Time-resolved diffraction experiments on piezoelectric actuators

Dissertation

zur Erlangung des Grades

des Doktors der Naturwissenschaften

der Naturwissenschaftlich-Technischen Fakultät III

Chemie, Pharmazie, Bio- und Werkstoffwissenschaften

der Universität des Saarlandes

Vorgelegt von

Dipl.-Ing. Florian Rödl

Saarbrücken, 2010

Tag des Kolloquiums: 04.06.2010

Dekan: Prof. Dr.-Ing. S. Diebels

Berichterstatter: 1. Prof. Dr. Eduard Arzt

2. Prof. Dr. Helmut Dosch

Vorsitz: Prof. Dr.-Ing. Frank Mücklich

Akad. Mitarbeiter: Dr. Dmitry Shakhvorstov

Abstract

One of the most important features of many common functional ceramics is piezoelectricity, a phenomenon which is not fully under-stood so far. Especially the time-dependent response and its role in the deterioration of properties due to fatigue has not been much investigated.

The present work focuses especially on time-resolved X-ray-diffraction, but also uses static methods to improve the understanding of dynamic processes that occur during switching in piezoelectric actuators and how they change with increasing fatigue. Micro-tensile tests were performed on the electrode material; the flow stress strongly depends on the temperature.

A new synchrotron-based method was developed to study actuators in-situ during switching on timescales of microseconds. The results show different relaxation processes depending on the sample position. In a pre-stressed actuator, only one 90° domain relaxation can be found in the active area. In an actuator without pre-stress, we can find two different 90° domain relaxation processes. In the inactive area of the actuator, only slow processes can be seen as no domain processes occur. Close to the electrode edge, high mechanical stresses yield defect relaxations which could be a reason for stronger fatigue in this area.

In this work it was shown that synchrotron experiments can be used to study the domain processes in piezoelectric materials. Future experiments could use this method to study the influence of fatigue on domain processes.

Zusammenfassung

In der vorliegenden Arbeit wurden in situ Untersuchungen an piezoelektrischen Aktoren durchgeführt. Dabei wurden keine Modellsysteme, sondern annähernd originale Bauteile aus Common-Rail Einspritzanlagen verwendet.

Neben mikrostrukturellen Untersuchungen wurden Mikrozugversuche an AgPd-Elektroden und zeitaufgelöste Röntgenexperimente durchgeführt. Die Mikrozugversuche zeigten, dass die Fließspannung des Elektrodenmaterials stark von der Temperatur abhängt.

Eine Methode für zeitaufgelöste Röntgendiffraktionsexperimente an Aktoren wurde entwickelt. Untersuchungen des Gesamtaktors zeigen kein starkes Relaxationsverhalten, im Gegensatz zu einzelnen Körnern. Während bei dem unter Vorspannung stehenden geteilten Aktor nur ein 90° Domänenprozess zu messen war, zeigte der freistehende Babyaktor zwei 90° Schritte. Ursache hierfür ist die Ausrichtung von Domänen durch die mechanische Vorspannung. Im inaktiven Bereich des Aktors wurde nur eine schwache Relaxation gemessen, da keine Domänenprozesse stattfinden. An der Elektrodenspitze kommt es durch hohe mechanische Spannungen zu ausgeprägten Defektrelaxationen, die das Ermüdungsverhalten beeinflussen könnten.

Es wurde gezeigt dass mit Hilfe von Röntgenstrahlen das Domänenrelaxationsverhalten piezoelektrischer Aktoren gemessen werden kann und von der Position auf der Probe abhängt. In zukünftigen Untersuchungen kann mit der hier entwickelten Methode der Einfluss des Ermüdungszustandes auf die Domänenprozesse untersucht werden kann.

Danksagung

Index

1   Introduction

One of the most interesting properties of modern functional ceramics is piezoelectricity, which is used in a wide variety of applications. While some of them are already well established, such as piezo ignition for lighters or the use in speakers and microphones, one of the latest and most fascinating uses of piezoceramics is the application as actuators in modern fuel engine injection systems.

Although actuators made of piezoceramics are mass-produced and do not suffer from serious drawbacks, there is an increasing interest in fundamental processes that occur in these materials. Research focuses on general material properties like phase compositions as well as mechanisms that take place during switching of piezoelectric materials, like domain processes or other possible relaxations. This is not only of fundamental interest; also the long-term fatigue behavior of piezoelectric materials might be influenced.

In addition to that, piezoelectric multilayer actuators that are used in injection systems do not only consist of the ceramic, but also of metallic interlayers that serve as electrode material. This combination may lead to different effects like intermixing, stress concentration and diffusion in the direct contact area of those two materials.

The objective of this work is to study the dynamic processes that occur in piezoelectric multilayer actuators during switching and how they may change during the lifetime of an actuator. The response of the whole actuator will be studied as well as single grains at different sample positions. Also, the influence of the electrode interlayer will be taken into account. Final goal is to improve the fundamental understanding of switching and fatigue and to give some better input for simulations.

2   Literature review

2.1 Functional ceramics

The term "ceramic" describes a wide spectrum of different materials ranging from old technologies that were already known many centuries ago to modern high-temperature and electronic applications under extreme conditions. Among several possibilities to classify ceramics, the most common is to distinguish between structural and functional ceramics. Structural ceramics are mainly used because of their promising high-temperature properties or their mechanical strength. Typical examples are Al_2O_3 or Si_3N_4.

In contrast to that, functional ceramics are used because of other special features like magnetic, electric, dielectric or optical properties. For special functions, these materials are superior to metals or polymers and are used in many modern applications. A wide variety of papers and books describe and summarize the state of the art of functional ceramic technology. Only as examples, the books of Wachtmann[1] and Moulson and Herbert[2] should be mentioned here.

2.2 Piezoceramics

2.2.1 History

One of the potential special features of functional ceramics is piezoelectricity. The word *piezo* is derived from the greek word *"piezein"* for *"to press"*. The first material on which piezoelectric properties were discovered is Rochelle salt, which was investigated by the Curie brothers in 1880[3]. They discovered that mechanical pressure on a crystal generates electrical charges in the material. In a systematic study it turned out that some other materials like quartz, tourmaline or topaz also

showed this property. The generation of charges due to mechanical stress is called direct piezoelectric effect. The opposite effect, where the application of an electrical field leads to mechanical deformation of the crystal, is called the converse piezoelectric effect and was also discovered by the Curie brothers one year later. The first application of piezoelectricity was established by Paul Langevin in 1917 with the sonar used to detect submarines in World War I.

With the discovery of a large group of oxide ceramics with perovskite structure in the late years of World War II, the technology of ferro- and piezoelectric ceramics advanced and became more and more interesting for electronic applications[4]. Nowadays, piezoelectric materials are both used as sensors (direct piezoelectric effect) and actuators (converse piezoelectric effect) and in other applications where fast and well controllable switching is of advantage. An overview of common applications is given in figure 2.1.

Generators (millivolts to kilovolts)	Motors (microns to millimeters)	Resonant devices (kilo- to megahertz)
hydrophones microphones phonograph cartridged gas igniters accelometers power supplies photoflash actuators sensors piezoelectric pens impact fuses composites	actuators (micro/macro) loud speakers camera shutters buzzers ink jet printers fish finders micropositioners valve controllers pumps video head positioners nebulizers piezoelectric fans relays	ultrasonic cleaners ultrasonic welders filters transformers delay lines

Motor/Generator (combination device)
sonar ranging transducers non-destructive testing medical ultrasound fish finders filters piezo transformers

Figure 2.1: Overview of the typical modern applications of piezoelectric ceramics[4].

4

2.2.2 Fundamentals of Piezoelectricity

For the fundamental understanding of the piezoelectric behavior of materials it is crucial to consider some general rules of crystal symmetry. There are altogether 32 different types of symmetry point groups. According to F.E.Neumann's principle[5], the symmetry characteristics of any physical property of a material must reflect the symmetry elements of the point group of the crystal.

It is easy to understand that it is essential for a crystal to be non-centrosymmetric to show piezoelectric behavior. A deformation of a unit cell that shows only symmetric features would not lead to any shift of charges and thus cannot lead to polarization. If one tries to categorize all crystal classes (figure 2.2) there are 21 groups among the 32 that are non-centrosymmetric. 20 of them show piezoelectric behavior. Among them, 10 are pyroelectric, i.e. they show spontaneous polarization when heated. If this polarization is reversible, a material is ferroelectric. A good overview about piezoelectricity and the general conditions for piezoelectric behavior is given in the fundamental book of Jaffe et al.[6].

Figure 2.2: Overview of all point groups and their electric properties.

The most important group of piezoelectric and also ferroelectric materials has been shown to appear in the so-called perovskite structure[7]. The typical composition is ABO_3 and the prototype for this structure is Barium Titanate ($BaTiO_3$). Figure 2.3 shows the unit cell of a perovskite PZT (details will be discussed later) that can be understood as a cubic structure where the cations are located in the

edge (Pb^{2+}/Zr^{2+}) and centre (Ti^{4+}) position and the oxygen ions are placed on the face-centered positions. To enable piezoelectric behavior, the structure is distorted, for example tetragonally. In this case, the centre ion does not occupy the position exactly in the centre of the unit cell but is located slightly above or below the centre position. This leads to an external polarization. The centre ion can thus altogether occupy 6 positions in the unit cell (3 directions with two positions each).
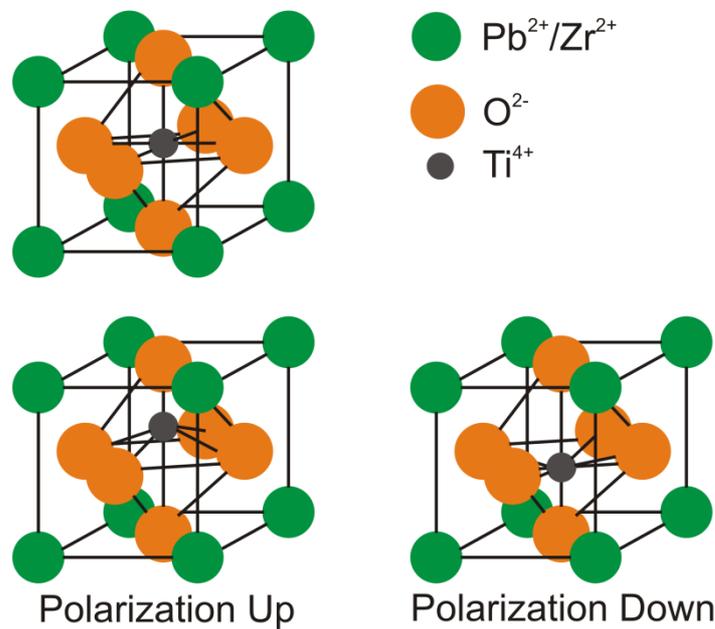
Figure 2.3: Polarization switching in a perovskite PZT unit cell.

Most materials used in applications are polycrystalline and consist of many grains of different orientations. If we simplify and consider a single crystal or single grain of a perovskite material, it is obvious that only a certain number of orientations are feasible. This leads to the formation of so-called ferroelectric domains[8], a region in the grain where the polarization points in the same direction. The size of such a ferroelectric domain is determined by an energy minimization between the leakage field of the domains and the energy that is necessary to form a domain wall between two neighboring domains. Typical sizes are around 50-100 nm, this

would mean that a typical grain of few μm diameter consists of hundreds or thousands of domains. In a non-textured grain of a perovskite material directly after fabrication, we do not have any preferred direction of polarization. If we now apply an external field, we have to consider two quantities: The first is the change of the internal polarization with the electrical field. The second is the macroscopic length change of the crystal.

We can first treat the change of polarization in the material, a feature of ferroelectric materials. Starting from a point (1) (figure 2.4) with no electrical field and no net polarization, the external electric field is increased. This will first lead to an increasing polarization. Ferroelectric domains with a certain direction of polarization are already present in the material. With increasing field strength, the domains that point in the direction of polarization will grow at the expense of domains that point in other directions. At a certain point, all domains will be polarized in the direction of the external field or, because of the limited number of possible directions, at least in a direction close to the external field. A saturation state called saturation polarization P_S will be reached (2).
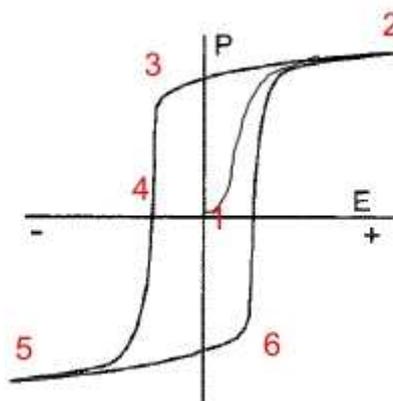
Figure 2.4: Typical polarization hysteresis loop

Taking away the electrical field will not immediately lead to a non-polarized state because there is now an energetic barrier that has to be overcome to switch the

polarization to the opposite state. At zero field, there is still a remaining polarization called the remnant polarization P_R (3). Only at a certain electric field strength (the coercive field E_C (4)) will the polarization return to zero and then switch to the opposite direction, where it reaches again the saturation polarization (5). Switching off the electric field will finally lead to the remnant polarization (6) again and applying a positive field will switch the polarization back to point (2), the positive saturation polarization.

So far we have only discussed the behavior of ferroelectric species. Considering a piezoelectric material and the length change in such a material, another type of hysteresis can be introduced: The so-called butterfly loops where the length change is plotted against the electric field strength (figure 2.5). Starting from a point without external polarization (1), an increasing number of domains will point in the same direction. This gives rise to an elongation of the crystal until the saturation polarization is reached (2).

If domains in a tetragonal material change their orientation, they can either flip into the opposite direction or in a direction perpendicular to the initial direction (90° switching). Typically, the polarization of a piezoelectric material will not change by one 180° switching process, but by two 90° switchings. Switching in this case does not mean that domains fully change their orientation. Usually, regions close to domain walls change their orientation and this leads to a growth of a domain at the expense of neighboring domains. Taking away the field will first lead to shrinkage (3), but when applying a reverse field the sample will shrink even more, because many domains are now oriented in a direction perpendicular to the axis of average polarization. At a certain point (4), these domains will change their orientation and start to point in the opposite direction and thus the crystal will elongate again (5). Applying a positive field will lead to the same processes in the opposite direction.
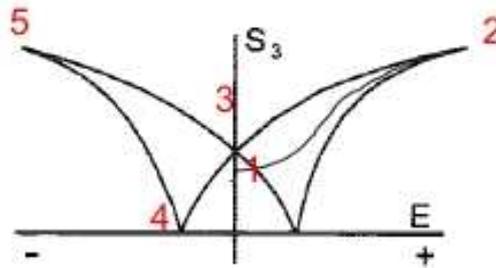
Figure 2.5: Typical strain hysteresis loop

The shape of the hysteresis loops is important when describing the properties of ferroelectric and piezoelectric materials. Degradation processes in the material are also visible by considering the hysteresis and many papers deal with proper analytical descriptions to explain the hysteretic behavior of a piezoelectric material [9-12].

A simple mathematical description of piezoelectricity is given by two basic equations established by Jaffe et al.[6]:

$$D = d \cdot E + \varepsilon_T \cdot E \tag{2.1}$$

$$S = s_E \cdot T + d \cdot E \tag{2.2}$$

D is the dielectric displacement (which can be considered equal to polarization), T is the stress, S the strain, E the electrical field, s the material compliance (the inverse modulus of elasticity) and ε the dielectric constant. d is the piezoelectric constant, which is numerically identical for both effects. The superscripts indicate a quantity held constant, which means in the case of ε_T that the piezoelectric element is mechanically unconstrained and in the case of S_E that the electrodes are short-circuited[4]. With these two equations (in matrix form), the properties along different orientations of the material can be described.

The piezoelectric coefficients d_{ij} relate to the direction of polarization and the direction of stress. Typical equations for these coefficients are:

$$D_i = d_{ij} \cdot T_j \qquad\qquad\qquad (2.3)$$

$$S_i = d_{ij} \cdot E_j \qquad\qquad\qquad (2.4)$$

Equation 2.3 describes the direct piezoelectric effect and equation 2.4 the converse piezoelectric effect.

There are many piezoelectric materials used in different fields of applications nowadays. Some polymers and salts are important, but most applications focus on piezoelectric ceramics with perovskite structure, among which the materials based on lead zirconate titanate (PZT) are most important.

2.3 Lead Zirconate Titanate (PZT)

In 1955, a patent[13] was registered in which Bernard Jaffe (who later wrote a fundamental book on piezoelectric ceramics) reported that materials composed of lead zirconate and lead titanate show very high piezoelectric coefficients in the composition regime around 55% lead zirconate. The general composition of this group of ceramics is $PbZr_xTi_{1-x}O_3$ and the group is referred to as lead zirconate titanate (PZT). Since that time, many investigations on this system have been performed and the properties have been widely analyzed.

2.3.1 Phases and Properties

The first PZT phase diagram was also established by Jaffe et al. in 1971[6]. Figure 2.6 shows the phase diagram that mainly is still valid today, although some new questions arose in recent years.
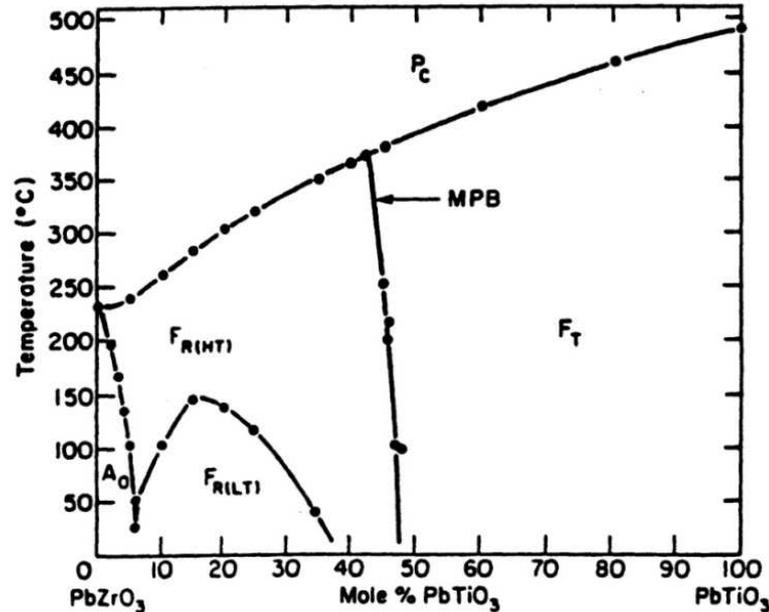
**Figure 2.6: Phase diagram of PZT as established by Jaffe et al[6]. The low tempera-
ture-phases are ferroelectric and appear in rhombohedral (F_R) or tetragonal (F_T) [14]
crystal structure. The phases are separated by the morphotropic phase boundary
(MPB). The high-temperature cubic phase is paraelectric (P_C).**

There are three main phases in the system. At higher temperatures, a paraelectric
cubic phase (P_C) exists. This phase transforms at the Curie temperature (T_C) into
two ferroelectric phases one of which, depending on the composition, is rhombo-
hedral (F_R), while the other is tetragonal (F_T). On the rhombohedral side of the
phase diagram exists a low-temperature phase. All three phases appear in a dis-
torted perovskite-type structure in which the titanium or the zirconium ion is the
centre ion in the unit cell.

Most technical interest focuses on the compositions close to the phase boundary
between the rhombohedral and the tetragonal phase. In this region the piezoelec-
tricity is particularly strong[6]. The boundary between both phases is called the
morphotropic phase boundary (MPB). Up to today, the reason of the extremely
high piezoelectric response of materials in this regime is not fully understood.

Park and Shrout[15] proposed that local stresses may induce phase transformations which altogether lead to higher strains than the pure piezoelectric response of the material. Bell[16] later presented a model to support this hypothesis. Rossetti[17] theoretically predicted a larger area of phase coexistence near the MPB, but up to now there is no experimental evidence for that.

A different hypothesis arises from investigations which Noheda et al.[18-22] performed in 1999 and later using synchrotron radiation. A detailed phase analysis of a polycrystalline sample that was prepared very carefully to avoid internal stresses revealed the existence of a monoclinic phase at lower temperatures (figure 2.7).
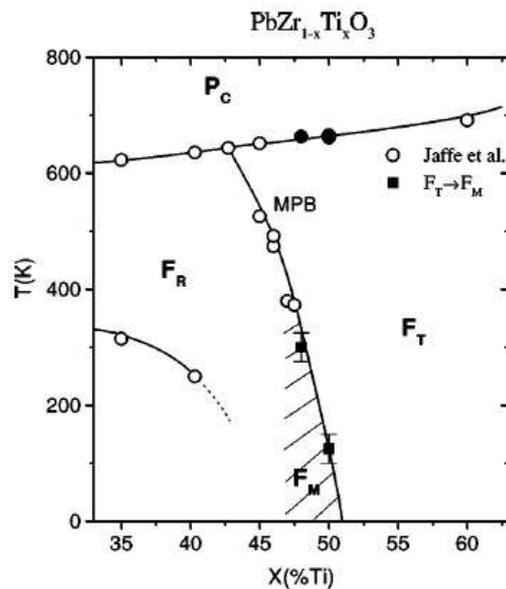
Figure 2.7: Phase diagram showing the existence of a monoclinic phase near the MPB as suggested by Noheda et al.[22].

The authors pointed out that the reason why this new phase was not discovered before was that the lattice parameters were very close to the rhombohedral and tetragonal phases and thus the resolution had not been high enough. It is also very difficult to produce clean and stress-free samples. Some first-principle calculations done by Bellaiche et al.[23] revealed that it is also possible to explain the high

piezoelectric coefficients by the high d_{15} coefficient in the monoclinic crystal. In many further studies the group strongly supported the thesis of a monoclinic phase, but up to now it is still controversial whether it exists at room temperature and may be the reason for the strong piezoelectric response. Other possible explanations for the experimental data might be highly stressed rhombohedral or tetragonal fractions which only "appear" to be a monoclinic phase.

Generally, PZT ceramics can be considered as hard ferroelectrics, which means that the hysteresis loop is nearly square-shaped and the remnant polarization is high. If we consider some possible applications, it may be necessary that the ceramic is used in a pre-stressed state which may affect the piezo- and ferroelectric properties[24]. Figure 2.8 shows the evolution of both the polarization and the strain hysteresis of a piezoelectric ceramic as a function of static stress applied parallel to the field direction[25]. The reason for this behavior is the obstruction of the domain movement. Thus, higher field strengths are necessary to move domains and a lower total polarization and strain will be reached. If stresses are applied in the described way, the switching processes change from mainly 180° domain switching in the unloaded state to 90° domain switching in a loaded state. If only unipolar loads are applied (see chapter 2.3.3), there is a maximum strain level at a certain pre-stress[26-30]. The reason for this is the alignment of domains due to the pre-stress. Domains are forced to switch into a configuration perpendicular to the applied stress, so the total actuator can reach higher strains when a stress is applied.
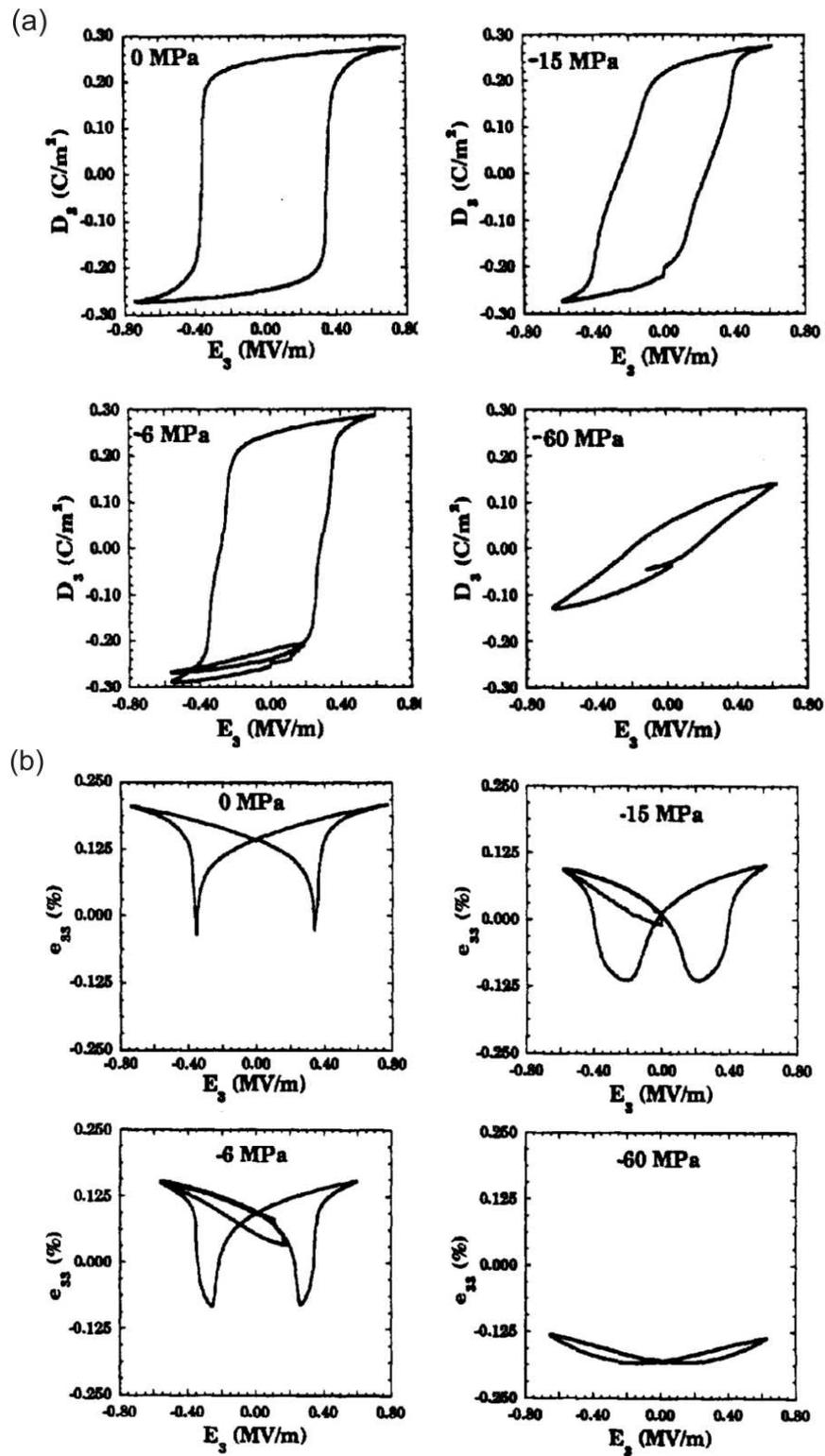
Figure 2.8: Evolution of the polarization hysteresis (a) and the strain hysteresis (b) with increasing external stress parallel to field direction[25].

2.3.2 PZT with dopants

In application, PZT ceramics always contain dopants to improve certain designated properties. Jaffe et al.[6] list a wide variety of dopants and their influence on the PZT properties. Two groups are important, the so-called isovalent and off-valent dopants. Isovalent means that the valence state of the new ion is similar to the ion it replaces. Pb^{2+} can for example be substituted for Sr^{2+} or Ca^{2+}. This yields a lower Curie temperature, but a higher dielectric constant and a higher coupling coefficient at room temperature. Adding Ba^{2+} increases the region of phase stability for the cubic phase. Of greater importance are off-valent dopants such as Nb^{5+} (replacing Zr^{4+}) or La^{3+} (replacing Pb^{2+}). Adding a donor like Nb^{5+} leads to A-site vacancies enhancing domain reorientation. Typical properties of donor-doped ceramics are square-like hysteresis loops, low coercive fields, high remnant polarization, high dielectric constants, high coupling factors and reduced aging. Most of these properties are desirable for piezoelectric ceramics. Poling with acceptors such as Fe^{3+} replacing Zr^{4+} limits domain reorientation and gives rise to poorer piezoelectric properties, but higher mechanical stability. The most important dopant for the PZT system is La^{3+}, PZT doped with Lanthanum is referred to as PLZT and of high relevance for applications.

2.3.3 Piezoelectric Actuators

PZT-based piezoelectric ceramics are widely used in many applications. The focus of this work is in the field of piezoelectric actuators and thus the concept of this component and possible designs[31] will be explained further in this chapter. The simplest possible design of such an actuator is a disc of a piezoelectric crystal with an electrode mounted on each side, as shown in figure 2.9 (a). There are several disadvantages of such an actuator. The voltage that needs to be applied is proportional to the thickness of the crystal. Typical length changes are around 0.2% and typical field strengths are around 2 kV/mm. To reach a displacement of 50 μm one would thus need a crystal with a thickness of 25 mm and a voltage of 40 kV.

It is obvious that a single disc-design is not suitable to reach strains that are required for many applications. Two possible designs to get to higher strains by connecting several layers are shown in figure 2.9 (b) and (c). A multilayer actuator as shown in figure 2.9 (b) is basically built out of many piezoelectric layers (marked with A) with electrodes separating them. These electrodes (B) are alternately connected to both electrodes so that each layer will operate independently. This design is called interdigitated and is not very sensitive to failure: if a single layer fails for any reason, the other layers will still continue operating (as long as no direct electronic path between the electrodes is present). One of the disadvantages of this so called double-comb structure are field inhomogenities that occur at the electrode edges (C). This gives rise to internal stresses. The main area of mechanical failure is thus close to the internal edges of the electrodes[32-34]. Another possible design is the double helix structure (figure 2.9 (c)). Here, the problem of stress concentration does not occur, but a failure due to short-circuit is more likely because the electrodes are continuous and fabrication is much more sophisticated. If one single disc of piezoelectric material is mounted to a non-piezoelectric material, this configuration can be used as bending actuator (figure 2.9 (d)).

This work will concentrate on actuators with interdigitated design. Figure 2.10 shows the steps of fabrication[32] of such an actuator. Starting with a green sheet of PZT, the electrodes (usually made out of silver or silver palladium alloys) are printed on it via a screen process. Several hundreds of these layers are then laminated together. At the top and bottom, an actuator is usually fixed and thus some inactive layers are used. The laminated actuators are cut to single devices and sintered at temperatures around 1000 °C. They shrink by about 20 % in volume during sintering. On the sintered actuator, the external electrodes are mounted and finally the actuator is pre-polarized in an electrical field. This can happen at room temperature or at elevated temperatures.
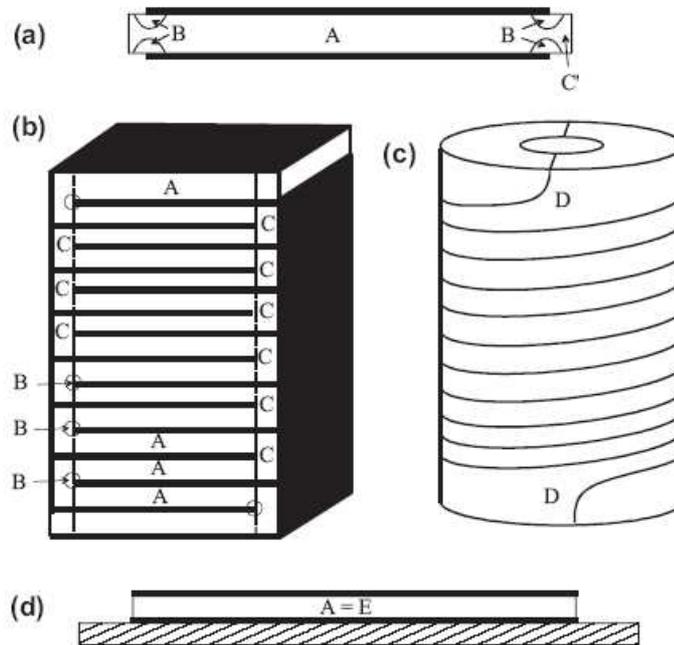
Figure 2.9: Possible actuator geometries[31]. (a) single disc geometry, (b) double-comb structure, (c) helix structure, (d) bending actuator.
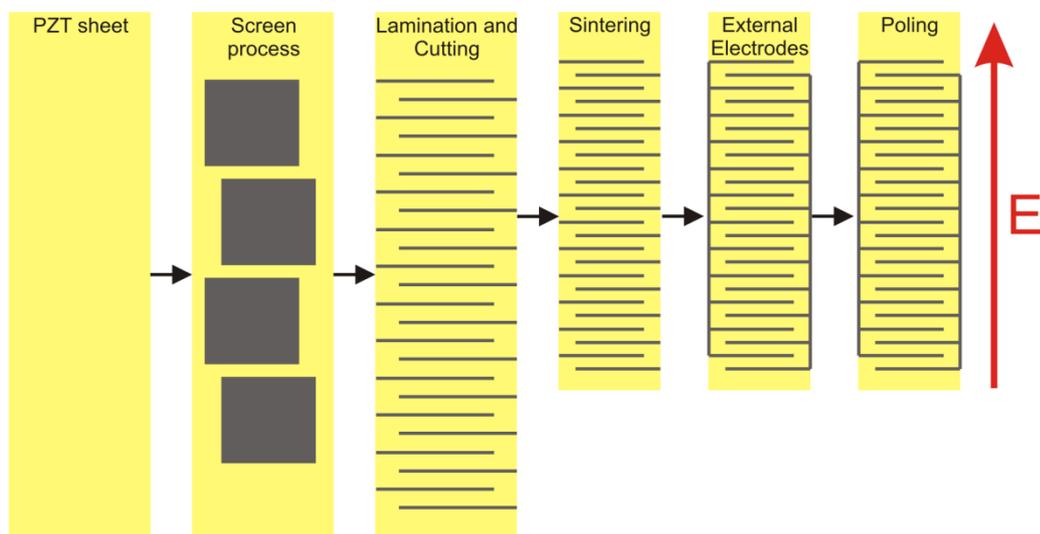
Figure 2.10: Schematic overview over the fabrication steps of a piezoelectric actuator. The electrodes are printed on the PZT sheet and the single actuators are cut and sintered. After the external electrodes are mounted, the actuator is poled.

17

Multilayer actuators are used for example in engine injection systems, precision mechanics and optical stages. To ensure long-term stability, many studies have been performed to investigate the reasons for fatigue of these materials. The focus of this work will be on the application as switch in modern diesel injectors[35], where the use of piezoactuators enables faster and more exact control of the injection process. This yields a fuel reduction of approximately 10 %. Usually, these actuators are made of doped PZT ceramic layers connected to AgPd electrodes[36,37].

Different types of loading scenarios exist which define the possible processes involved in switching and fatigue. Figure 2.11 gives an overview about all possible types of cyclic loading that can occur in piezoelectrics. The simplest driving mode of an actuator is unipolar loading, where only an alternating unidirectional current is applied (a). A small amount of domain wall movement occurs. By combining different measurements, it is possible to distinguish between the so called intrinsic strain coming from the piezoelectric effect and the extrinsic strain by domain wall movement[38,39]. The total extent of extrinsic and intrinsic strain depend on the shape of the hysteresis; for softer piezoelectrics, more domain wall movement is involved. Concerning uniploar loading, only a few studies on fatigue have been performed, but fatigue problems still occur[40]. A typical component with unipolar loading is an actuator in engine injection systems. If this is done under a compressive pre-load the amplitude of the strain changes (c), with a maximum strain at a certain intermediate stress. Mixed loading (b) occurs in ultrasonic motors where a slightly higher amount of domain movement is involved. The difference to unipolar loading is the hysteresis loop of the material that covers a larger area. If larger strains are required, partially negative voltages are applied. This is called sesquipolar loading (d). The more domain processes are involved in the total switching, the higher is the risk of fatigue problems. In ferroelectric memory devices (FERAM), it is necessary to switch between a fully positive and a fully negative polarization state (bipolar loading, (e)). A large amount of domain wall movement

occurs. Consequently fatigue problems are higher than in all other types of loading and most studies on fatigue of piezoelectrics focus on bipolar loading mode[31,41-43].
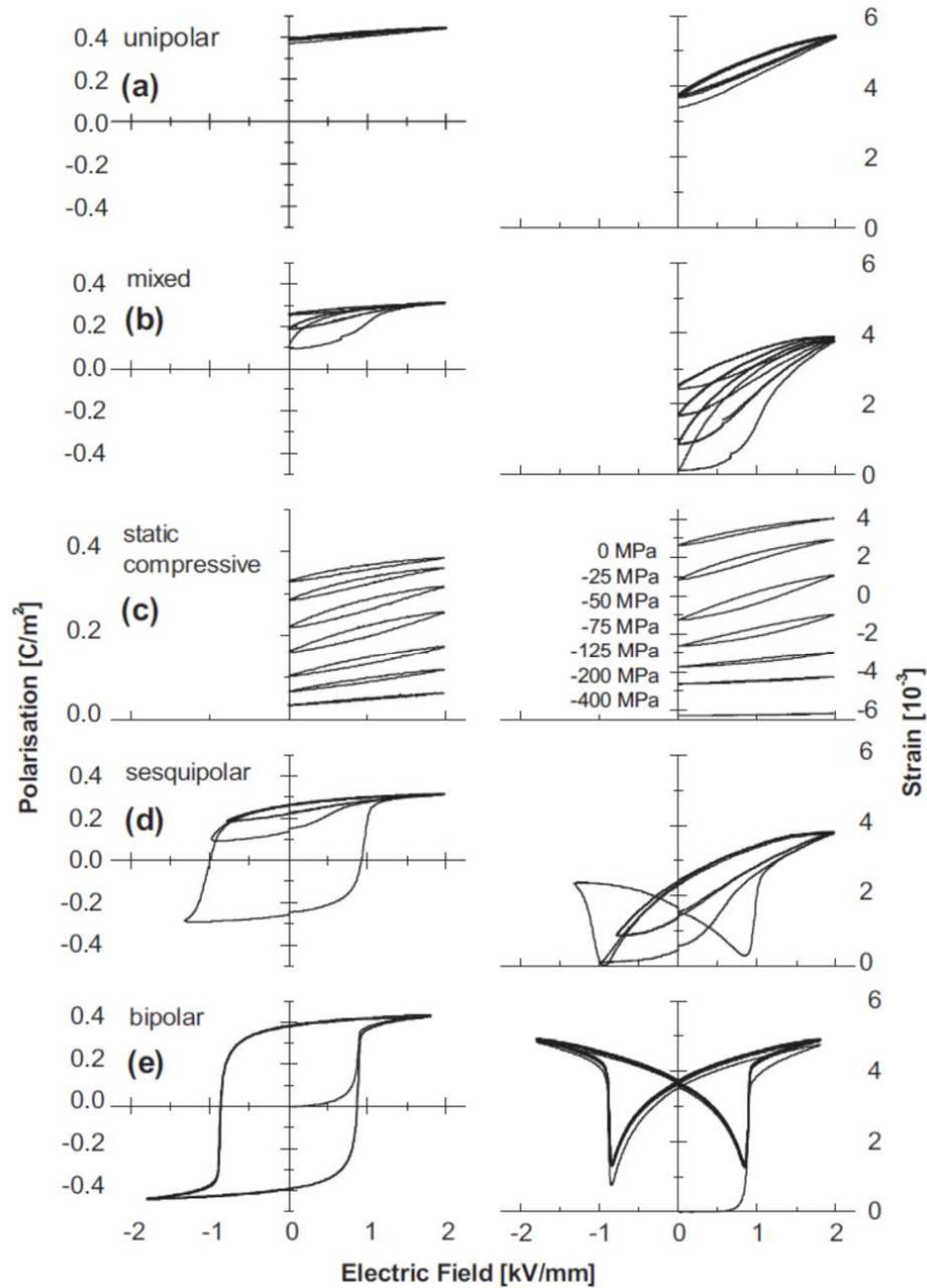
Figure 2.11: Overview on hysteresis loops of a PZT ceramic during different types of loading scenarios[31].

2.3.4 Fatigue in PZT

There are in general two types of ageing or fatigue in piezoelectric devices. The first one is the "classical" type of fatigue: crack nucleation finally leading to crack growth and failure. In multilayer actuators, cracks will mainly appear at the areas of inhomogeneous mechanical stresses which are the internal electrode edges (Figure 2.9 (b), B). Once small pre-cracks are present, cyclic loading finally leads to crack growth and failure. Only few studies deal with pure mechanical fatigue[44], normally also electrical fields are involved[45-48].

If we consider both mechanical and electrical load, we first have to introduce a second type of fatigue behavior. Not only mechanical properties are influenced by the loading history of a piezoelectric ceramic, but also the electrical properties are modified. This is termed electrical fatigue and most research in the area of fatigue of piezoelectrics performed in recent years focussed on this phenomenon. If we take a closer look at the long-term behavior of piezoelectric ceramics, several changes in the hysteresis loops are visible (figure 2.12)[31]. The polarization loops show decreasing amplitudes of polarization while the strain loops do not only show this decrease but also a growing asymmetry. Both effects have been widely investigated in the last years in different studies of electrical fatigue[41,42,49-52] and possible explanations for this were suggested.

If we compare the degradation of the hysteresis loops with pre-loading scenarios (figure 2.8) we can see similar effects. A decreasing polarization always indicates a reduction of switchable polarization. There are multiple mechanisms that have been suggested to explain fatigue in piezoelectric components happening on different length scales. An explanation for this behavior is always linked to understanding how switching changes over the lifetime of a piezoelectric material[52]. The main theory today involves electrical stress that results in a creation or redistribution of imperfections where these imperfections influence the switchable polarization. Possible imperfections are delaminations of the electrode[53], the for-

mation of a passive (non-switching) layer close to the electrode[54] or changes of the domain configurations due to the pinning of domain walls and seeds[31]. The latter process is considered to be the most likely and defect clusters of O^{2-} vacancies, holes and electrons from the electrode material or dopants[46,52,55] are regarded as possible agents to form these clusters. Fatigue appears much earlier if the voltage is higher than the coercive field[43].
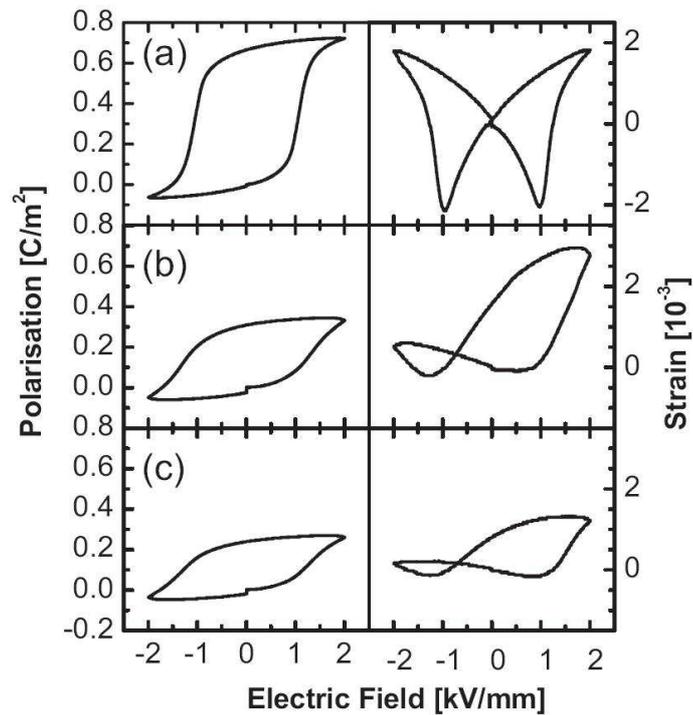
Figure 2.12: Typical evolution of hysteresis loops of a PZT alloy with increasing cycle number[31].

The reason for the asymmetry of the strain loop has also been widely studied. Today it is believed that free charge carriers generate a bias field that modifies the external field[51] together with an offset polarization where domains are "locked" in a polarization state. Domain walls do not move anymore due to defects. These two effects are considered to occur more or less randomly and irreproducibly[56].

Several studies focus on fatigue and how it may be influenced by changing different boundary conditions. To summarize this, fatigue behavior depends on many parameters such as the oxygen concentration[57], switching voltage and temperature[52], the composition of PZT[58] and dopants[49], potential buffer layers[59], the electrode material[60] or the grain size of the material[61].

Almost all of these studies have been performed using bipolar loading scenarios. There are only very few studies on unipolar fatigue even though this is of high importance for the application as actuators. The work of Verdier et al.[40] showed that even though switching plays only a minor role in the response of a piezoelectric actuator in unipolar loading, still a degradation and an offset polarization is measurable. They do not find any indications that the same mechanisms are responsible that can be found under bipolar loading. By contrast, the mechanisms for the offset in strain hysteresis seem to be the same.

The dominant mechanisms that give rise to fatigue in piezoelectric ceramics are partly understood, but still questions remain open. Many mechanisms that are suggested by different models are not proven yet. Conditions close to application and under unipolar loading have not been studied much. Up to now, no experiments deal with the influence of dynamic effects like relaxation processes in the material or the in-situ measurement of domain processes. In this work, we will try to measure the direct dynamic response of a piezoelectric material.

2.3.5 Diffraction Studies of PZT

A big advantage when studying piezoelectric materials by X-ray or neutron diffraction methods is the tetragonal or rhombohedral structure of the material. This non-cubic distortion leads to a splitting of some of the reflections and thus domain processes and orientation changes can be studied by diffraction methods. When working with X-rays, synchrotron radiation offers high brilliance and opens the field even to position-resolved or time-resolved measurements. A total overview

about all possible applications of X-ray diffraction methods to piezoelectric materials can be found in the substantial review by Jones[62].

If we consider the tetragonal phase and take c as the axis of tetragonal distortion, we expect a splitting of the {001} type reflection into a (001) peak at lower angles that represents lattice planes oriented perpendicular to the direction of polarization and a (100) peak that represents the lattice planes oriented parallel to the poling axis which should have double intensity if the material is non-textured. The {111} plane represents the unit cell diagonal and the peak position and the integral intensity should not be influenced by poling (figure 2.13). In contrast, the rhombohedral phase should not show big differences at the {100} peak, but the {111} intensities change. Figure 2.14 shows an example taken from a paper by Guo et al.[19] in which the change of the different peaks with the poling state of the ceramic was investigated. The splitting of the peaks as discussed above is well visible. The intensity ratio between (002) and (200) for the tetragonal case and (111) and (11-1) for the rhombohedral case changes when a field is applied. In addition, poling leads to a broadening of some of the peaks due to higher strains.
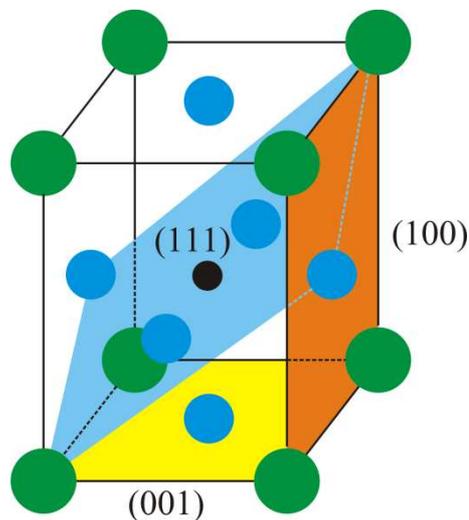
Figure 2.13: Sketch of different lattice planes in a tetragonal unit cell. While the (111) reflection does not split up, the {100}-type planes shows two reflections depending on the orientation.
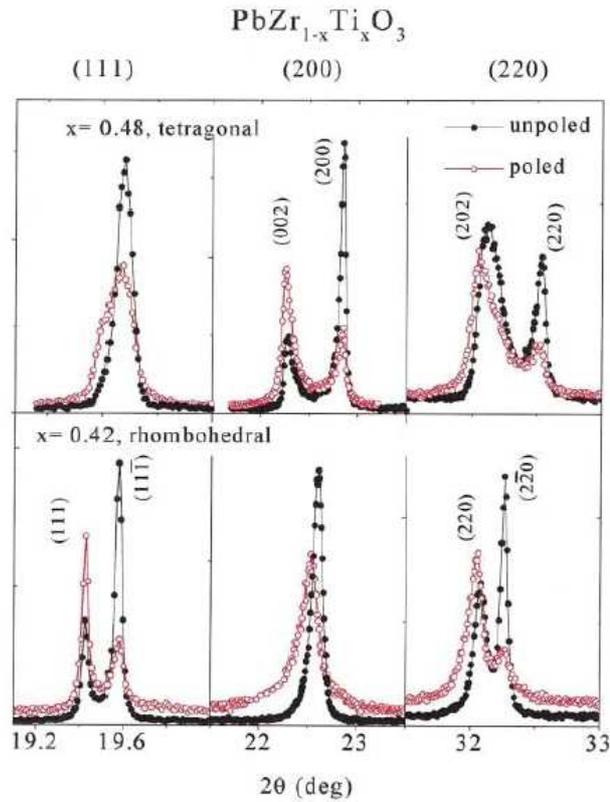
Figure 2.14: Change of different Bragg reflections with poling of two polycrystalline PZT ceramics of different phase composition[19].

The observation of peak changes can also be used to macroscopically identify the influence of domain processes on the fatigue of PZT ceramics[63]. A study by Do et al.[64] deals with the behavior of single domains in a thin film using X-ray microdiffraction with sub-micron resolution. The work revealed the pinning of some areas of the film. The inactive regions could be reactivated by applying a higher field (figure 2.15).
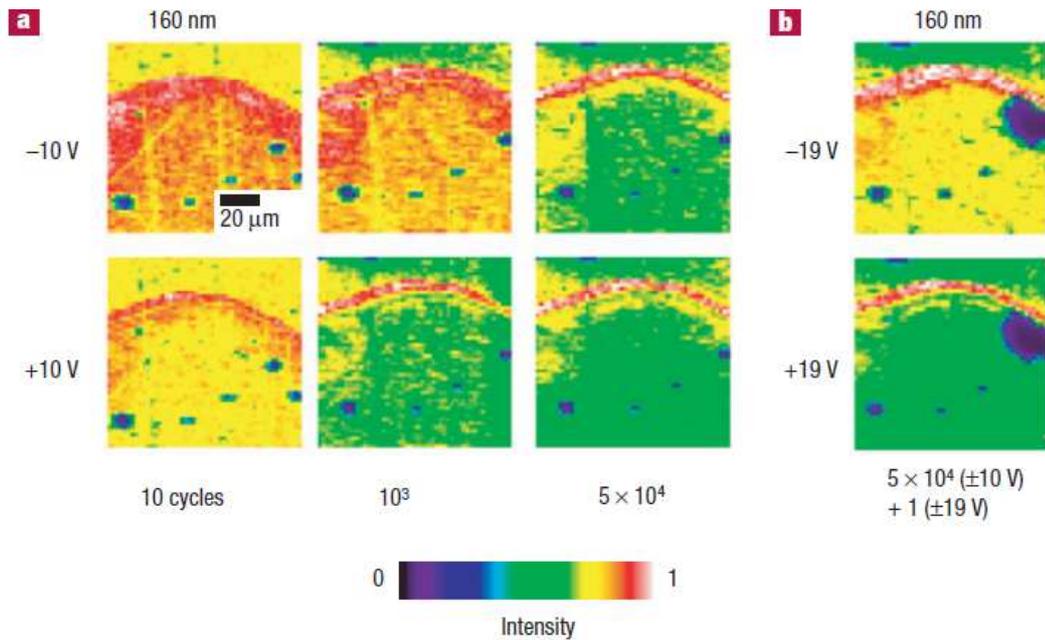
Figure 2.15: Study of the (002) reflection in a 160 nm PZT film with increasing cycle number. The colors represent a changing X-ray intensity. (a) After 10^3 cycles the maximum domain switching is visible. A higher cycle number leads to a decrease of switchable polarization. (b) The switching processes can be restored by applying a higher field[64].

Finally one can also use x-ray-diffraction to study the changes in lattice parameter to either measure the evolution of residual stresses[65,66], the strain hysteresis[38], the fraction of switched domains[67], piezoelectric coefficients[68] or to detect fracture mechanisms[69,70]. In this study, the main focus will be on the changes of lattice parameters and the tilting of lattice planes in time resolution after switching.

2.4 Time-resolved Investigations

The methods explained so far are used to study the static behavior of piezoelectric materials in different states. This can give an insight on many important properties, but nevertheless some other features are not taken into account. When a piezoelectric material switches, all processes involved are of dynamic nature and thus also time-resolved techniques are suitable to study them. There are several differ-

ent phenomenon that occur on different timescales. Some of them have been studied quite well on model systems, but a fundamental study of actuators in operation mode has not been done so far. Different transient phenomenon can be found in piezoelectric materials. We first expect the intrinsic piezoelectric relaxation to happen, which is a very fast process. Domain wall movement (which will be dealt with in more detail in chapter 2.5) and possible diffusion and stress relaxation processes happen on slower timescales. Finally, also very slow relaxations can be found until the final state is reached. All these processes are strongly influenced by the external field that is applied.

There are several methods to measure the dynamic response ranging from simple time-dependent length measurements over different mechanical spectroscopy methods to time-resolved diffraction that includes different techniques to measure the response on a wide range of timescales[71].

First, the macroscopic response of the length change of a piezoelectric material will be considered. According to Jung and Gweon[72], two different regimes can be distinguished (figure 2.16): a regime of dynamic response where the actuator shows an overshooting of the length and dynamic oscillations followed by a creep regime in which the actuator slowly drifts to its final elongation. This happens in timescales of ten to some hundred seconds and depends on the peak voltage. The higher the voltage, the faster the final elongation is reached.
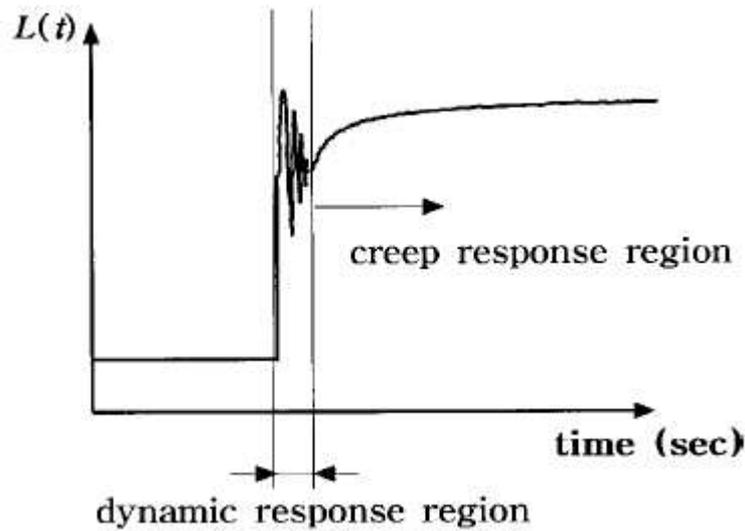
Figure 2.16: Time-dependent length change of a piezoelectric actuator. The actuator shows a dynamic response with periodic oscillations followed by a slow creep regime[72].

Mechanical spectroscopy is an indirect method to measure and identify relaxation processes that occur in the material. For example, the frequency-dependent piezoelectric properties can be studied[73]. The results show a decrease of the material polarization with increasing frequencies. The decrease starts at around 100 Hz, which would suggest that the dominating relaxation processes occur in the material on the timescales of several milliseconds and faster. A study by Li et al.[74] reveals that fatigue is lower when the material is excited with lower frequencies. The authors could explain this by relaxation processes which are completed before the next switching occurs. The processes they could identify are the creation and reorientation of electrical dipole defects.

Some other papers focus on measuring local effects by AFM-related methods. Fu et al[75] showed on a 200 nm PZT film that even after thousands of seconds, domain relaxations still occur and change the total domain area. Similar findings were published by Ganpule et al[76]. Other very fast studies[77,78] done with PFM focus on domain wall speeds. Another example for relatively long-term relaxations com-

pared to normal switching times can be found in the work of Lee and Lee[79]. They measured the remnant polarization as a function of time and found a relaxation in the millisecond regime, which is closer to the results found by mechanical spectroscopy.

Even though other methods might give interesting results, the best view on dynamic processes on atomic scales is given by time-resolved diffraction methods. Different techniques exist[71], which can either give very high temporal resolution by using gated detector setups, where only counts in a very small time interval of interest ($\Delta t > 50$ ps) are collected, or make use of the full incoming beam intensity by using multichannel scalers. With this technique, the resolution limit is in the range of microseconds.

The first time-resolved studies of piezoelectric materials date back to the 1980s, where McWhan et al[80] measured the intensity changes of different Bragg peaks of $BaTiO_3$ single crystals using a multichannel counter setup. The focus of their work was the speed of field-induced phase transitions which happen on millisecond timescales. One year earlier, Zorn[81] also used time-resolved methods with a multichannel counter to measure the piezoelectric coefficients of PZT. Later studies use much more sophisticated setups, especially the improvement of synchrotron radiation sources led to a great improvement of time-resolved techniques, as now much higher beam fluxes were available. Long and very short term studies can now be performed with high accuracy.

To measure the direct piezoelectric response of a material, very fast techniques are necessary. Grigoriev et al.[82] measured the time-dependent Bragg peak position of a PZT thin film after the application of an electric field. Figure 2.17 shows the corresponding graph. The piezoelectric lattice deformation takes place in several hundred picoseconds. The relaxation time at different sample positions was also measured and from this, a domain wall speed of 40 m/s could be extracted. The

result corresponds to PFM measurements done by other groups[77,78]. A similar study by Zolotoyabko et al.[83] revealed a strong frequency dependence of the switching speed.
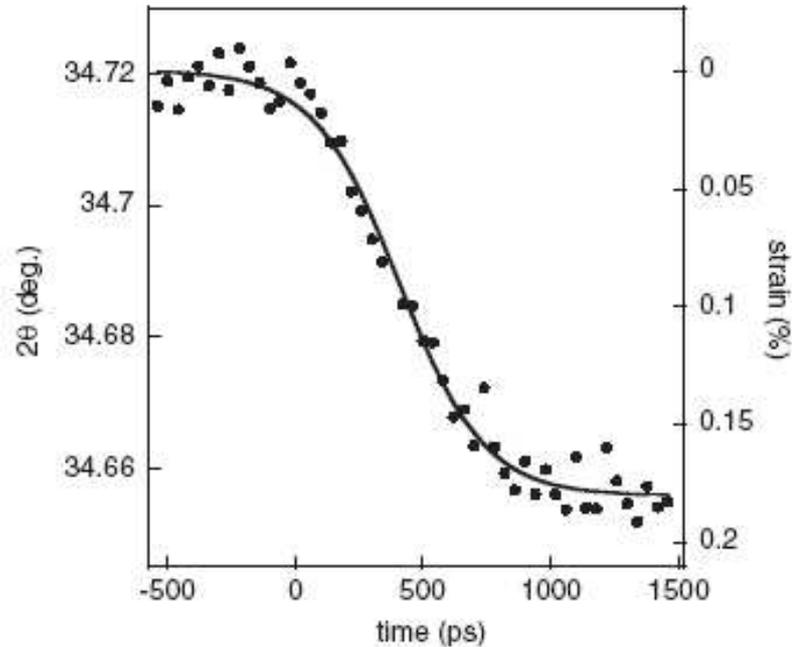
Figure 2.17: Time-dependent Bragg peak position of a PZT thin film after application of an electric field[82]. Lattice deformation has finished after 1 ns.

A completely different effect has been found by van Reeuwijk et al.[84] on a DKDP (Potassium Dideuterium Phosphate) single crystal. The group could measure additional periodic oscillations happening in microseconds when studying the rocking curve position (figure 2.18). These oscillations could be attributed to the propagation of elastic strain waves reflected from the crystal edges. Similar effects in multilayer actuators would be much harder to detect because of the many different interfaces that are present in the material.
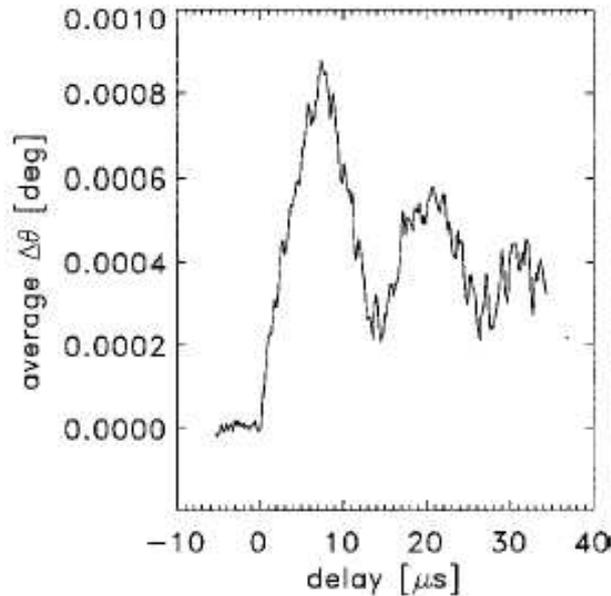
Figure 2.18: XRD rocking position of a piezoelectric DKDP single crystal as a function of time after switching[84]. The oscillations are due to strain waves propagating through the crystal.

Some recent studies by neutron diffraction on PZT ceramics dealt with the time-dependent response focusing on the domain configuration. The (002)/(200) doublet was studied and a significant change in intensity was found[85]. Also, the time-dependent lattice strain was measured. In both cases, the resolution was not high enough to resolve possible relaxation mechanisms[86] (figure 2.19).

To summarize all time-resolved measurements, one can distinguish between two types of effects. The first one is the simple intrinsic piezoelectric effect which happens very fast. On the other hand, domain wall movement can occur very slowly, even much slower than the technologically relevant times. As the theory of domain wall movement will play a role later in this work, the literature review will be more detailed here.
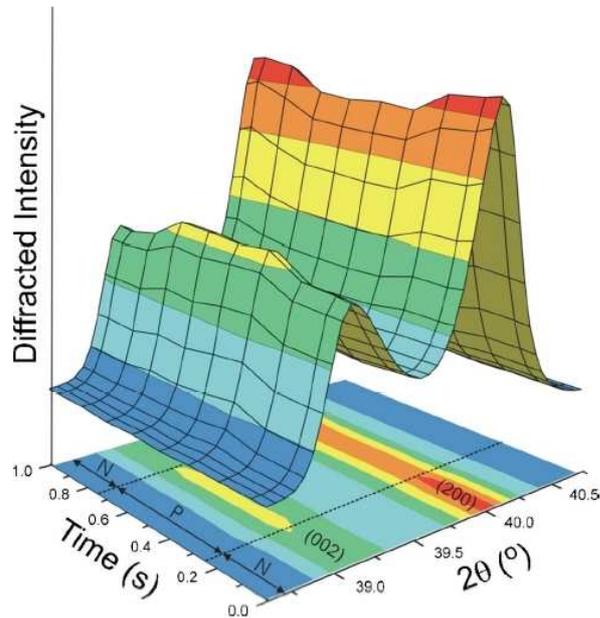
Figure 2.19: Time-dependent change of the (002)/(200) doublet in a piezoelectric material[86]. Domain switching can be proven very well, but no significant relaxations can be resolved with the setup.

2.5 Domain dynamics

2.5.1 Theory

When speaking about domain dynamics, often the expression of moving domain walls is used. In reality, domain walls do not really move, but regions close to the boundaries of different polarization direction change their orientation. This is not simple to describe, and many effort has been done to understand the processes that occur close to the domain wall and how this can be modeled theoretically.

The most accepted model nowadays is based on Avrami's theory of phase transition kinetics[87-90]. This theory was adapted to ferroelectric materials by Ishibashi and Takagi in 1971[91] and 1985[92]. According to Ishibashi[92], the reversed domain fraction at time t, Q(t) is given as:

$$Q(t) = 1 - \exp[-A(t)] \tag{2.5}$$

where A, called the fraction of the extended area, can be written as:

$$A(t) = \int_o^t R(\tau) S(t,\tau) d\tau \tag{2.6}$$

The rate of nucleation at a certain time τ is described as $R(\tau)$ per unit time per unit area. $S(t,\tau)$ is the area covered at time t by the reversed domains nucleated at τ. In this case, S can be written as:

$$S(t,\tau) = D[r_c + v(t-\tau)]^d \tag{2.7}$$

The domains grow with a constant velocity v, r_c is the radius of the reversed nuclei and d describes the dimensionality of the growth: $d=1$ for one-dimensional, 2 for two-dimensional and 3 for three-dimensional growth. Assumptions for the model[93] are (1) a random distribution of pre-existing, aligned domains with a uniform radius r_c, (2) a constant nucleation rate of aligned domains with radius r_c and (3) constant velocity of the domain boundary in one, two or three dimensions and (4) no cooperative interaction between domains. A (t) can be described as

$$A(t) = \left(\frac{t_c + t}{t_0} \right)^d \tag{2.8}$$

with t_c and t_0 being constants. After simplifying and implying that $r_c=0$ one can finally receive a formula which is referred to as the so-called Kohlrausch-Williams-Watts[94,95] type of equation:

$$Q(t) = 1 - \exp\left(-\left(\frac{t}{t_0}\right)^d\right)$$

(2.9)

In the special case of ferroelectric polycrystalline materials and if relative changes of domain area are considered (which means that not the full area switches), the equation can also be written as:

$$Q(t) = Q^* \cdot \left[1 - \exp\left(-\left(\frac{t}{\tau}\right)^\beta\right)\right]$$

(2.10)

This type of equation is called a stretched exponential function. Q(t) is the amount of switched domains, Q^* is the amount of switched domains at infinite time, t the timescale of the experiment, t_0 (or τ) the typical relaxation time and d or β the so-called stretching exponent which characterizes the dimensionality of the switching process. If homogeneous nucleation is assumed, β is replaced by $\beta+1$.

The model is linked to Avrami's theory of phase transitions, where an exponent also describes the dimensionality and the mechanism of switching[88]. If the mechanism is simple and consistent in the whole sample, we expect an integer number to describe the dimension of growth, which results in a simple exponential relation. There are two possible explanations why this simple form can transform into a stretched exponential response[95]: the first explanation is a broadened response for all regions of the sample, the second possibility is a distribution of response times[96]. As a result, this also leads to a stretched response of the sample. To describe the switching processes in ferroelectric materials, it is more likely to describe the stretched nature of the response with a distribution of relaxation times. When thinking about domains in a polydomain material, it is not surprising that some domains show a different response than others, as they are present in different sizes and configurations. The stretched nature of the exponential function

is thus due to a distribution of domain sizes and orientations because this distribution leads to inhomogeneous growth speeds of the domains[97,98].

According to Avrami's model, an exponent of 1 describes simple one-dimensional growth; exponents larger than one correspond to growth in more than one dimension. When considering domain structures in particular, the maximum exponent should be one, as normally stripe domains are present in the material, which only have one natural growth direction. Very often, exponents smaller than 1 can be found in ferroelectric materials. This can be explained by not only considering linear growth of the domain walls, but also some random growth fluctuations of segments of domain walls that are involved and might also occur in opposite direction to the growth[99]. Keeping this in mind, β can also be linked to the randomness of the domain distribution in the material, the higher β, the more "ordered" is the domain structure[100]. A detailed view on stretched exponential theory, its physical meaning and its history can be found in the review of Chamberlin[95].

There are also other mathematical descriptions of domain switching which sometimes appear in literature and will only be briefly mentioned here. For times t that are much smaller than the typical relaxation time τ, the stretched exponential function reduces to a simple power-law description for mathematical reasons[93]:

$$P(t) = P^* \cdot \left[1 - \left(\frac{t}{\tau} \right)^{\beta} \right] \tag{2.11}$$

This relation is also called the Curie-von Schweidler[101,102] relationship and can in some cases describe the whole switching process in highly ordered systems[95].

In some other works, a logarithmic decay function is used to describe the decay of polarization[103], which is only possible when β is small:

$$P(t) = P^* \cdot \left[1 - \beta \ln \left(1 + \frac{t}{t_0} \right) \right] \qquad\qquad \textbf{(2.12)}$$

Finally, one should mention that not only relaxation in ferroelectric materials is described by stretched exponential behavior, but also many other processes like dispersive diffusion[104], strain relaxations after an external excitation[103] and relaxations in glasses[105] and constrained systems[95].

2.5.2 Experiments

Different kinds of experiments on ferroelectric materials have been performed to describe the switching kinetics. They can briefly be classified in short-term and long-term experiments. Most of the long-term experiments were done on the timescale of days or longer to study the polarization loss in thin films with the background of the application as ferroelectric memory (FERAM). The fast experiments are often performed with a more general background or to get more information about the writing process in FERAMs.

A general trend that is visible in the literature is the presence of two relaxations that happen on different timescales. The faster relaxation was discovered by Benedetto et al in 1992[106], when the polarization of a PZT capacitor was measured depending on the read/write delay. The same fast relaxation was later reproduced by other authors[77,93,107-109], most of the times this fast relaxation could be described using a power-law or logarithmic relationship, but sometimes also with a stretched exponential. An example for a measurement of polarization changes with time in a PZT capacitor at different voltages is given in figure 2.20. The effect was usually explained by 90° domain wall relaxation and depolarizing fields.
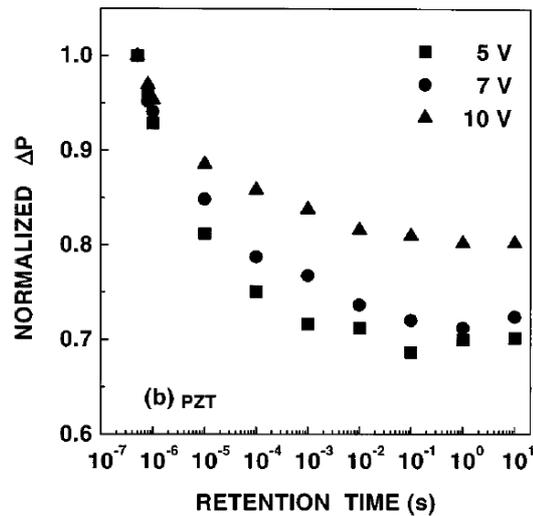
Figure 2.20: Polarization retention for a PZT capacitor and different switching voltages[108]. As seen in the plot, the polarization decreases relatively strongly in the first micro- to milliseconds. This fast relaxation is found in a similar way in many experiments.

On the other hand, studies exist which focus on the long-term retention loss of ferroelectric capacitors[75,110,111]. In this case, the mathematical description of the loss is mostly a stretched exponential function with a relatively low stretching exponent of 0.1 to 0.5. Most of these studies are done with scanning methods such as AFM or PFM, where domain growth can be directly measured. An example for the data obtained in such an AFM study can be seen in figure 2.21.

In some studies, it is also found that the amount of slow switching compared to fast switching increases with increasing cycle number of the capacitors[100]. As an explanation, a combination of random fields of ionized defects, clustering of point defects and cascaded switching due to the polycrystalline nature of the material is proposed.
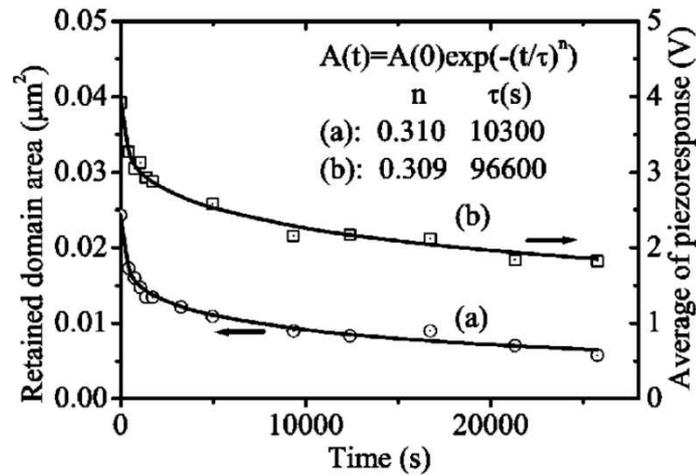
Figure 2.21: Domain area depending on time measured by PFM on a thin PZT film[75]. A long-term relaxation is found and can be described using a stretched exponential function.

To summarize all studies on domain dynamics, two different switching processes on different timescales exist, among which especially the fast switching is of interest for our study. Often, this is described by a simple exponential or power-law function, but also by a stretched exponential decay. The stretching exponent, which describes the dimensionality of domain growth and the degree of order of the domain structure, is usually smaller than 1 and often in the regime close to 0.5. For our study, we still have to keep in mind that most of the literature data was collected for thin films and thin film capacitors.

2.6 Objective of this work

Piezoelectrics are nowadays used in many applications where they are exposed to cyclic loads over a long lifetime of up to 10^9 cycles. There is an increasing interest in understanding the time-dependent response of piezoelectric actuators. Studies have been performed on model systems, but the direct response of an actuator operating under application conditions has not been investigated so far. To understand the application, it is however crucial to study real systems which are more

complex because they contain mechanical and chemical inhomogenities, interfaces and different phases. Also, it is completely open how dynamic processes of a material might change with the fatigue state or contribute to fatigue behavior.

In this study, a new synchrotron-based method to perform time-resolved experiments of piezoelectric actuators will be shown. The actuator is driven under comparable conditions like in the application as diesel engine fuel injector. The direct response of different areas of the actuator can be studied with a time resolution of 1 μs. Precise mechanical tables and a focused beam even enables us to study changes in single grains at different positions of the actuator and thus understand the influence of the inhomogeneous intrinsic structure of the material. This is the first time such experiments are not only performed on model systems, but take the real application conditions into account and try to rebuild these conditions as close as possible.

With this work we want to investigate dynamic processes that occur in a piezoelectric actuator during switching and to understand the influence of the ceramic-electrode interface. With selected methods, we want to look at different time- and lengthscales. The goal is to get more details about dynamic processes and possible fatigue mechanisms and understand how the actuator responds under different boundary conditions. This might help to give data for simulation of these devices and to find ideal application conditions.

3 Experimental methods

3.1 Sample types

Altogether, five types of samples were used for different diffraction experiments. An overview is given in figure 3.1. A detailed description will follow below.
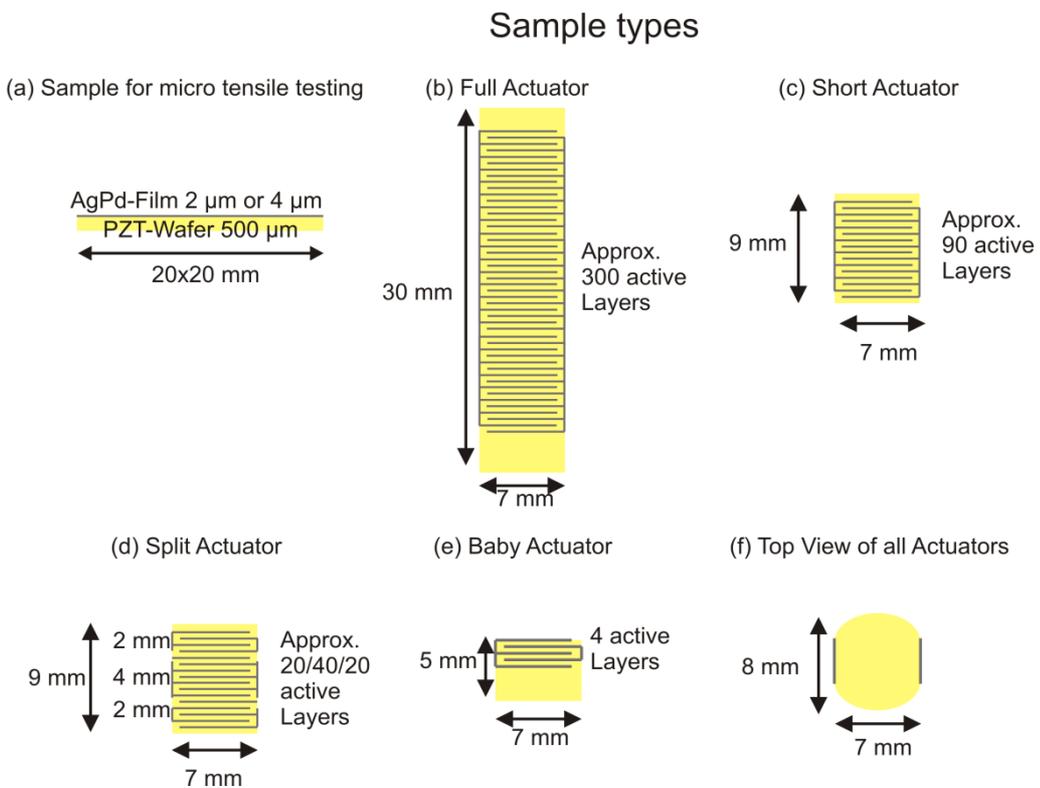
Figure 3.1: **Overview about all sample types used in this work. (a) Wafer-like samples with only one or two electrode layers with 2 μm thickness each. From this, the micro-tensile samples were prepared. (b) Whole actuator as used in diesel injection systems. First experiments on the big sample chamber were done with this. (c) Short actuator for new sample chamber. The preparation was simply done by cutting of whole actuators. (d) Split actuator, prepared from a short actuator. The electrodes were partly cut. (e) Baby actuator for special X-ray experiments to study lattice planes that expand parallel to field direction. (f) Top view to show the shape of all actuator samples.**

All samples were made of a PZT of the composition $PbZr_{0.53}Ti_{0.47}O_3$ doped with several different elements. The electrode material was Ag70Pd30. The ceramic thickness was 90-100 µm per layer, the electrode films were 2 microns thick. The sample production line was the same as for the actuator used in injection systems, which is described in chapter 2.3.3. and by Randall et al.[32] Sintering was carried out at 1000 °C followed by a pre-polarization step at 150 °C where the ceramic was cycled 10^5 times.

With this basic process, a variety of samples was fabricated. For micro-tensile testing, a special square-shaped sample with 20x20 mm² size was prepared (figure 3.1 (a)). On 5 layers of PZT that were laminated without electrode material, one or two electrode films were printed leading to a total thickness of 2 and 4 µm, respectively.

For first investigations in a large sample chamber, experiments on the full actuator, the original 30 mm long device used in fuel injection systems, were done. The top and bottom of the actuator consist of an inactive area with no electrodes; solder spots for electrical connection are located at the bottom of each side. The external electrodes are made of copper and soldered to the shoulders of the device. In operation, the total elongation is approximately 0.15-0.2 % (around 40-50 µm). The capacity of the full actuator is around 3.4 µF.

For later experiments, a short actuator with only 9 mm length (see 3.1 (c)) was used. With this sample, a much more compact sample chamber could be built and experiments on an Eulerian cradle with maximum geometric flexibility were possible. To prepare the short actuators, a large actuator was cut into pieces with a diamond wire saw. Later, we used a special split actuator setup where the electrodes were cut at certain positions also using a wire saw.

Final experiments were done on a special smaller actuator we refer to as baby actuator. Only 4 active layers were laminated on top of a 4.6 mm inactive PZT

bottom. Keeping the movement of the sample as small as possible was crucial for the stability on the position-resolved experiments at ESRF. By transmitting through the top electrode, lattice planes oriented perpendicular to the electrical field direction could be studied, which are supposed to show expansion in contrast to the contraction which we measured at lattice planes parallel to the field direction.

3.2 Microscopic Investigations

3.2.1 Preparation

For all metallographic investigations, the samples were prepared by grinding starting with a grid of 240 on a Leuth-Rotor 3 by Struers. Further grids were 500, 1000, 1200, 2400 and 4000. For each step the grinding time was around 3 minutes. After that, a diamond polishing of 6, 3 and 1 μm (Labopol 5, Struers) was applied to further improve the surface quality. Minimum polishing time was 3 minutes per step. For the EBSD measurements, polishing was extended and a chemical polishing with Mastermet® solution was added for a better pattern quality. Due to the slight surface etching of the agent, thin oxide films could be removed.

3.2.2 Light Microscope

The light microscope investigations were performed on an Olympus BH2 microscope in reflected light mode. The pictures were taken using the ProImage 3.2 software package and a Jenoptik camera. Different lenses from 5x to 50x were used with an ocular of 10x magnification.

3.2.3   Scanning Electron Microscope (S EM)

Several polished samples were analyzed by a LEO 1530 VP SEM using voltages of 15-20 kV. Most investigations were done for the purpose of finding good positions for EBSD analysis. Pictures were taken with the in-lens and an RBSD (Rutherford backscatter) detector. The sample was partially coated with silver paint to avoid electrical charging of the surface.

3.2.4   Focused Ion Beam Microscope (FIB)

In addition to the SEM experiments we also performed investigations in the focused ion beam. The microscope we used was a FEI FIB 200 with a liquid gallium source. Polished and unpolished samples were studied with different magnifications. The FIB was also used to mill into the sample and take cross-section pictures of the electrode material.

3.3   Diffraction Methods

3.3.1   Synchrotron Experiments

Experiments on lab sources were only performed for testing purpose; all important X-ray diffraction results in this thesis were collected on synchrotron radiation facilities. Synchrotrons make use of the fact that relativistic electrons, which are accelerated along a radial path, emit radiation. Elder et al.[112] discovered this in 1947. Since the late 70s of last century, science started to use that kind of radiation for the creation of X-rays of high brilliance. The brilliance is a relative figure-of-merit to describe the quality of x-ray beams and is typically expressed as photons/mrad²/mm²/s in the relevant part of the spectrum. Modern X-ray sources offer brilliances up to 10 orders of magnitude higher than conventional lab sources.

The synchrotron experiments were performed at two different synchrotron radiation facilities, the Angströmquelle Karlsruhe (ANKA) and the European Synchrotron Radiation Facility (ESRF). ANKA is a relatively small storage ring with a diameter of approx. 30 m and a storage ring energy of 2.5 GeV[113]. Experiments were done at the surface diffraction beamline operated by the Max-Planck Institute for Metals Research[114]. The optical setup of the beamline is shown in figure 3.2. The main experiments at ANKA were the micro tensile tests (see chapter 3.4) and part of the time-resolved experiments (3.5.2). The beam energies were between 8 and 10 keV, the beam at the sample distance was focused to approximately 0.25x0.5 mm² spot size.
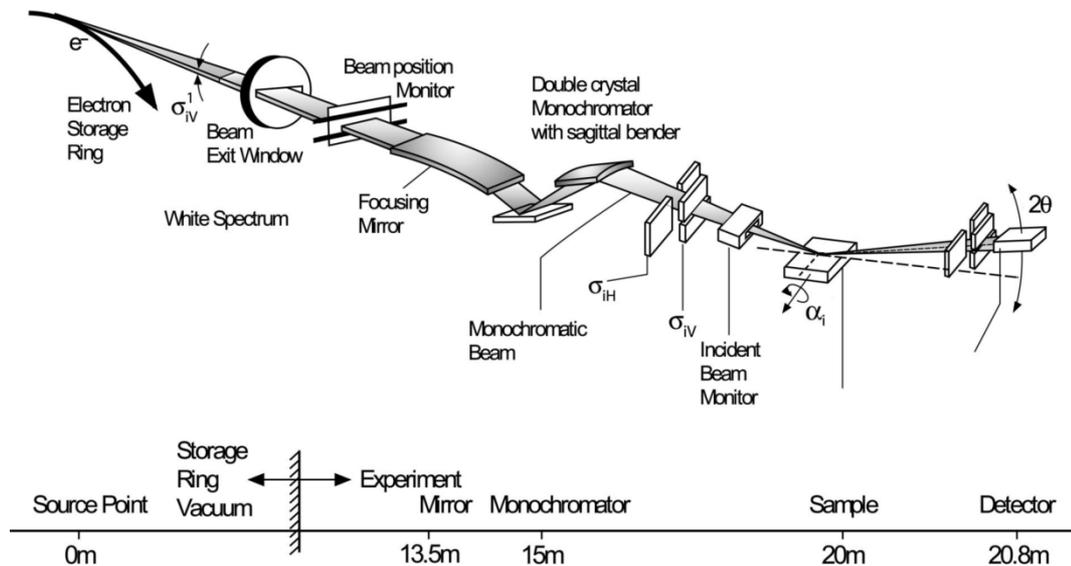
Figure 3.2: Basic setup of the surface diffraction beamline at ANKA[115].

Some more complex time-resolved diffraction experiments with better spatial resolution were performed at ID01[116] at ESRF in Grenoble[117]. The beamline is equipped with an undulator and offers an energy range between 5 and 35 keV. 16 bunch mode and 1/3 multibunch filling mode were used. Our experiments were done with 10 keV radiation energy. The setup of the beamline optics is shown in figure 3.3. With a focusing monochromator and 16 compound reflective lenses a

beam size of approximately 4x6 μm² on the sample position could be achieved. A more detailed experimental description will be given in chapter 3.3.2.
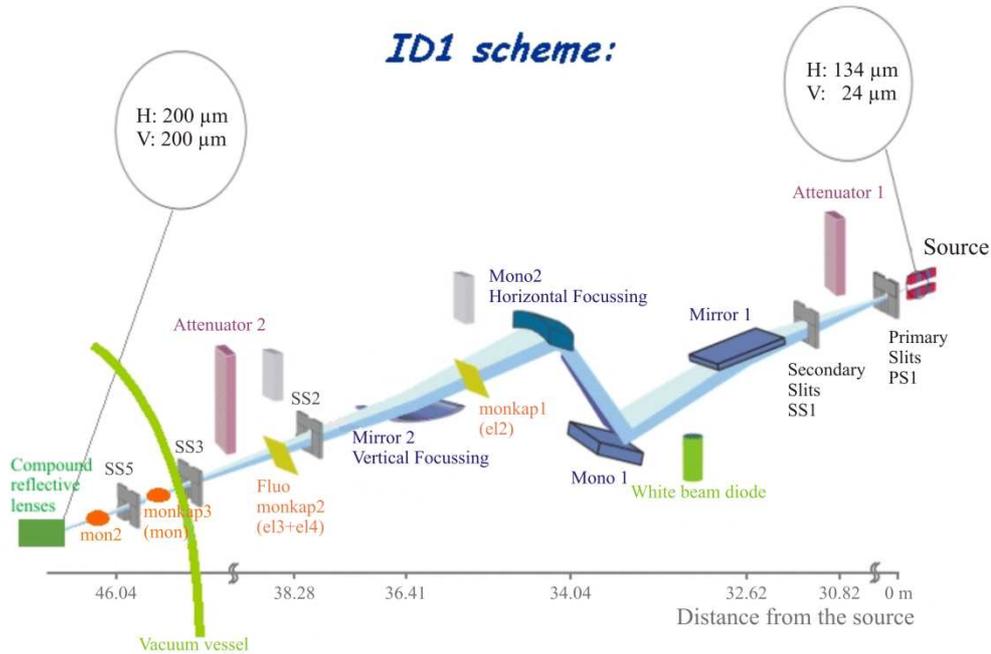
Figure 3.3: Overview on the optics' setup of ID01[118]. Behind the monochromator and mirror close to the sample, compound reflective lenses can be mounted to focus the beam.

Different kinds of scans were used to characterize our samples. Bragg's law[119] describes the interrelation between the diffraction angle θ and the lattice plane distance d:

$$n\lambda = 2d\sin\theta \qquad (3.1)$$

with the photon wavelength λ and the order of the reflection n. A series of lattice planes is described by the Miller indices h, k and l which can be related to the lattice plane distance d and the unit cell axis a, b and c by the following formula:

$$d_{hkl} = \frac{1}{\sqrt{\left(\dfrac{h}{a}\right)^2 + \left(\dfrac{k}{b}\right)^2 + \left(\dfrac{l}{c}\right)^2}}$$ (3.2)

When the incoming angle θ and the diffracted angle 2θ are scanned at the same time with the ratio 1:2 this is called θ-2θ scan; the peak position 2θ of a certain reflection represents the distance of the respective lattice planes. On the other hand, scans where the diffraction angle 2θ is kept constant and one of the tilting angles of the sample is scanned are called rocking scans. If the scan covers two angles at the same time, we receive a three-dimensional dataset. These scans are called mesh-scans.

3.3.2 Time-resolved X-ray Diffraction

Synchrotron radiation makes it possible to run experiments with higher resolution, intensity and in shorter times compared to lab sources and opens the field to a completely new type of time-resolved X-ray experiments[120]. The high brilliance and intensity make it possible to study phenomena on timescales down to picoseconds[82]. Time-resolved diffraction experiments can for example be used to study chemical reactions, phase transformations or the structural response of a material to an external excitation, as we did in our study. The X-ray signal can either be collected continuously with a multichannel scaler card or only in certain selected timeframes synchronized but delayed with the excitation, which is called pump-probe experiments[121].

Synchrotron radiation has an internal time structure that limits the maximum time resolution. Electrons are arranged in bunches with a usual bunch length of 25-100 ps while bunches are separated by several nanoseconds. In our case, experiments were done with a time-resolution of 1 µs, so the incoming beam of the synchrotron can be considered as continuous photon source. This is the case for continuous filling (electron bunch separation of 2.8 ns, see figure 3.4) as well as in 16

bunch mode with bunch separation of 176 ns where 5 or 6 electron bunches are within the 1 μs counting time. As our data always is monitor-normalized, changes in the incoming intensity due to different bunch numbers or the decay of the ring current are averaged out.
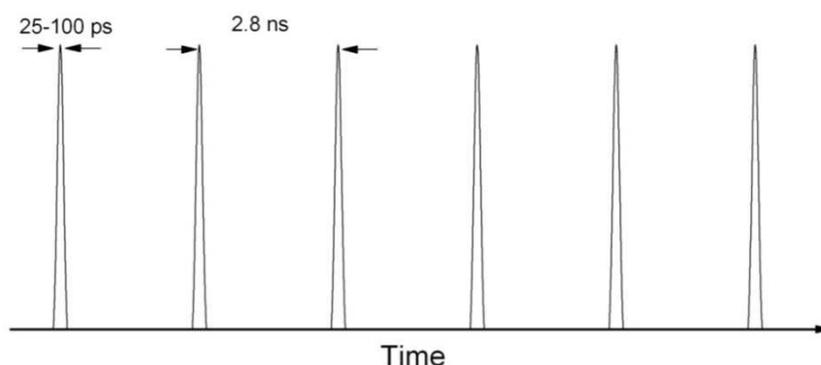
Figure 3.4: Typical bunched time-structure of synchrotron radiation.

If the detection signal is sent to a multichannel counting card (in our case the SIS-3820 by Struck Innovative Systems), each time slice of a certain fixed length can be accumulated on an individual channel. This is called histogram mode. The start of each counting sequence is triggered by or synchronized to an external pulse. A macro to work with the SIS-3820 counting card in histogram mode was written in SPEC diffraction software.

First experiments were performed with the full and the short actuator, which were switched as a whole. A scheme of the basic components of the experimental setup is given in figure 3.5. On a PC equipped with SPEC, the parameters for the counting card like number of accumulations, counting interval time and number of intervals could be set. When starting the counting sequence, a trigger signal from the counting card started the accumulation by triggering an additional delay generator (DG535 by Stanford). After 1 ms of holding time, a pulse from the delay generator started the voltage amplifier, which was at the beginning SL400-25PDS3C by Scienlab company. Later this part of the setup was modified, details

are given below. The adjustable voltage was usually set around 150V. The ramp was chosen between 1 and 5 V/µs.

The pulses from the delay generator and the amplifier were checked with an oscilloscope as well as the temperature of the sample with a Lakeshore 330 temperature control system. During cycling, the piezo usually heated up to approximately 45-60 °C. Equilibrium was reached after some minutes, but already very soon a temperature close to the final state was obtained, so the temperature during an experiment can be considered as constant. For some experiments at higher temperatures, a heating cartridge with temperature controller was used.
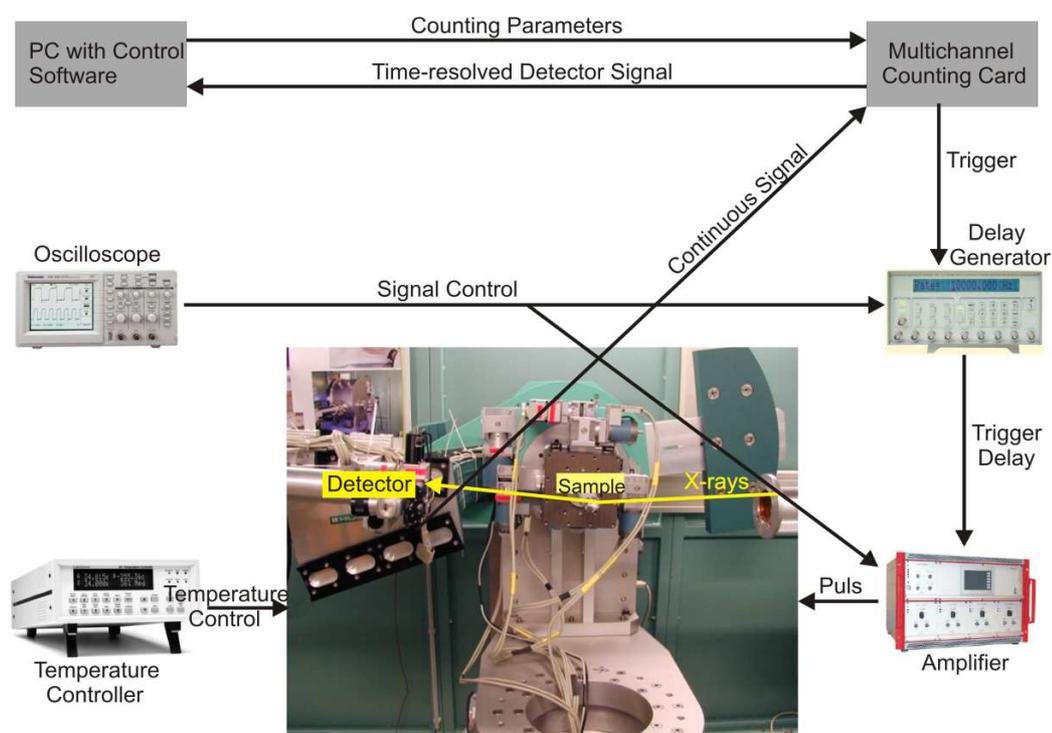
Figure 3.5: Schematic of the electronics used to perform experiments. From a PC, the counting parameters were sent to a multichannel counting card. A trigger from this card started the experiment, the delay generator controlled the time until the pulse was applied and the repeating frequency. The detector signal was fractionized into the designated time channels by the counting card and finally read out by diffractometer software.

First experiments were done with a NaI scintillation counter, which can be linear-corrected for count rates up to 400,000 counts per second (cps). For later experiments at ANKA and the ESRF beamtimes, an Avalanche Photodiode (APD) for higher count rates up to 2,000,000 cps was available. We always tried to use the fastest available detectors at the given energies as high count rates were crucial for good statistics in the time-resolved experiments. The detector signal was continuously collected and electronically split up into the different time channels of the counting cards' histogram space. Necessary deadtime corrections were applied in the data analysis software which will be mentioned later.

An overview of the diffraction geometry and all angular degrees of freedom used in the experiments with the full, short and split actuator is given in figure 3.6. θ is the tilting angle with a rotation angle parallel to the sample surface and perpendicular to the incoming beam. χ tilts the sample along an axis which is oriented parallel to the sample surface and parallel to the direction of the incoming beam while φ is the angle of rotation with the rotational axis being perpendicular to the sample surface and the incoming beam.
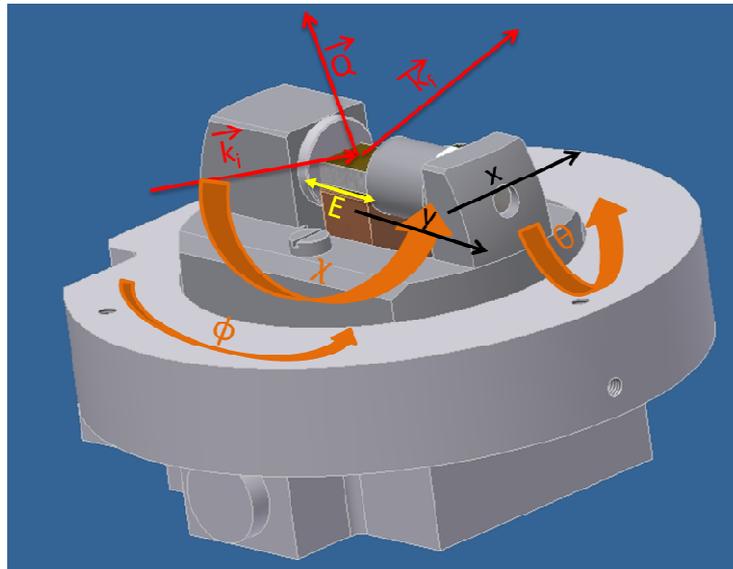
Figure 3.6: Sketch showing the diffraction geometry and the definition of all angles and directions used in the experiments.

Two sample chambers, one for the full and one for the short actuator, were constructed. The requirements for both were similar; the sample had to be mounted in a frame to apply the pre-stress, which could be adjusted by a screw mechanism. The amplitude of pre-stress could be measured by the deformation of the spring the sample was operating against because the spring constant was known. A heating option was included in the copper block below the sample operating up to temperatures around 300 °C. On the sample, a PT 100 temperature sensor was mounted. Electrical feedthroughs were necessary for the temperature sensor and the control of the piezo. Finally, a cover to work in a protective gas atmosphere (helium) was implemented as well as gas inlet and outlet valves.

Photos of the two sample chambers can be found in figure 3.7. For experiments with the full actuator, a big chamber to be mounted onto the large Huber tower at ANKA beamline was constructed. The frame where the sample was fixed was the original test frame for fatigue experiments at Bosch (see figure 3.7 (a)).
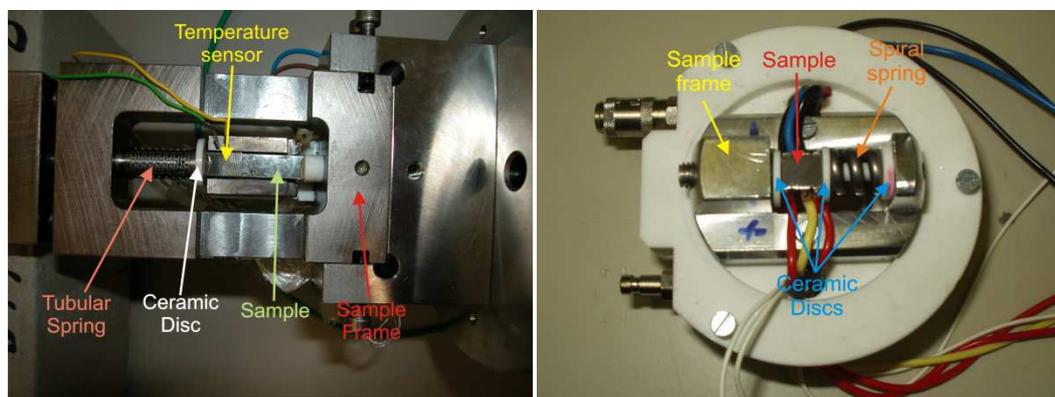
Figure 3.7: Sample chambers. (a) Big sample chamber for experiments on the full actuator. (b) Small sample chamber for the short and the split actuator setup, which is shown in the picture. The ceramic discs seen in the right picture were later replaced by discs made of epoxy circuit board material. On one of these two epoxy discs, a piezo sensor to measure the system vibrations was attached. The spring was exchanged by a bulk steel block to reduce vibrations.

The actuator was operating against a tubular spring with a spring constant of 1kN/mm. The actuator was ground and polished to prepare a flat surface for X-ray investigation. A silicon based coating was sprayed on the sample to prevent electrical sparkover. The sample chamber could be covered with a steel cylinder with a Kapton window as pathway for the X-rays. A heating cartridge could be introduced in the copper block that can be seen below the sample. The electrical feedthroughs necessary to provide the voltage for the sample were included on the bottom of the chamber. Temperatures up to 300 °C could be reached with this setup.

The construction principle of the second sample chamber is similar; a new frame was constructed to mount smaller samples. As counterpart for the piezo, a tubular spring, a spiral spring or a bulk steel block could be mounted. Feedthroughs for 3 cables on each side of the actuator as well as a temperature sensor were available on the bottom of the chamber. The chamber was covered with a PEEK dome as used in the DHS-900 heating chamber from Anton Paar company. To raise the temperature if necessary, a heating cartridge was buried in a copper block below the sample.

Experiments with the baby actuator were done with a commercially available sample chamber which was adapted to our experiments. The BTS-basic temperature stage from mri company enables heating and cooling in large temperature ranges and is equipped with a beryllium dome to measure under vacuum and protective gas conditions. The chamber can be adapted to different applications. In our case, we used the low-temperature setup with a nickel strip heater, where temperatures up to 400 °C or also down to -180 °C can be reached. Temperature was controlled by a Eurotherm 2404 controller. The setup with the baby actuator as used at ANKA can be seen in figure 3.8. The sample had to be positioned carefully in the centre as no x-y stage was available in this setup. Electrical feedthroughs were available to connect the sample with the external voltage. The sample height

was adjusted by three screws, which were bearing on the base plate below the chamber.
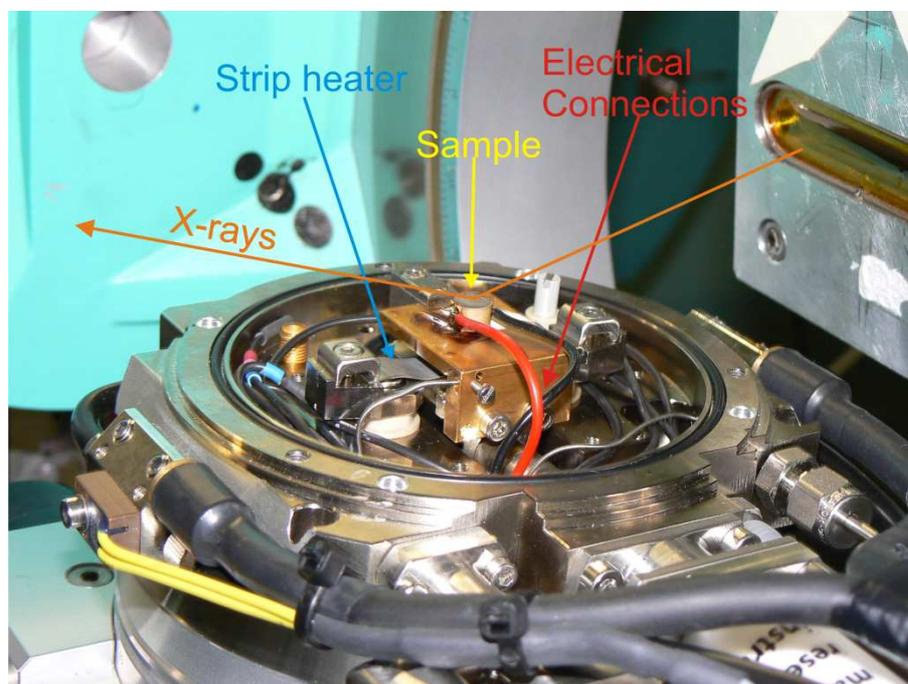
Figure 3.8: Photo of the mri BTS basic sample chamber used to perform experiments with the baby actuator. Usually, the chamber is covered with a beryllium dome. Feedthroughs for the electrical connections are available. A nickel strip heater is used to work at temperatures up to 400 °C.

Between 10,000 and 100,000 cycles were usually accumulated per datapoint in the time-resolved experiments. Often, a whole mesh in θ-2θ and θ direction was recorded (see figure 3.9). To select peaks, a rocking scan was performed; a peak with high intensity was selected and the peak centered in all tilting directions. The counting interval was usually set to 1 μs, which is the minimum interval time due to an internal limitation of the counter card board frequency. A measurement started with a waiting time of 0.2 to 1 ms before the voltage was switched on, after 5 ms holding time, the voltage was switched off again and another 4-5 ms waiting time to measure potential relaxations was included. This adds up to a repetition rate of 89-100 Hz, so that a usual measurement of a whole mesh with

around 20000 accumulations per datapoint took 6 hours. The number of repetitions was adapted to the desired measurement time.
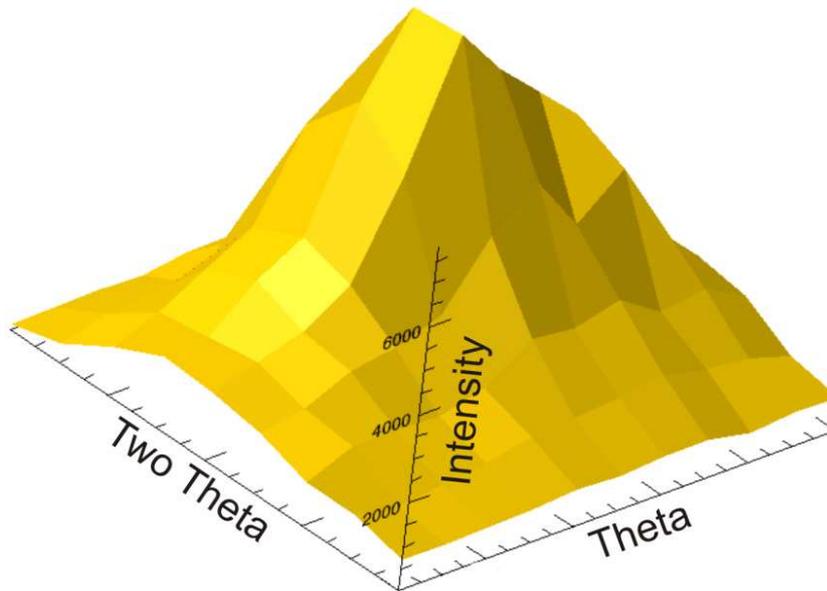
Figure 3.9: Example for a typical mesh recorded in time resolution. On each Q point on the mesh, a series of several ten thousand accumulations was performed to collect the data in histogram mode. Altogether, a dataset of usually (11x11x10000) points was obtained.

Almost all of the experiments were done at the (101) peak, which showed the highest intensity and thus enabled the fastest measurements and best counting statistics. Count rates on the peak were between 300,000 and 2,000,000 counts per second. At ESRF, higher count rates were achieved. Figure 3.10 shows a schematic view on the unit cell of PZT and how it changes when an electrical field is applied. The (101) planes should not only change their distance as a consequence of the piezoelectric effect, a tilting of the lattice planes should also be measured because the ratio between the lattice parameter changes.
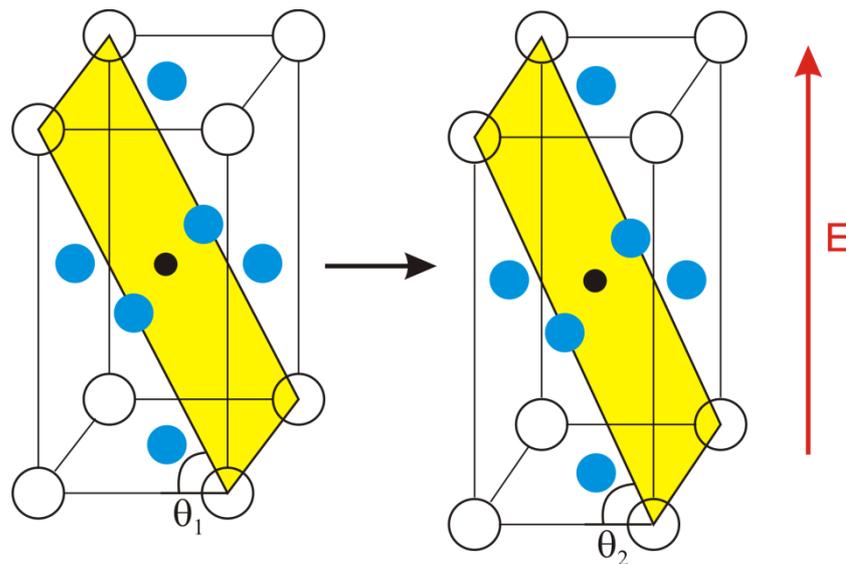
Figure 3.10: Sketch of the unit cell of PZT with the (101) plane marked in yellow. If an electrical field is applied, the lattice plane distance of the (101) planes should change, but also a tilting of the (101) planes can be measured (θ1≠θ2).

In first experiments, very pronounced oscillations of the intensity signal were found. This could be attributed to the excitation of eigenmodes of the sample and the surrounding, e.g. the spring and the sample frame (see chapter 7.1). As this effect was stronger than potential relaxation effects which we wanted to measure, a new setup was developed where the actuator was split up into three parts (figure 3.11). The inner part was of the same length as the sum of the outer two parts. Voltage was first applied to the outer actuators to achieve a pre-pressurized state (b). Then the voltage of the inner part and the two outer parts of the actuator were applied 180° out-of-phase. In this setup the total length of the system did not change anymore during cycling. The second advantage especially for the position-resolved measurements at ESRF was that in the centre of the sample a region was present which did not move during the experiment. This is necessary when working with a small beam spot and investigating single grains.
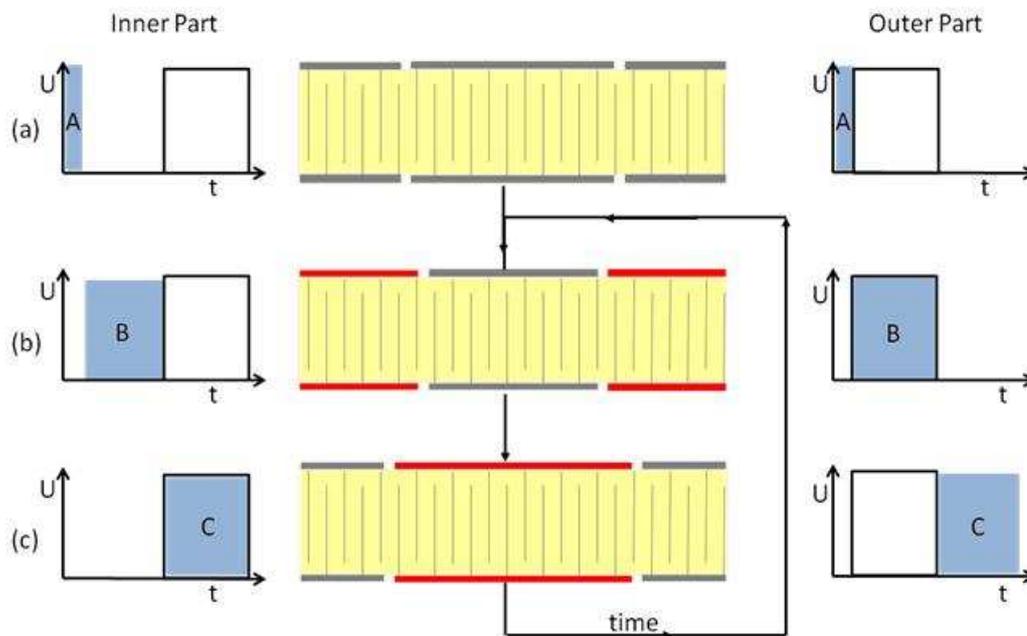
Figure 3.11: Schematic principle of the split actuator setup. The voltages of the inner part and the two outer parts of the actuator are applied 180° out-of-phase. With this setup, the total length of the whole actuator does not change and thus no mechanical resonances of the frame are excited. The blue box symbolizes the actual time; the corresponding shape of the actuator is shown in the centre of the figure. The states (b) and (c) are repeated continuously during the experiment.

Working with the split actuator also made it necessary to change the electronic setup, as now at least two amplifiers, one for the outer two parts and one for the inner part, were necessary. To do so, we used three TA 2400 TX-K audio amplifiers coupled with a function generator to provide the pulse signal. The amplifiers were triggered at the same time, but two of them received opposite pulses compared to the first one. Figure 3.12 shows a pulse diagram to explain the electronic setup we were now using for the cases of the baby actuator ((a), one amplifier) and the split actuator ((b), three amplifiers). The SIS 3820 counting card starts with a TTL pulse which is directly sent back to the card to start the counting sequence. After a programmed delay in the range between 100µs and 1 ms, the Stanford DG535 pulse generator starts the TGA 1240 function generator which finally controls the amplifier supplying the sample with the desired voltage. A piezo bi-

morph sensor was used to find the point of minimum vibrations. Such a sensor consists of two PZT layers poled in opposite direction and is very sensitive to bending. The voltage signal of this sensor was taken with an oscilloscope and the minimum voltage corresponded to the least bending of the bimorph sensor. With the split actuator, the vibrations could be reduced by a factor of 20. As the amplifiers only provided an alternating signal of ± 100 V, a pre-amplifier with a voltage of up to +100 V was used to shift the signal into the required signal range of 0-200 V maximum pulse height.
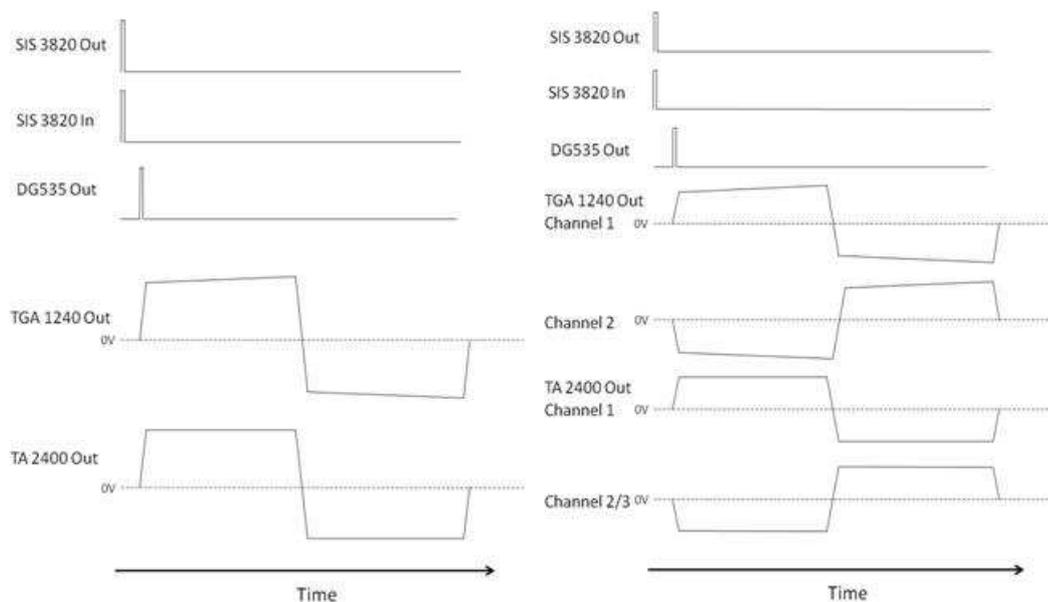
Figure 3.12: Pulse Diagram to explain the electronic setup used in experiments with the (a) baby and (b) split actuator. When using the split actuator, three TA 2400 audio amplifiers are used, where the signal of two of them is 180° out of phase with the third. This is controlled by programming two different waveforms in the function generator.

Figure 3.13 shows a circuit diagram of the complete setup. In the centre of the figure, a plan of the box is shown which is used to shift the voltage from ± 100 V into the range of 0-200 V by using a DC amplifier combined with the audio amplifiers. The BNC connectors can be used to study the voltage and current signal

of the box. In case of the split actuator where three amplifiers are connected to the sample, three adapter boxes are needed.
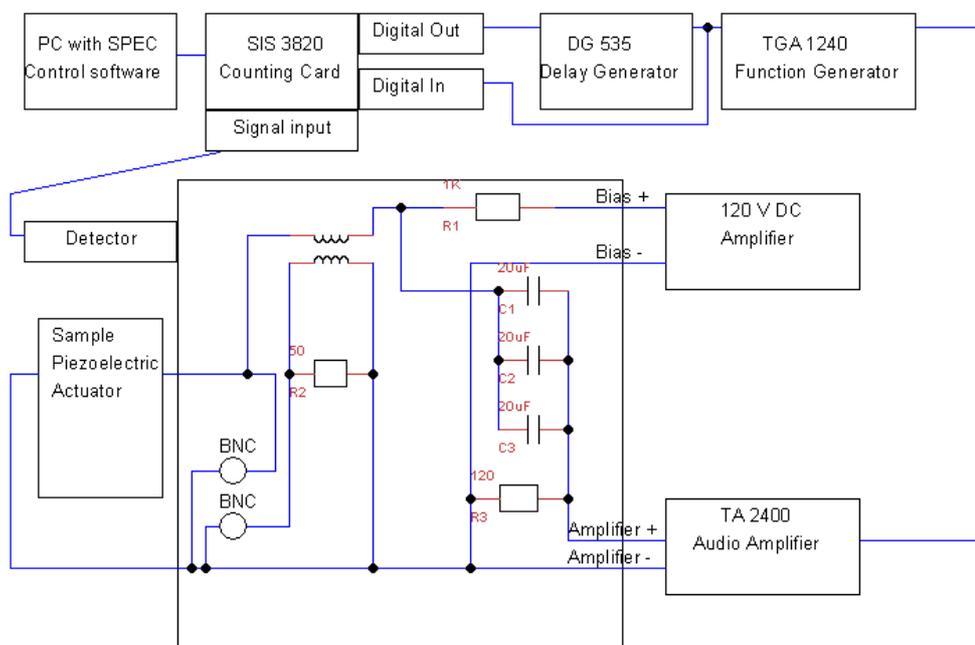
Figure 3.13: Circuit Diagram of the electronics setup used in the experiments. The black square symbolizes the adaption box which changed the voltage from originally ± 100 V to 0-200 V.

At ESRF, we first performed time-resolved and position-resolved measurements of the split actuator. We studied the response of single grains at different sample positions and compared potential relaxation effects. For this experiment, the second sample chamber was equipped with Huber x-y-z stages with high resolution and repeatability below 1 µm. The resolution was 2.5 µm in x-y directions and 50 nm in z-direction. For the second ESRF beamtime, the x-y resolution was improved to 0.25 µm by implementing a gearbox. By scanning the sample for AgPd-peaks, a good positioning with respect to the electrodes could be achieved so that grains at special sample positions could be selected by performing rocking scans and x-y scans. Grains had to be chosen carefully; often the intensity was not sufficient for time-resolved experiments.

56

Later experiments at ANKA and ESRF were done with the baby actuator. The baby actuator was only built with four active layers to ensure minimum movement of the sample, which was of particular importance when working with the small beam spot at ESRF. Advantages of this setup was the mechanical stability, the disadvantage was that no x-y stages could be included in the setup on the Eulerian cradle at ANKA. Also, the sample height had to be adjusted manually. At ESRF, the setup could be mounted onto a large Huber tower where mechanical tables were available.

First experiments with the baby actuator revealed that the absorption of the X-ray beam due to the AgPd top electrode was too high, as the PZT peak intensities were remarkably lower than the intensities measured for the split actuator. To solve this problem, several etching methods were used. Finally, the top electrode was partially removed by argon sputtering in a reactive ion etching chamber. The parameters were 300 W plasma power and 1 hour of sputtering time. The success of the sputtering process was verified using X-ray diffraction, where the peak intensities of AgPd and PZT before and after sputtering could be compared well (figure 3.14). A clear decrease of the AgPd signal and an increase of PZT intensity can be seen.
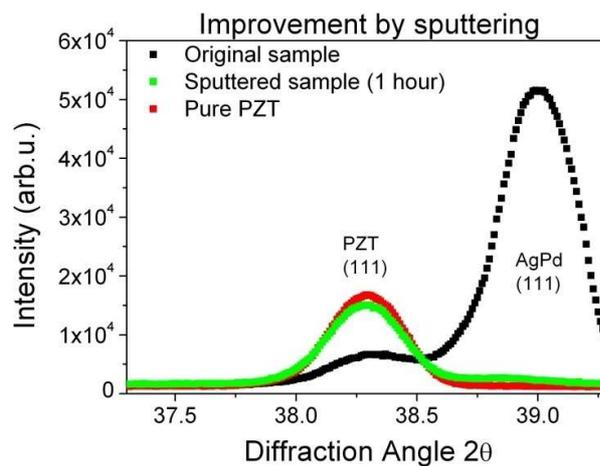
Figure 3.14: Intensity changes in the signal of the AgPd electrode material and the PZT when sputtering the electrode in the RIE chamber.

When doing experiments with the baby actuator setup at ESRF, there were still stability problems during the experiment which potentially could be caused by our setup. But also, there were indications that the incident beam was moving, especially due to problems with the monochromator stability. Even when we did not change the sample position, peaks often had to be readjusted during the experiment. After several trials to locate the instable component of the setup, we tried to simplify the experiment as much as possible. Finally, only a bulk steel block underneath the sample, which was glued directly on it, was used. Still, all translational and rotational positioners were available, but the sample chamber was removed. The sample was covered with a plastic bag filled with helium protection gas to minimize radiation damage. Now, heating was not possible anymore. Even with this setup (figure 3.15), we still had to readjust the sample position in direction parallel to the X-ray beam after each measurement point on a mesh. For further details on this stability issue, see chapter 7.5.
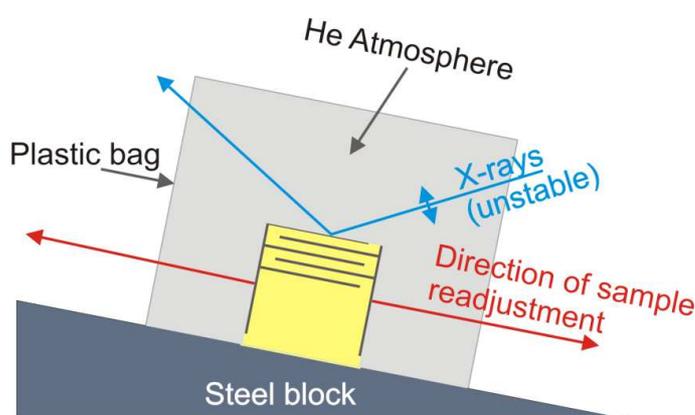
Figure 3.15: Setup with the baby actuator as finally used at ESRF. The sample is glued on a steel block and covered with a plastic bag for He protection gas atmosphere. Still, the sample position had to be readjusted manually during the experiment in direction parallel to the X-ray beam.

Later, a small test experiment in the lab was done to check whether the stability problems were caused by our setup or the beamline. The position of our setup was checked with a test gauge with sub-micron resolution. Even after the piezoelectric

actuator was excited for 2 days, no movement was found. An additional indication for the beam instability was the occurrence of "stripes" in the signal of single grains (see figure 7.23), whose relative intensities were unstable. The reason for these stripes was imperfections of the monochromator, and as they were changing in intensity, this was a clear indication that the incident beam from the storage ring or the monochromator were moving.

Main goal of the experiments at ESRF was the study of single grains at different sample positions. For this, different measurements of the time-dependent response of grains at the active and inactive area of the actuator were done for both the split actuator (first beamtime) and the baby actuator (second beamtime). Figure 3.16 gives an overview of the different sample positions studied in both beamtimes. In the baby actuator, we studied in addition a third position close to the electrode edge. At each point, grains were selected and centred and a mesh in θ and 2θ direction was recorded.
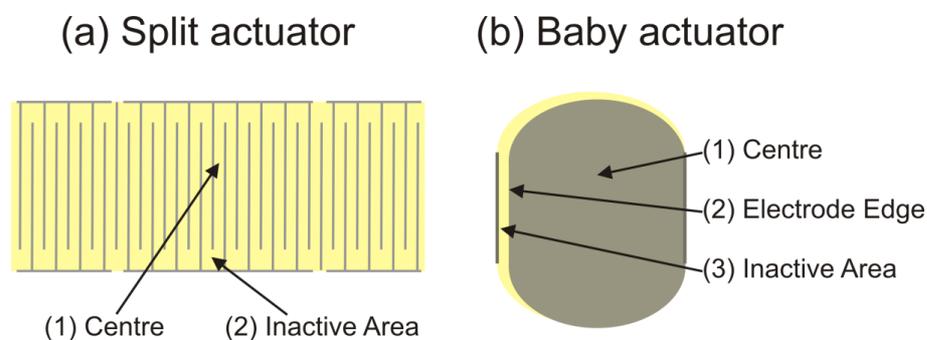
Figure 3.16: Different sample positions where grains were investigated in the ESRF beamtimes. (a) Split actuator, two grains were studied, one in the active and one in the inactive area of the sample. (b) Baby actuator, four grains at three different positions were studied, two in the centre area and one close to the electrode edge and in the inactive area, respectively.

Data was treated using the Interactive Data Language (IDL)[102] software package. A program was written to automatically read in the files at each datapoint of a mesh and to save the data in a 3D array. Some fitting and data treatment routines

were developed to fit peaks in both directions, smoothen the data, do monitor normalization, deadtime correction and save the fit parameters. Exporting parts of the data for further treatment in other programs was also implemented. With this program set, all necessary data treatments were possible. Peak fitting with Gaussian peak shapes showed the best agreement with the data compared to other peak functions. The fits allowed us to extract a time-resolved peak position. To fit the relaxations, especially in the data of the second beamtime, the data was exported to Origin, where better fit results were obtained. Fit functions were self-written and adapted to Origin fitting routines.

3.3.3 Micro-Tensile Testing of Thin Films

The synchrotron-based testing technique for thin films used in this thesis has been introduced by Böhm et al. in 2004[122]. The general idea is to deposit a thin metal film onto a polymer substrate and to perform in-situ X-ray stress analysis of the film during a tensile test. This method is the only known experiment to perform tensile tests on films down to 30 nm thickness.

To determine the stress state in a polycrystalline material by X-ray analysis, usually the $\sin^2 \psi$-method is used[123]. The general idea is to make use of the fact that in a strained sample the spacing of lattice planes depends on the orientation of the grain (figure 3.17). A plot of the lattice constant against $\sin^2 \psi$ (the tilting angle) will result in a linear relation from which one can determine the residual strain in the tested material (if the material is isotropic and untextured). Using the elasticity tensor, the strain can be determined from the measured stress.
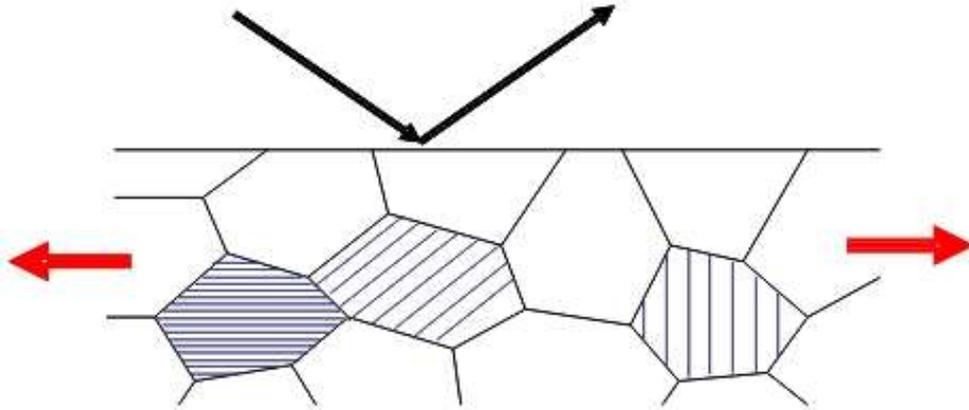
Figure 3.17: Principle of the sin²ψ-method. In a strained sample, the distance of lattice planes perpendicular to the direction of load increases while it decreases in planes parallel to the load.

In contrast to that, the method of synchrotron-based micro-tensile testing uses the in-plane rotation angle ϕ (sin²ϕ-method). The sample is investigated in transmission instead of reflection geometry. If we consider the lattice spacing (figure 3.18(a)), it also depends on the in-plane orientation of the grain. A CCD area detector is used to record the whole Debye-Scherrer rings simultaneously. From the elliptical distortion, the lattice strain in both longitudinal and transversal direction can be determined. The stress is calculated from the measured macroscopic displacements of the whole film with a given elasticity tensor using Hooke's law.

The specimens were made out of special square-shaped samples (20x20 mm) produced by Bosch. Two different film thicknesses were used (2 and 4 μm) corresponding to 1 or 2 electrode layers. All samples were spin-coated with a polyimide solution (PI 2611 by HD Microsystems) and baked in an oven to eliminate the solvent. After that, a homogeneous polyimide film of approx. 10 μm thickness remained on the film. Polyimide is very soft and considered not to have a strong influence on the mechanical properties of the film.
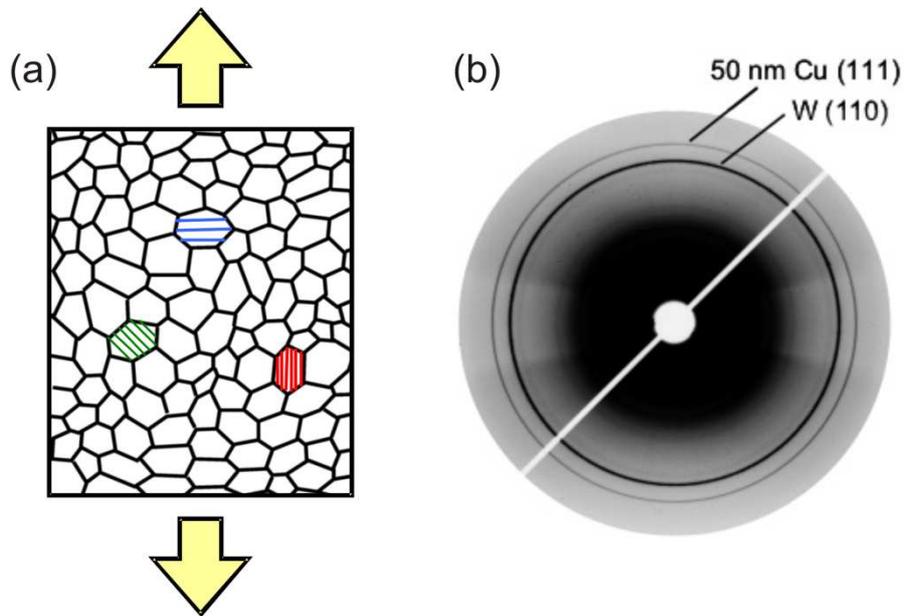
Figure 3.18: (a) Principle of the sin²ϕ -method. The in-plane lattice strains are measured. (b) Example of a CCD camera image of a thin copper film showing also the ring of the tungsten calibration substance.

The samples were cut into slices of 3x20 mm² with a wire saw. Different acids were tried to etch away the PZT, but it turned out that the only acid that etched PZT in a reasonable time (HF) also partly destroyed the electrode material. Reactive ion etching of the ceramic with SF_6 was too slow. It was found that the adhesion between the film and the substrate was not very good, so we were able to peel off the polyimide with the AgPd film attached. Finally, two polyimide foils with a thickness of 125 µm were glued on each side of the sample (figure 3.19) with a silver-epoxy-paste that was hardened on a heating plate.
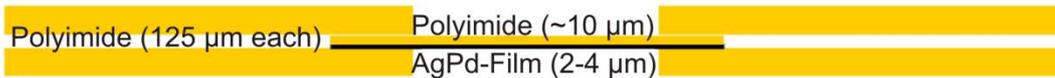
Figure 3.19: Sample preparation for micro-tensile testing: A polyimide film is deposited on the sample. After removing the substrate, two thicker polyimide foils are glued on each side.

The sample was mounted into a micro tensile testing machine that also offered the opportunity to heat. The CCD camera had to be moved close to the sample to be able to record the complete Debye-Scherrer rings. This was also the reason why a calibration substance was needed as the CCD camera position was not always at the same reproducible position. The tungsten powder was dispersed in a gel and stuck to the Kapton side of the sample. The macroscopic length change was measured by tracing two markers with a high resolution optical camera.

The experiments were performed at the surface diffraction beamline operated by the Max-Planck-Institute for Metals Research at the Angströmquelle Karlsruhe (ANKA)[114]. The photon energy was 7.97 keV. The micro-tensile tester was mounted on the goniometer. The exposure time for the CCD camera was 30 seconds, pictures were taken for each step of the tensile test. Figure 3.20 shows the experimental setup at the MPI-MF beamline at ANKA.
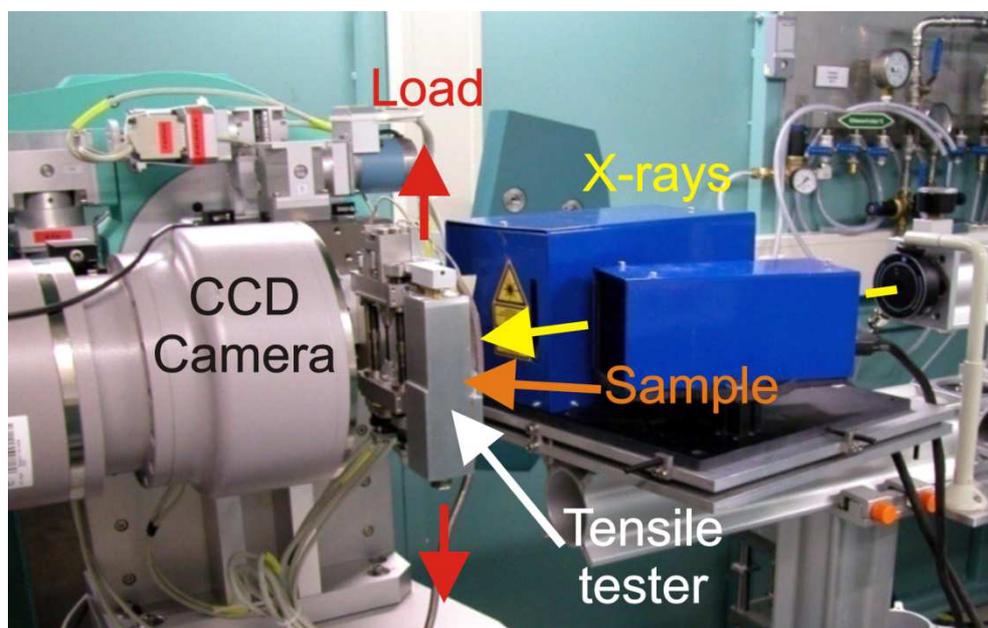
Figure 3.20: Setup for micro tensile testing at the MPI-MF beamline at ANKA Karlsruhe.

For most of the samples, the loading program was 7 steps with 9 µm step size followed by 23 steps with 18 µm step size each. Altogether the sample was elongated by 477 µm. The unloading program was 10x9 µm and 13x30 µm. At temperatures above 100 °C, the step size was 7x6 µm and 23x12 µm for the loading and 10x6 µm and 13x20 µm for the unloading part of the experiment. The testing temperatures were 20, 60, 100, 150 and 200 °C. For both film thicknesses, at least 2 samples were tested at each temperature. The nominal temperature was 10 °C higher than the temperature measured on the sample.

The CCD-frames were processed with a software package[122] written in IDL to extract the lattice strain. The stresses were calculated from Hooke's law using the values of the pure metals[124] and assuming isotropic behavior (no strong texture can be found in EBSD measurements in chapter 4.4) and a mixture rule for the Young's modulus E:

$$E_{alloy} = 0.7E_{Ag} + 0.3E_{Pd} = [(0.7 \cdot 82.7) + (0.3 \cdot 121)]GPa = 94.2GPa$$

The strain was calculated assuming equidistant steps. This simplification can be made if the strain of the film is proportional to the strain of the polyimide foil. To determine the residual stress, we took the stress plateaus of the loading and unloading curves and calculated the average value. Half of the distance between the plateau values was assumed to be the flow stress. A more detailed description of this can be found in chapter 5.2.

3.3.4 Electron Backscattering Diffraction (EBSD)

EBSD is a powerful method to monitor the orientation of grain and subgrain structures in a scanning electron microscope. It was discovered in the 1950s, but became widely used after 1992, when Dingley and Randall[125] developed automatic pattern collection and fitting routines. Reviews on this technique can be found e.g. by Huphreys[126] and Baba-Kishi[127]. In this work, EBSD was used to determine

the grain structure and to verify whether preferred orientations were present in the material before and after poling. To investigate our samples, we used polished PZT samples and investigated them in a LEO 1530 VP (see chapter 3.2.3) with an attached EBSD system (HKL channel 5.7). The voltage was 20 kV and the working distance 13 mm. Tango hkl software was used for automatic pattern interpretation. We also investigated AgPd films.

The pattern quality is highly dependent on the surface quality, so additional polishing steps were added. The sample surface is scanned with a stepwidth between 100 nm and 1 μm. An automatic mapping of a given region is done. The color coding of the standard orientation triangle allows determining the orientation at each point. Colored maps can be plotted to map the crystallite orientation in a certain spatial direction at every point. Usually, the pattern quality at some points is not high enough to determine the orientation. The indexing rate is a measure for the number of patterns that can be analyzed successfully. In our case, we achieved an indexing rate up to 90 %.

4 Results: Microstructural Investigations

4.1 Light Microscope

The light microscope pictures were mostly taken to get a rough idea of the multilayer actuator structure. Figure 4.1 gives an overview over the interdigitated layer structure of an actuator. The ceramic material can be seen in light blue. The high density of pores (dark spots) is mostly due to preparation artifacts. The internal electrodes are visible as dark blue lines. The red dots on the upper side of the actuator are the external electrodes made of copper which are connected to the actuators by a common Sn-based solder.
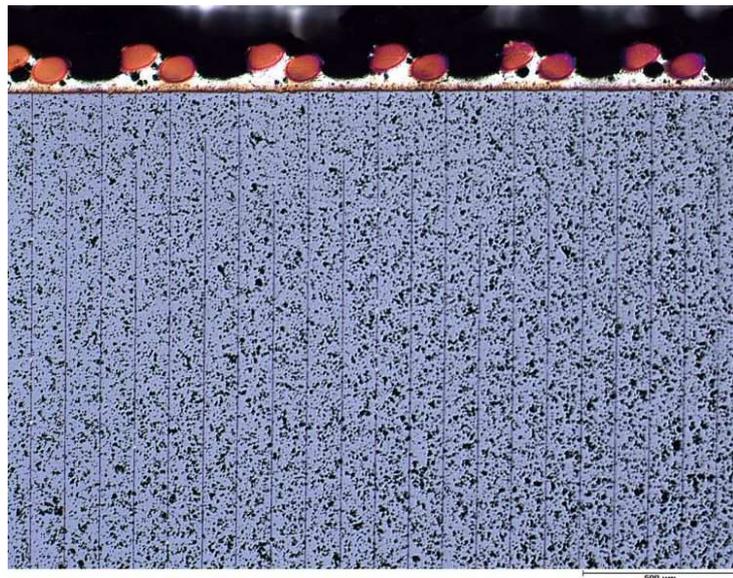
Figure 4.1: Overview of multilayer actuator taken in a light microscope with a magnification of 50x. The pores are preparation artifacts.

4.2 Focused Ion Beam (FIB)

The first investigations we performed with the focused ion beam microscope were overview pictures of the bulk actuator. In figure 4.2 and figure 4.3 two images with low magnification are shown. It is striking that the distances between the ends of the electrode material and the counter electrode vary strongly between 100 and 400 μm, which is due to the fabrication of the actuator when several hundred layers are stapled, a geometrically not very precise process, especially in proto-type production status. The grey shades around the electrode edges are due to charging effects of the non-conductive ceramic material. In figure 4.2, the external electrodes are still missing, so the actuator is investigated right after sintering.
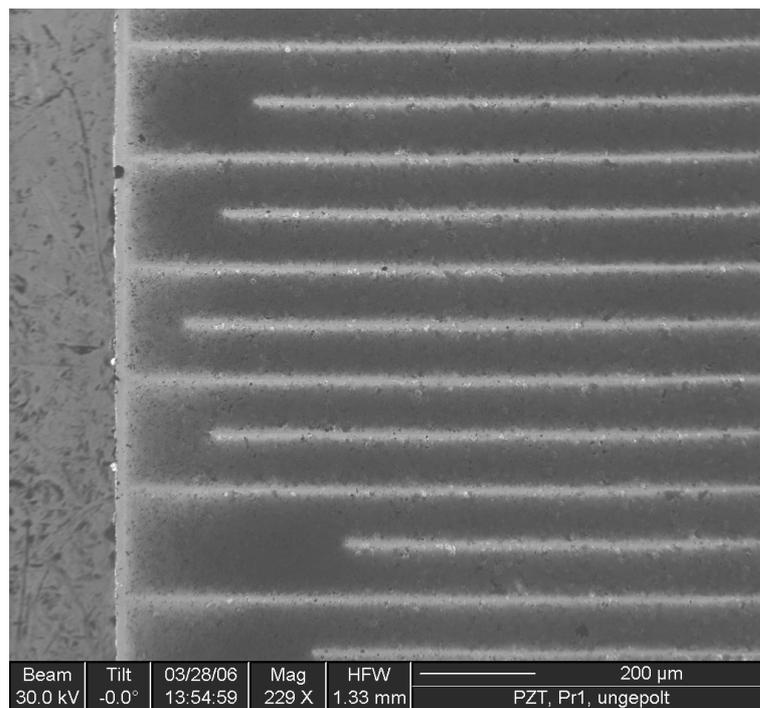
Figure 4.2: Overview picture of an actuator after fabrication, but still without external electrodes.

Beam	Tilt	03/28/06	Mag	HFW	200 µm
30.0 kV	-0.0°	15:04:33	239 X	1.27 mm	PZT, Pr2, gepolt (piezo)
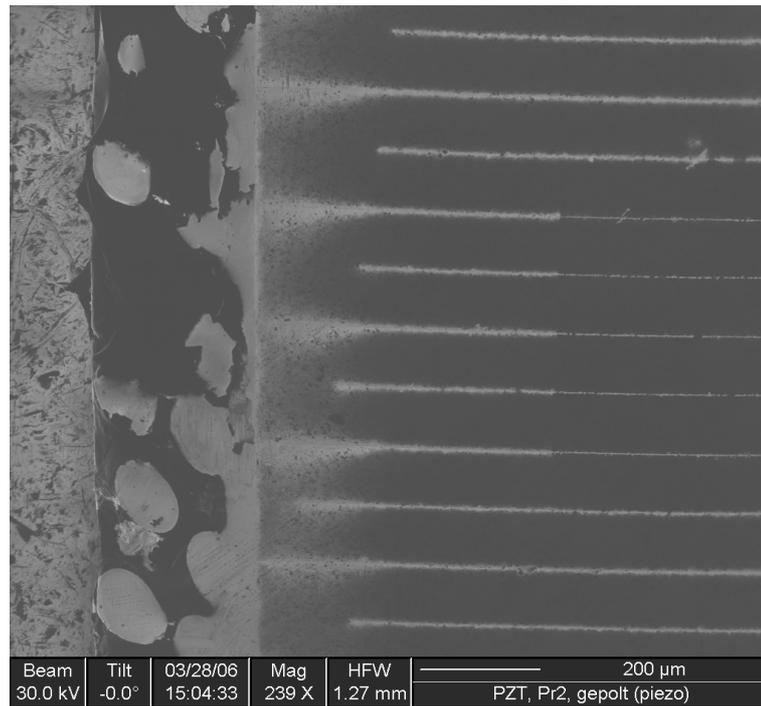
Figure 4.3: FIB picture of the actuator in pre-poled state with external electrodes, which can be seen on the left side of the picture as globular structures.

Furthermore, we took a closer look at the structure of the ceramic and the electrode material. Cross-sections were taken to get an insight view of the electrode structure because the soft electrode material may cause some smearing effects at the surface when grinding (figure 4.4). On the surface as well as within the cross-section the thickness of the electrode layer is not very homogeneous (figure 4.5). Some twin boundaries are visible and the grains are relatively coarse with grain sizes close to the film thickness (2 µm). Twins are boundaries where the stacking sequence of one side is the mirror image of the opposite side and are a well known structural feature in many metals. They can form during growth, recrystallization or deformation.
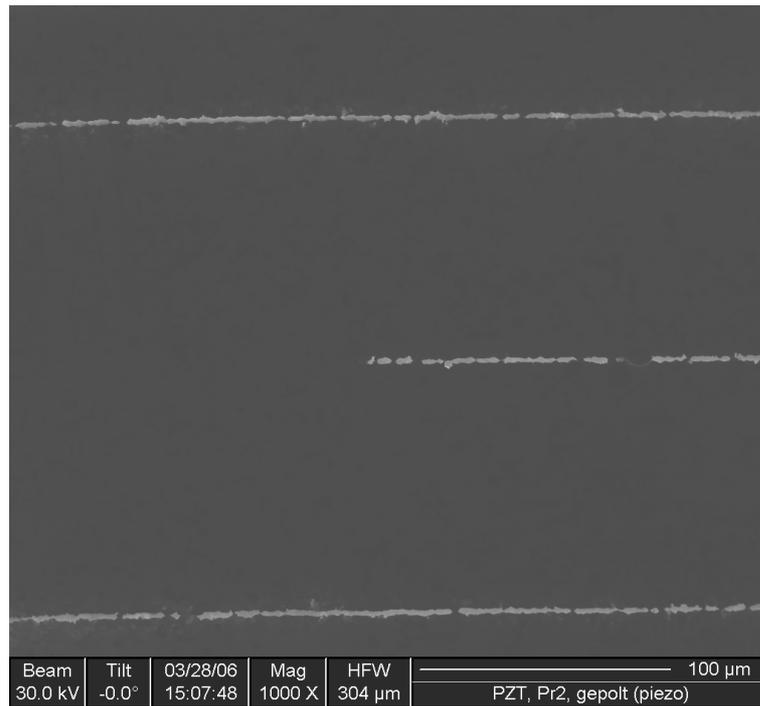
Figure 4.4: Overview of the actuator; the electrode material is smeared out at the surface.
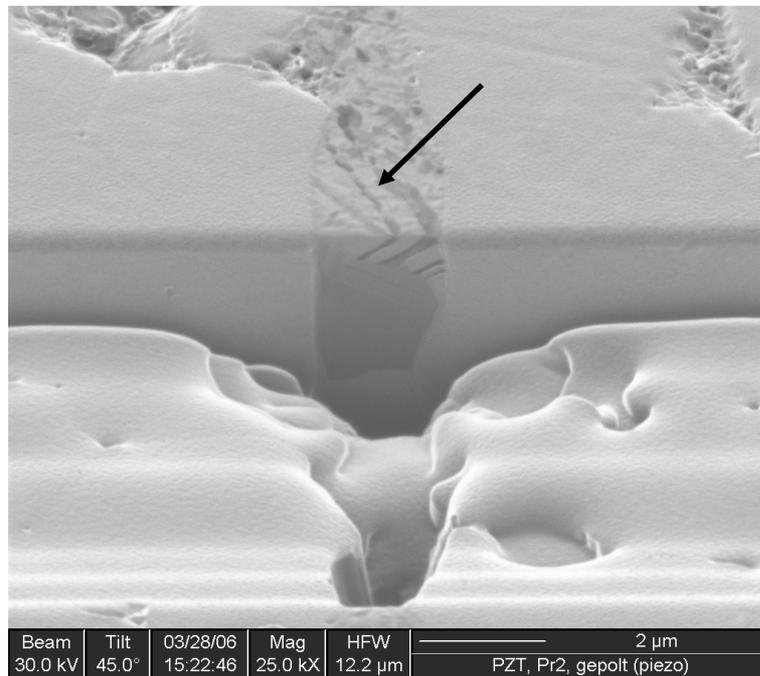
Figure 4.5: Cross-section image of an electrode. Twins (marked with arrow) and large grains are found.

Further experiments were performed on the samples for micro tensile testing (2 µm and 4 µm AgPd). The surface was very rough (figure 4.6) and many large hillocks were formed on the surface. The cross-section showed large grains again. To get a better view of the film and the interface the sample was polished and some more cross-sections were taken. The inhomogeneous film thickness was mostly due to surface roughness of the ceramic substrate leading to inhomogeneous ablation and some pores occurred at the electrode-ceramic interface (figure 4.7). A thin deformed surface layer formed during the polishing process.
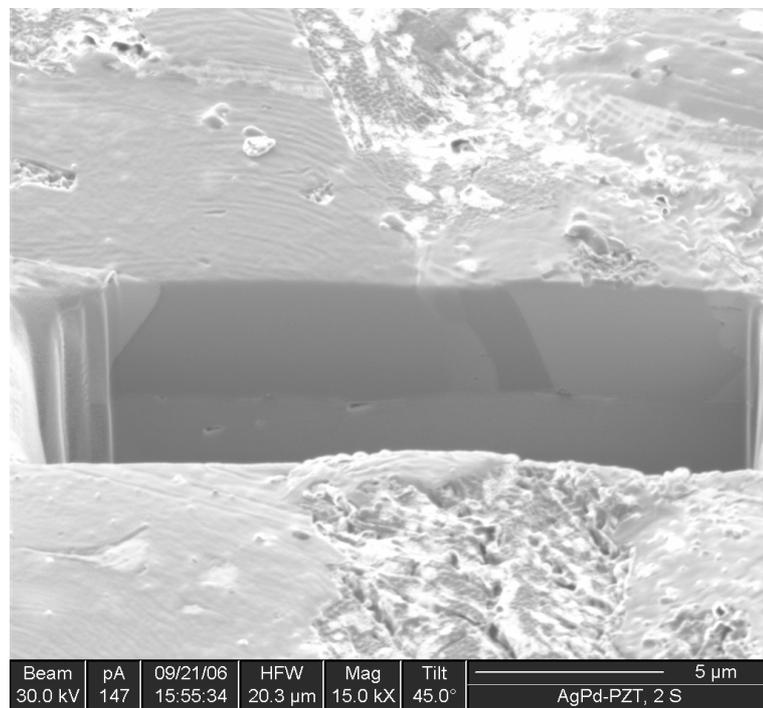
Figure 4.6: Surface image taken with the FIB. The unpolished surface is rough and hillocks are visible.
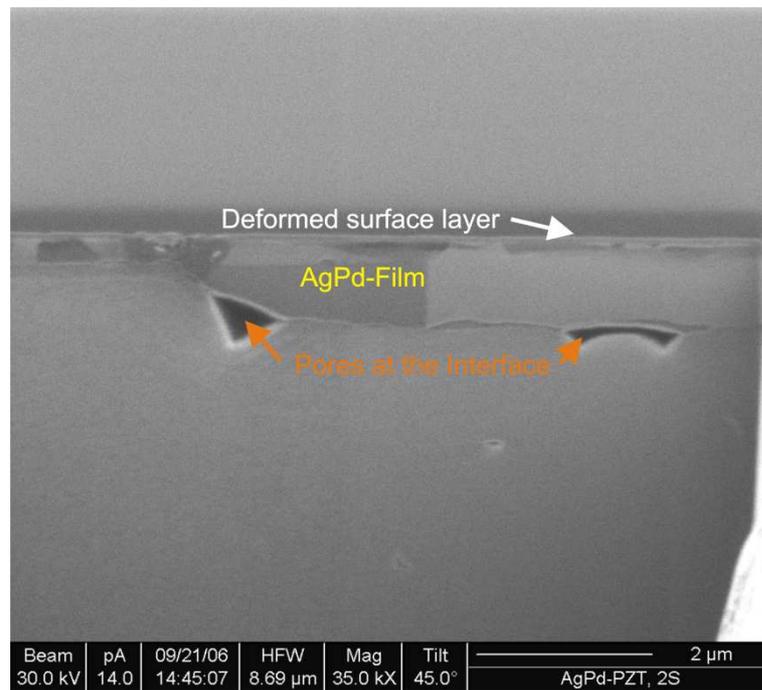
Figure 4.7: Surface picture of the FIB after polishing. A thin deformed layer on the surface is visible. The thickness of the film is inhomogeneous and pores on the interface are visible.

4.3 Scanning Electron Microscope (SEM)

The main use of the SEM was the imaging of grain and domain orientation of the ceramic by Electron Backscattering Diffraction (EBSD) measurements. In addition to the results observed with other microscopic methods, grains could be better distinguished using the RBSD detector (figure 4.8). With a higher magnification, the domain structure was partially resolved (figure 4.9), even though it was difficult to take really sharp images due to charging effects.

From the SEM Images one can see that the grain size was mostly in the regime of 1-5 μm, the domains were arranged in stripes of several hundred nm.
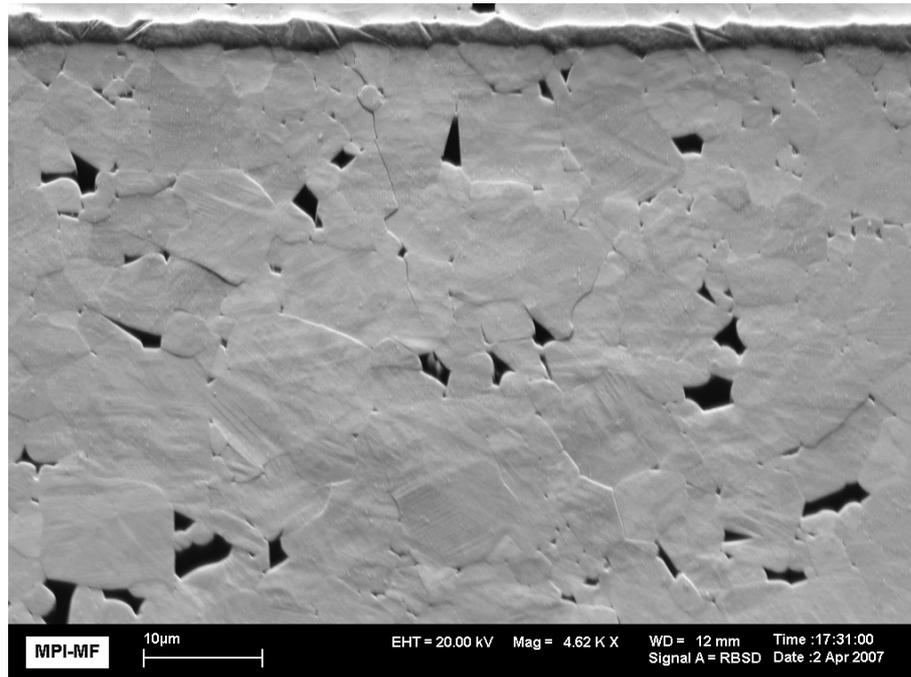
Figure 4.8: SEM overview image taken with the RBSD detector. Different grains can be resolved. Pores are due to preparation of the hard, brittle ceramic.
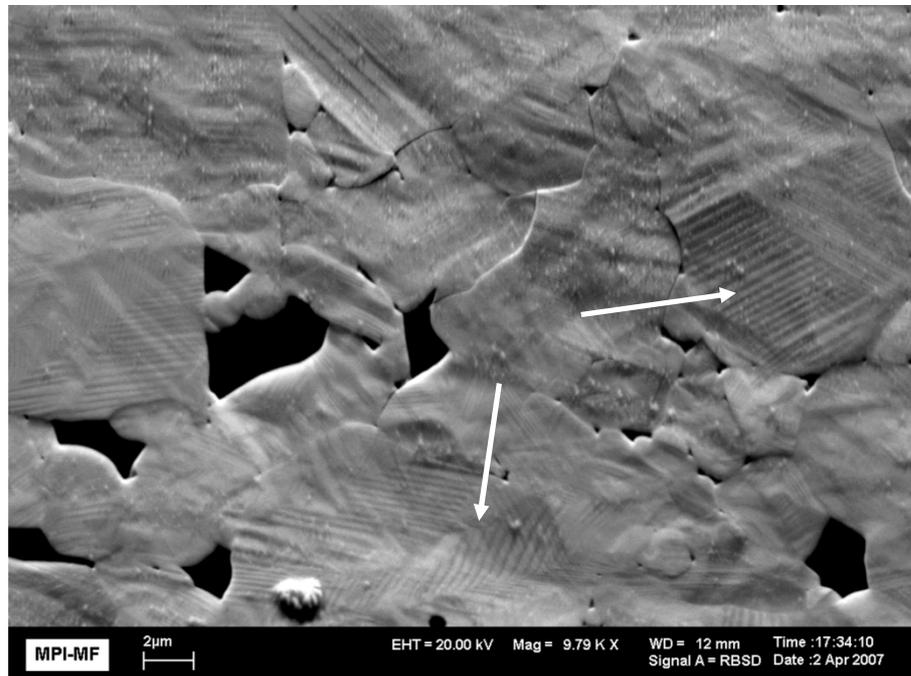
Figure 4.9: Detail picture in the SEM also showing domain structures (marked with arrows).

4.4   Electron Backscattering Diffraction (EBSD)

EBSD experiments were performed on the AgPd films as well as on the PZT ceramics. Figure 4.10 and figure 4.11 show two graphs of an AgPd film with the measured y- and z- orientation of the unit cell in the grains. In the upper centre grain, several twin boundaries can be found. The twins are oriented close to (001) and (210) direction, so the angle between these two orientations is almost 90°. In the lower grain, also a twin boundary can be assumed, but the indexing rate is lower, so no final conclusion can be drawn. The grain size is found to be relatively large (around 10 μm), which fits well to the results found in other microscopes.
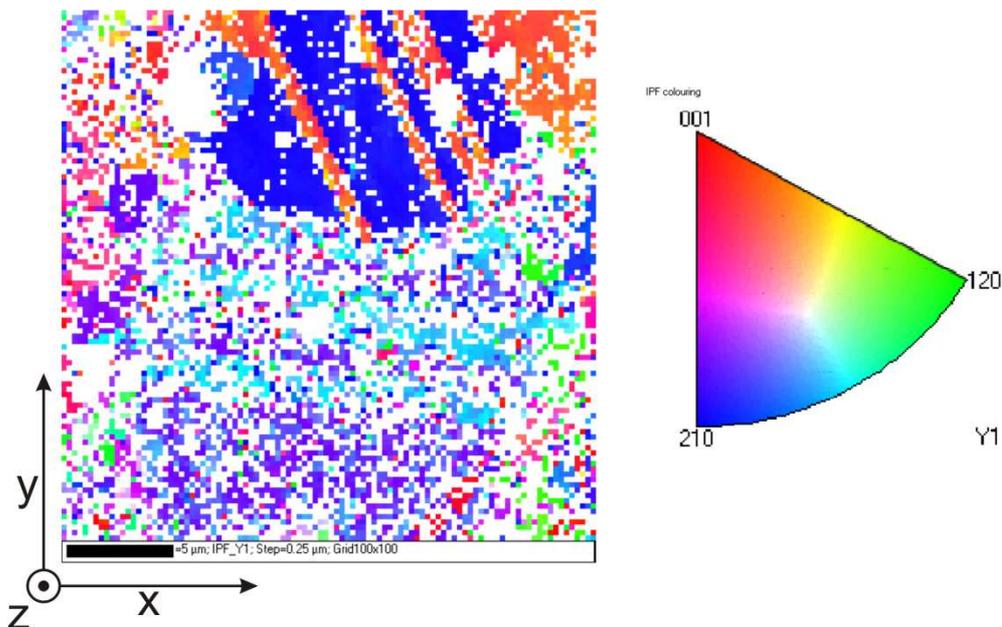
Figure 4.10: EBSD map of the orientation of an AgPd-film in y-direction. The color coding representing the unit cell orientation is shown in the right. To explain the directions used in all EBSD maps, the corresponding coordinate system is shown. In this case, for the micro-tensile sample, z is the potential direction of the electric field and the film expands in x- and y-direction.

74
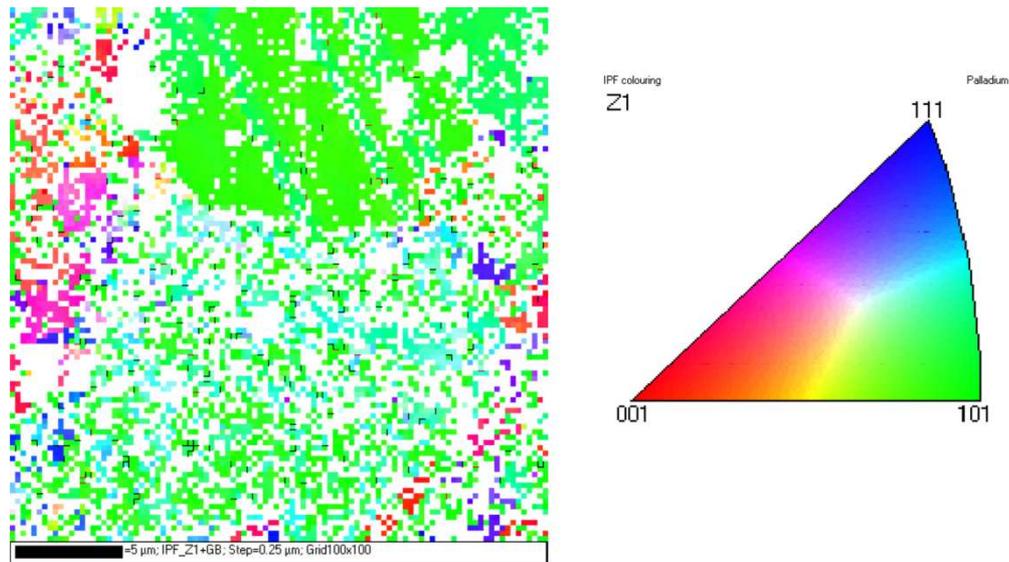
Figure 4.11: EBSD map of an AgPd-film in z direction.

In the ceramic, mapping was done at different sample positions. Goal of this study was first to resolve the grain structure of the material, second to see whether there is an orientation difference between the centre of the actuator and the inactive area close to the electrode edges. No clear trend could be seen at different sample positions, but in general it is remarkable that a relatively strong in-plane orientation in y-direction can be found (figure 4.12), while in z-direction the orientation is more or less random (figure 4.13). This is visible at all sample positions and thus probably due to a preferred orientation of the initial sheet material. Some single domains can be seen in EBSD experiments with higher magnification (not shown here), the grain sizes are mostly between 1 and 5 μm.
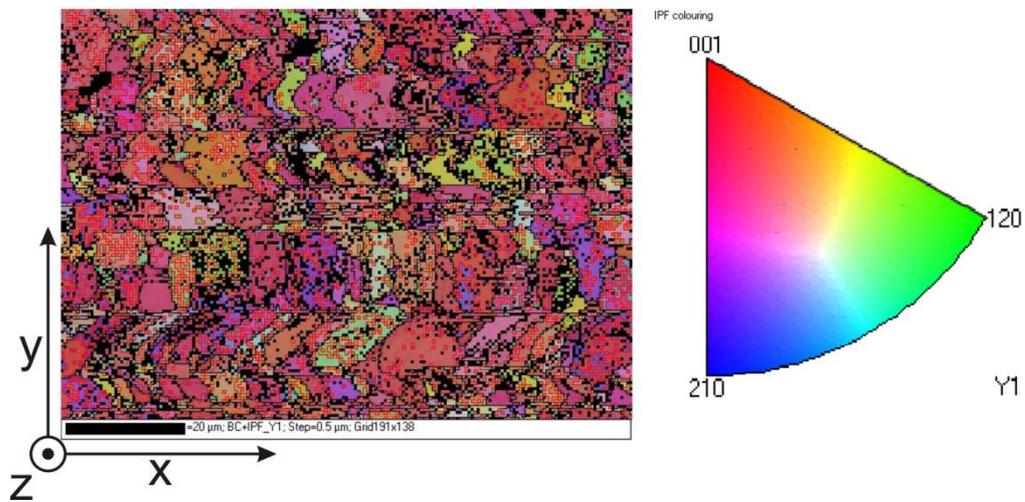
Figure 4.12: EBSD orientation image of the ceramic in y-direction. The grains are mostly (001) oriented. Y is the direction of the electrical field, x the direction of the electrodes.
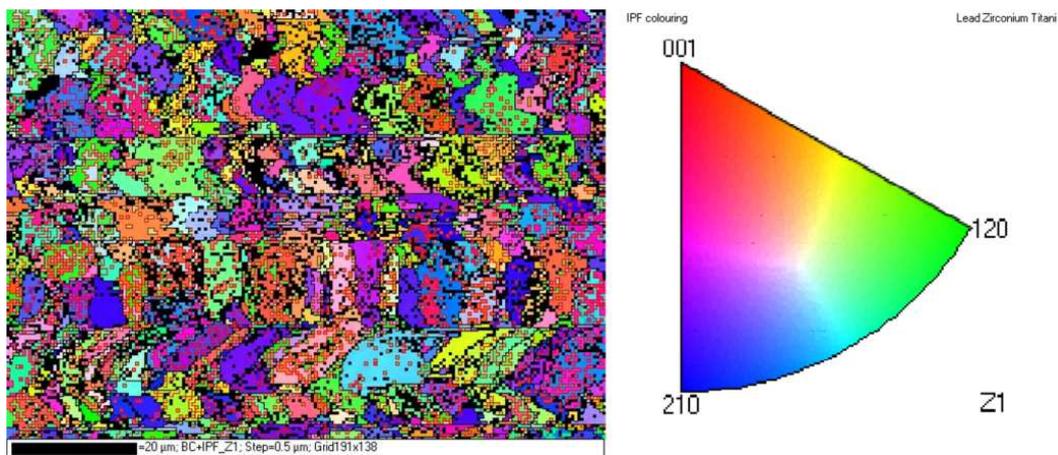
Figure 4.13: EBSD orientation image in z-direction. The grain orientation is random.

4.5 Discussion

The microstructure plays an important role when considering the properties of a material. In the case of a piezoelectric actuator, the whole material system that has

to be considered is complicated. Different constituents are involved, namely the internal electrode and the ceramic material. In addition, the involved geometries are complex.

The electrode is made of Ag70Pd30. Silver-Palladium is a system with a continuous solid solution between the two elements[128], so a homogeneous microstructure would be expected (figure 4.14).
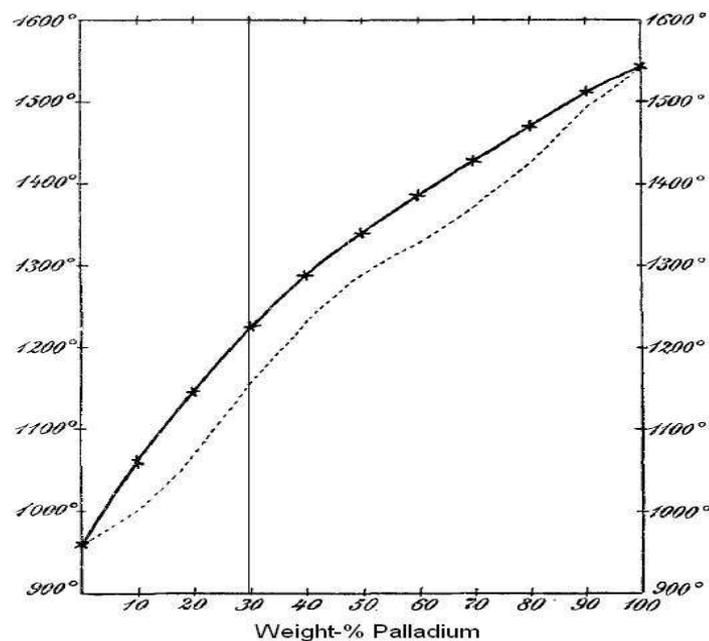
Figure 4.14: Phase diagram of the system Ag-Pd[128], the given concentration of our material (Ag70Pd30) is marked. The elements are fully miscible. The dotted line is the solidus, the continuous line the liquidus line.

The FIB cross-section pictures show twinning, a mechanism known to occur during recrystallization of fcc metals[129]. The temperatures to which the material was exposed during sintering (1000 °C) were relatively close to the melting temperature which lies around 1220 °C. At such high temperatures, recrystallization was definitely expected[130]. The large grains of usually several microns size can also be attributed to the growth of few grains during recrystallization when sintering the actuator. Normally, recrystallization also leads to a textured material, but in this

case no strong texture evolution was found. A study performed on AgPd films focusing on recrystallization could not be found in literature, so it is not clear how the microstructure of an AgPd alloy with this composition changes due to recrystallization. No significant difference was found between the films used for micro-tensile tests and the electrodes of the actuator.

Microstructural investigations of the actuator also revealed that the distances between the electrode edges and the counter electrode were inhomogeneous. The reason for that was the fabrication process, where all the layers of the actuator are stapled, laminated and then sintered[35]. The stapling in combination with the sintering process led to inhomogeneous distances and small shifts of all the PZT layers. The distances varied between approximately 100 and 500 µm. In addition to that, the FIB cross sections showed that the electrode thickness was also not constant. In fabrication, the electrodes were screen printed on the ceramic sheet material. As the sheet material thickness was already inhomogeneous and the screen printing is not a very precise process, thickness variations can be easily understood. When looking at the results of the micro-tensile tests, we have to keep in mind that the film thickness cannot be regarded as homogeneous. As the boundary layer between the film and the electrode shows some pores and did not appear to be very adhesive, we were able to pull off the films for the micro-tensile tests without destroying them.

The piezoelectric ceramic was made of $PbZr_{0.53}Ti_{0.47}O_3$, a composition where a potentially monoclinic structure would be expected. A small fraction of a different phase might nevertheless still be present (figure 4.15). This was not totally confirmed by synchrotron X-ray experiments (see chapter 6.2); our samples were mainly tetragonal, even though the question of a possible presence of a second phase could not be definitely answered. As the material was polycrystalline and not stress-free, it is very difficult to distinguish between intrinsic effects like residual stresses, which can also lead to changes in the peak shape, and a second

phase that may be present in the material. No clear information whether a possible second phase is rhombohedral or monoclinic could be found. To verify this, a different kind of sample, a powder with small grains and as stress-free as possible, would be necessary. When we consider expected phase compositions, we also have to keep in mind that other elements are present as dopants. This will shift the boundaries in the phase diagram.
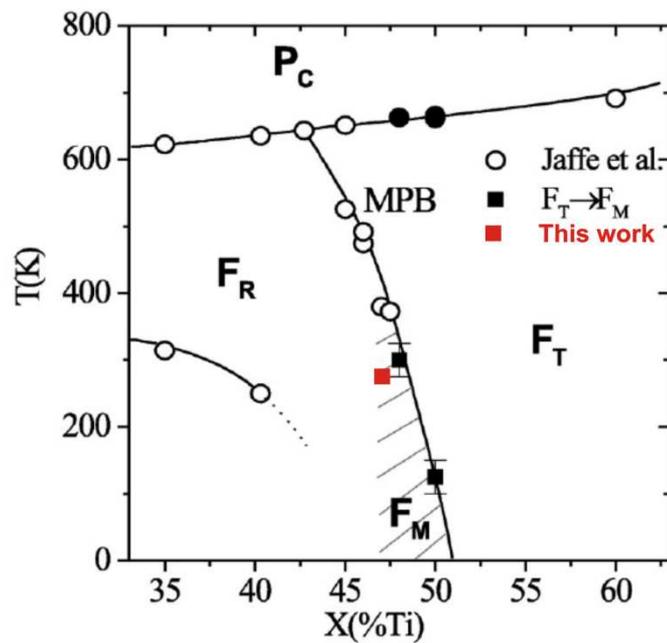
Figure 4.15: Phase diagram as suggested by Noheda et al.[22] A PZT ceramic with our composition is expected to occur potentially in the ferroelectric monoclinic phase (F_M), even though a small fraction of ferroelectric rhombohedral phase (F_R) might still be present in the material. From the pure composition, no ferroelectric triclinic phase[14] would be expected. The paraelectric cubic phase (P_C) only exists at higher temperatures.

By EBSD and SEM analysis, separate grains and in some of them even domains could be detected. Unfortunately, automatic grain size detection by the EBSD software was not possible due to the domain boundaries also present in the material. A manual grain size analysis showed grains in the range of 1-5 μm, smaller

grains are more frequent. Domains are arranged in stripes with distances of approx. 200 nm. The results fit well to other studies focusing on the domain configuration of PZT. A study of Schmidt et al.[131] done at PZT films of different thickness and composition showed similar domain sizes and shapes, a second work by Munoz-Saldana et al.[132] also confirmed this kind of configuration. Most of the domain boundaries that are visible seem to be 180° domain walls, but also some 90° domains can be found. In figure 4.16 (our work) and figure 4.17 (literature work) both configurations are marked.
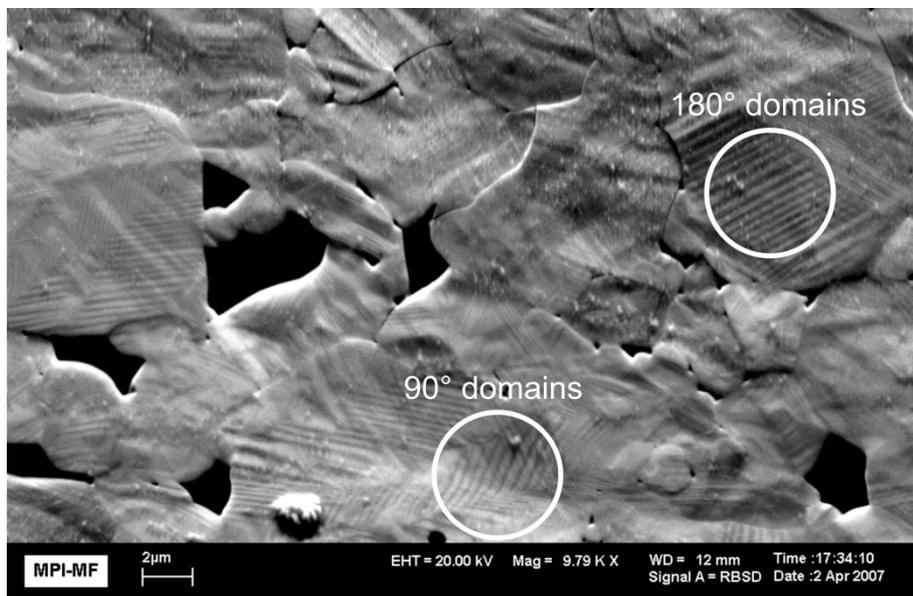
Figure 4.16: SEM picture showing the presence of 90° domains ("fishbone" structure indicating 90° angles) as well as 180° domains ("stripe" structure).
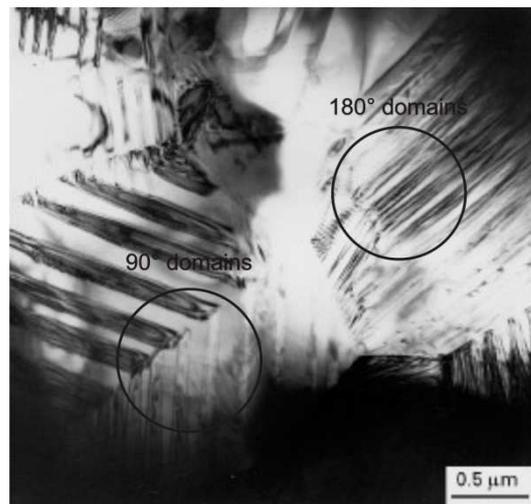
Figure 4.17: TEM picture taken from a work of Choi and Choi[133] also showing both types of domain configurations.

It is assumed that in general most switching in a piezoelectric material proceeds by 90° domain reorientation[25]. As these domains are present in the material, we can also expect this in our case. 180° domain switching is difficult to detect with our setup. In principle, the orientations can be distinguished using diffraction methods, but require studies with domain resolution. Also imaging methods like AFM or PFM can help, but are not used in this work.

A second thing that is revealed by the EBSD experiments is a relatively strong in-plane (001) orientation in y-direction (see figure 4.12). This would generally be expected after pre-polarization, because most of the domains should be oriented in poling direction. The general trend can nevertheless also be seen in the imhomo-geneous regions of the actuator, so we would rather expect an effect due to a pre-ferred orientation of the initial sheet material. For further details and to also get an insight into the domain structure, more EBSD measurements would have been necessary. In general, EBSD experiments showed that we can also measure single domains with this method; but also here more detailed investigations would have been necessary.

5 Results: Thin Film Experiments

5.1 Characterization of the metal electrode

Beside the first characterization of the films by FIB (chapter 4.2), X-ray experiments were performed to characterize the residual stresses in the films. The experiments were done by the central scientific facility X-ray diffraction using the $\sin^2\Psi$-method. Table 5.1 summarizes the results. Two specimens were investigated, one with 2 μm film thickness and the other with 4 μm film thickness.

Table 5.1: Residual stresses of AgPd films for both thicknesses, measured by X-ray diffraction.

Sample (AgPd thickness)	2 μm	4 μm
Residual Stress σ_R [MPa]	41 ± 5	61 ± 5
Lattice Parameter a_0 [Å]	4.000 ± .002	4.008 ± .002

A texture analysis of both films was also performed. Figure 5.1 shows the plots for the (111) peak. No significant texture could be found, the existence of many small peaks indicates a large grain size. The fact that the 4 μm sample had a stronger intensity drop already at lower tilting angles (figure 5.1 (b)) was only due to the smaller sample where edge effects occurred earlier.
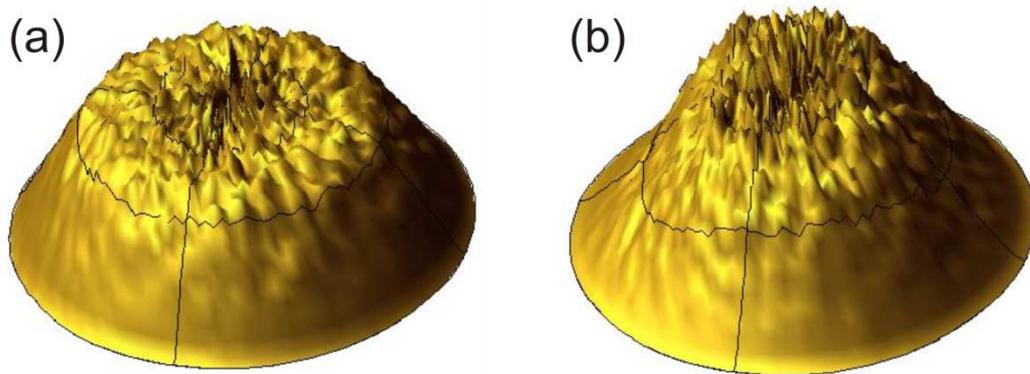
Figure 5.1: (a) (111) pole figure for the 2 µm AgPd sample. (b) (111) pole-figure for the 4 µm sample. No significant texture is visible. In both experiments, the sample was completely rotated (360°) and tilted by 90°.

5.2 Micro-tensile testing

For both types of samples (2 µm and 4 µm film thickness), micro-tensile tests were performed at ANKA. Starting from room temperature, the mechanical behavior of the samples at five temperatures between 20°C and 200 °C was studied. In figure 5.2, a typical stress-strain curve for an AgPd thin film is shown. The curve starts with an elastic slope marked in red. At a certain point, either plastic deformation starts or the films fracture in case they are brittle (figure 5.2). The maximum stress is reached at the end of the plastic regime and stress drops because of fracture. After loading is finished at almost 2 % strain, the unloading curve shows the same behavior, but fracture does not occur, as the test is now performed in compression. A larger plateau is visible.

From the curves, a maximum tensile stress σ_{max} and a maximum compression stress σ_{min} can be determined. Usually, one would expect that the absolute values of both stresses are equal. If this is not the case, one can assume that the sum of

both stresses represents an initial residual stress σ_i that is already present in the material at the beginning of the test.

$$\sigma_i = \frac{\sigma_{max} + \sigma_{min}}{2} \qquad (5.1)$$

To determine the flow stress of the films, the average of both maximum stresses has to be taken to eliminate the effect of the initial stress:

$$\sigma_{flow} = \frac{|\sigma_{max}| + |\sigma_{min}|}{2} \qquad (5.2)$$
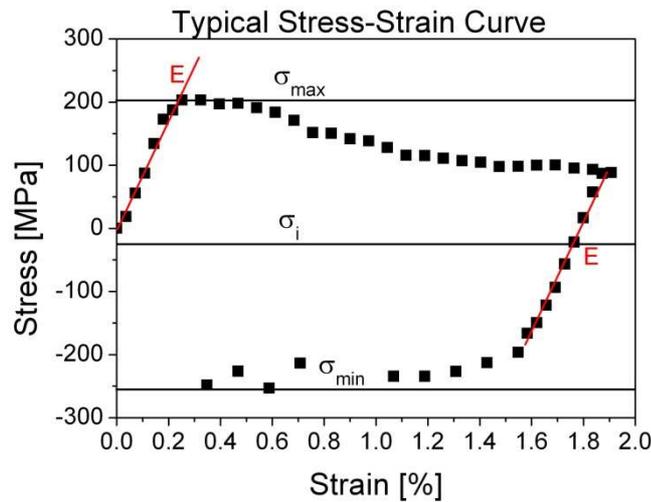
Figure 5.2: Example for a stress-strain curve of a micro-tensile test of a thin film sample. The maximum and minimum stress values ($\sigma_{max/min}$) are marked as well as the Young's modulus (E=Δσ/Δε=94.2 GPa) and the initial stress value (σ_i).

The stress-strain curves for all samples are summarized in figure 5.3. Curves for different samples are shown in different colors. The 2 μm samples show a high scatter and some of the films are porous, so only the 4 μm films are shown (and one example for 2 μm). For the 4 μm films, a general trend is visible. After an

elastic slope to strains of approx. 0.2 or 0.3 %, only a very small plastic regime can be seen, followed by stress drop.
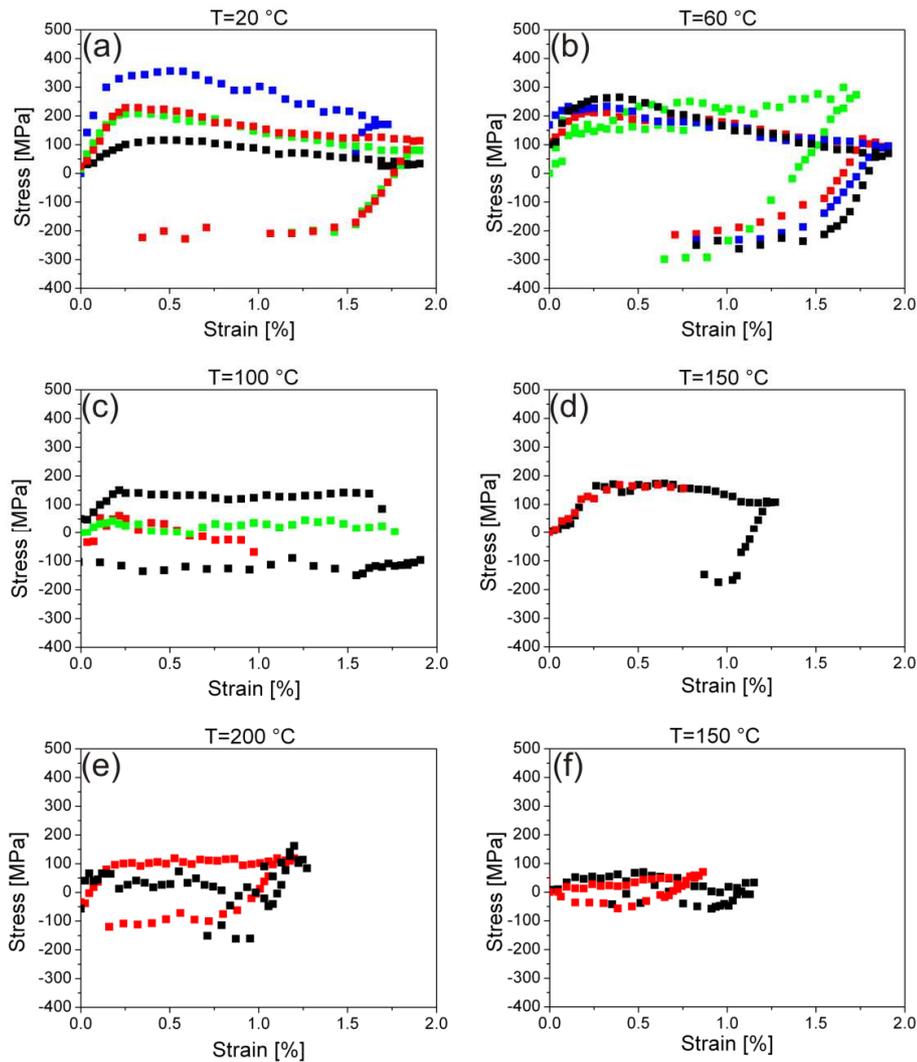
Figure 5.3: Stress-strain data of AgPd-films (a)-(e) 4 μm film thickness, T=20-200 °C. (f) 2 μm film thickness, T=150 °C. The different colors represent different samples tested at the same temperature.

From the micro-tensile tests, the flow stresses of the material could be determined. Figure 5.4 shows the flow stresses at 0.2 % strain for both film thicknesses plotted over the temperature. Even though the values scatter, a trend of decreasing flow stress with increasing temperature is visible.
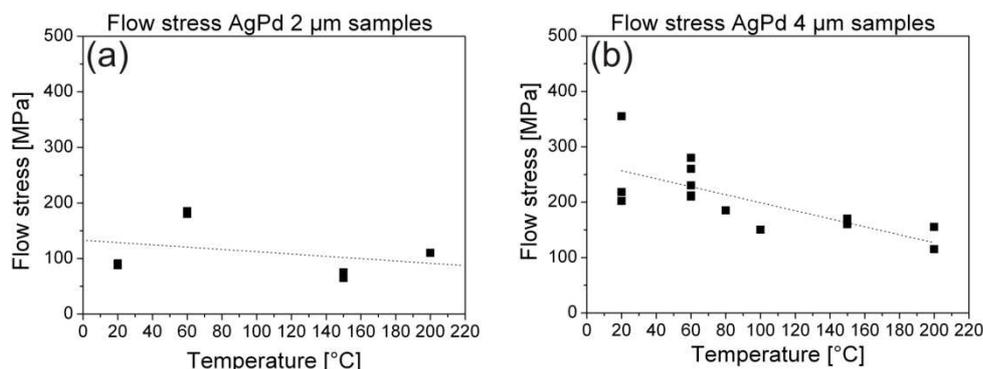
Figure 5.4: Flow stresses for both film thicknesses plotted against temperature (a) 2 μm, (b) 4 μm.

5.3 Discussion

Among other methods, micro-tensile tests play an important role in characterizing the mechanical properties of thin metal films. In our case, we used micro-tensile tests to study the temperature-dependent behavior of the AgPd electrode material. The films were printed on a PZT wafer and sintered with the same temperature program as the actuators to obtain a comparable microstructure. It turned out to be difficult to remove the films from the PZT substrate, especially all kinds of etching methods failed. The final method we used and which seems to be the only possibility was simply to peel of the polyimide film and the attached AgPd film from the substrate, which may induce some additional stresses in the film. On the other hand, this shows that we could assume a good adhesion between the film and the polyimide, so we think we can get reliable results from the micro-tensile tests.

A chemical or physical etching process might also change the stress state so we believe that our results are comparable to results obtained with an etched substrate. The initial stress state is also considered as the experimental results consist of both loading and unloading curve. From the shift of the flow stresses of both curves, the initial residual stress can be calculated. We obtained small tensile

stresses which fit reasonably well to the values determined by X-ray stress analysis with films that were still on the substrate. No strong influence of the peeling on the stress in the films is thus expected. The films are not textured, which can be explained by the printing process that does not favor a certain orientation. Anyhow, a texture would be expected from the recrystallization, as mentioned above.

If we look at the stress-strain curves, we can see that the stress drops at higher strains, which normally indicates fracture of the films. This effect does not occur during unloading where the film is compressed. If we compare the curves for the different temperatures, we can see that at higher temperatures, the plastic regime is larger and it is not obvious if fracture still occurs. The scatter of the data also increases at higher temperatures. For some of the films, either total fracture of the polyimide occurred or the glue dissolved. No unloading curve can be found in this case and the initial stress had to be assumed to be zero.

The general trend of the flow stresses is as expected, with increasing temperature the stresses decrease. Unfortunately the sample preparation especially for the 2 μm samples was difficult and often the glue spots were very small. Sometimes the bonding surface turned out not to be very stable, which was later solved by clamping the samples very close to the testing area. This may explain the high scatter at room temperature. Another problem is the fact that the unloading curves do not exist for all films, so sometimes we had to approximate the stress values only from the loading curve. In this case, the initial stress had to be assumed as zero.

Studying the mechanical behavior of thin films usually includes the study of size effects, as found e.g. in (ref.[134]). Thin films show higher strength due to the constrained geometry in one dimension. In our case, the thinner films show lower strength, so no conventional size effect can be seen, but the inhomogeneous thickness and the microstructure of the films determines the strength.

In operation, the actuator will undergo a length change of approx. 0.15 %. If we compare this with the curves we can conclude that only elastic deformation occurs in application as most of the samples have an elastic strain of approx. 0.25 %. FIB cross-section images showed that the film thickness of our samples is not homogeneous, so some thin areas of the film may be points of stress concentration and fracture will occur earlier here. Another result is that the plastic strain increases with higher temperatures. In figure 5.3 (e), the stress plateau is much more elaborated compared to the room temperature curves in 5.3 (a). This is not very surprising as dislocation movement is more reasonable at higher temperature, especially in the constrained geometry of a thin film. It should be mentioned that the residual stresses in the films after sintering is low, so we would not expect a huge problem during operation where much smaller temperature differences occur. On the other hand, the flow stresses of the films especially at elevated temperatures are also not very high (around 160 MPa for 150 °C) so still it cannot be excluded that residual stresses may cause problems at the interface.

6 Results: Static Diffraction Experiments on Piezoelectric Actuators

6.1 Pre-characterization by Conventional Diffraction

The goal of conventional X-ray diffraction experiments was to characterize the material and do pre-tests for the synchrotron experiments. A texture analysis of the sample was performed, but no significant texture was found as well as no huge difference in orientation between an unpoled and a poled sample.

6.2 Synchrotron Experiments

Some non-time-resolved measurements were performed at synchrotron sources to characterize the sample. First scans were θ-2θ scans, one of these scans can be found in figure 6.1. Splitting of some of the peaks can be found indicating a tetragonal or rhombohedral distortion of the sample.

From the θ-2θ scans we extracted the lattice parameters of PZT using Bragg's law (formula 3.1 and 3.2). Even though the peak positions did not yield exactly the same lattice parameters values for each Bragg peak, probably due to the stress state of the grains, the rough lattice parameters could be determined as:

a=b=4.03±0.03 Å, c=4.13±0.03 Å.

Thus, the tetragonal distortion of the unit cell is around 0.25±0.15%.
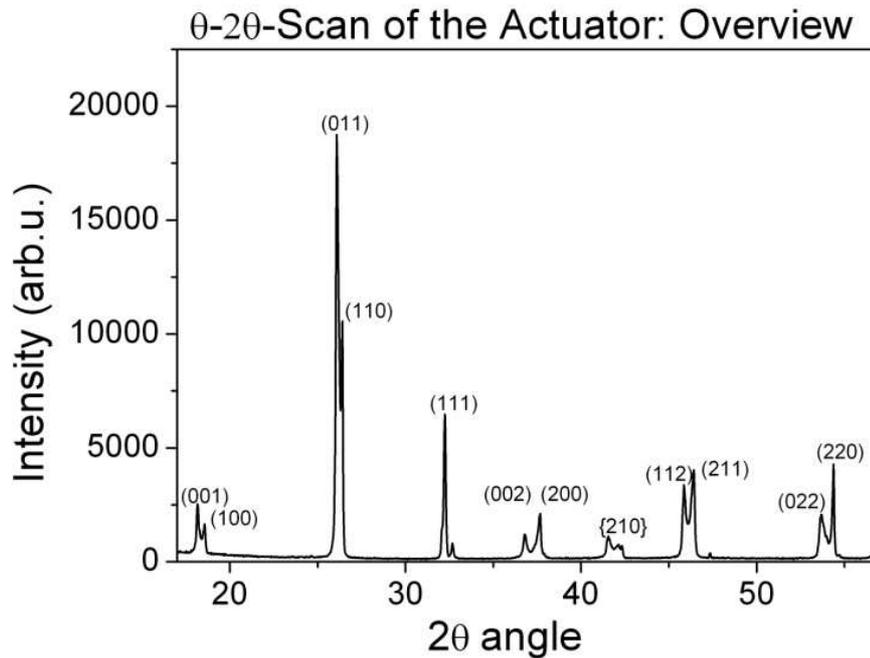
Figure 6.1: θ-2θ-scan of the PZT actuator performed at ANKA.

For some of the peaks, not only the expected splitting due to the tetragonal distortion, but an additional peak splitting was found indicating a two-phase material. As an example, figure 6.2 shows the (111) peak fitted with two Gaussian peak functions. For a purely tetragonal material, no splitting of the (111) peak would be expected. The second peak at lower angles might indicate a fraction of rhombohedral or monoclinic phase.
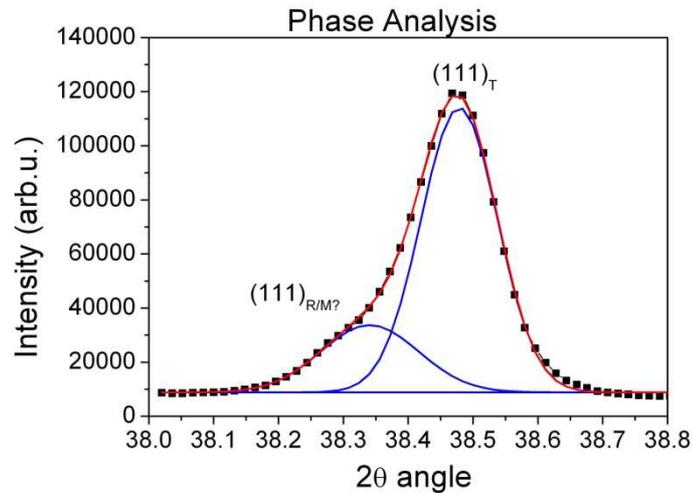
Figure 6.2: (111) peak of the actuator at room temperature. The peak can be fitted best using two Gaussian functions. For the tetragonal phase, no peak splitting would be expected, so the presence of a second peak could indicate a possible second phase.

Rocking scans at the (101) peak were performed to search for groups of grains with highest possible intensities. A typical example for a rocking scan can be found in figure 6.3. Some smooth and relatively broad peaks can be seen over a high background. These peaks may represent single grains or groups of grains with similar orientation.
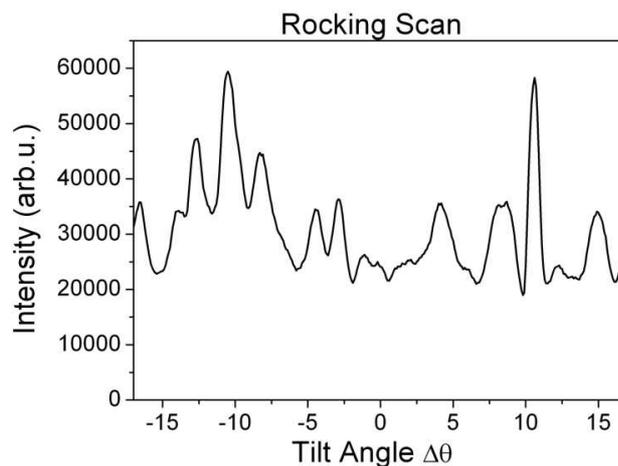
Figure 6.3: Rocking scan of the (101) peak of the actuator as performed at ANKA. Peaks indicate groups of grains with similar orientation, but the background is relatively high compared to the ESRF measurements.

At ESRF, we did not select the grains more or less randomly but used an x-y-stage to choose special sample positions we were interested in. To position the sample, the (111) peak of AgPd was centered and the sample position in the beam was scanned perpendicular to the electrode direction. The electrode positions were well visible as peaks (figure 6.4). The distance between those peaks is 90-100 μm, which corresponds to the electrode distance. The inactive area was found when the distance changed to approx. 200 μm, as now the counter electrodes were not illuminated by the beam anymore.
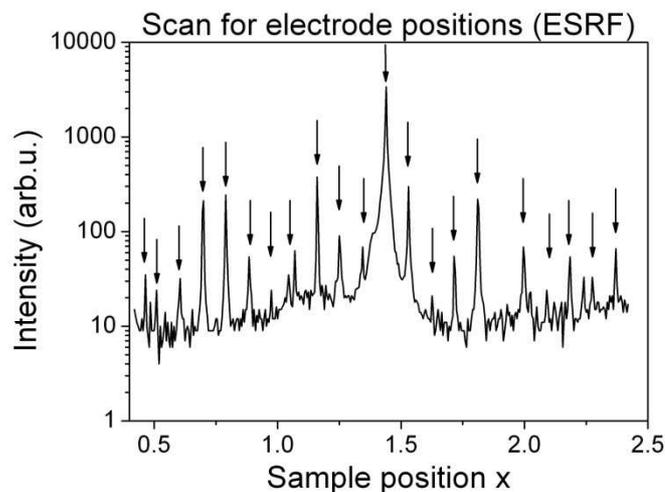
Figure 6.4: Scan of the sample to check for electrode positions (marked with arrows). The distance between the electrode peaks is around 90-100 μm, as expected.

Due to the small beam spot, the rocking scans of the ceramic material looked completely different at ESRF (figure 6.5). Only very few pronounced peaks were found which could finally be centered. Peak intensities were often close to 10^6 counts per second.
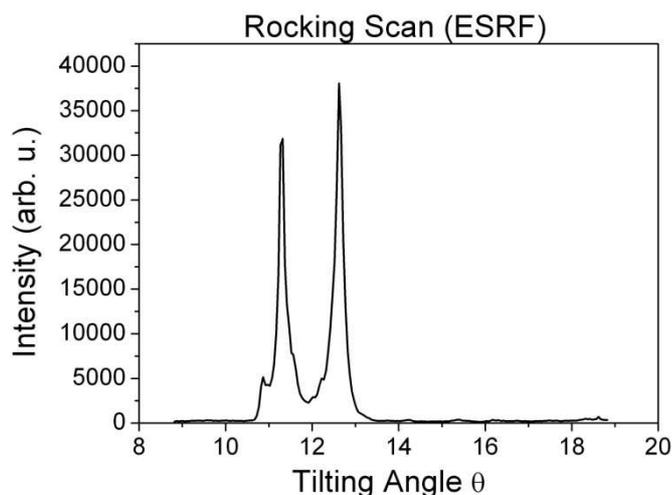
Figure 6.5: Rocking scan of the ceramic (101) peak at ESRF. Due to the small beam spot, only few grains are illuminated among which some single ones obey Bragg's Law. The background from other grains is almost zero.

When using the baby actuator at ANKA and ESRF, the basic setup remained the same. The only difference was that it was more difficult to locate the electrode material at ESRF because the top electrode was thinned and less grains of AgPd were in diffraction condition.

6.3 Discussion

Some experiments with a static external electrical field applied to the actuator were done at ANKA to study the voltage-dependent change of the lattice parameter. Voltages between 0 and 200 V were chosen (figure 6.6 (a)). At first, it appeared to be surprising that the lattice plane distance was decreasing with increasing field strength. This could be explained by the geometry of our experiments. To verify this hypothesis, the sample was tilted by 70° and the experiment was repeated. Now the shift occurred in the expected direction (figure 6.6 (b)).
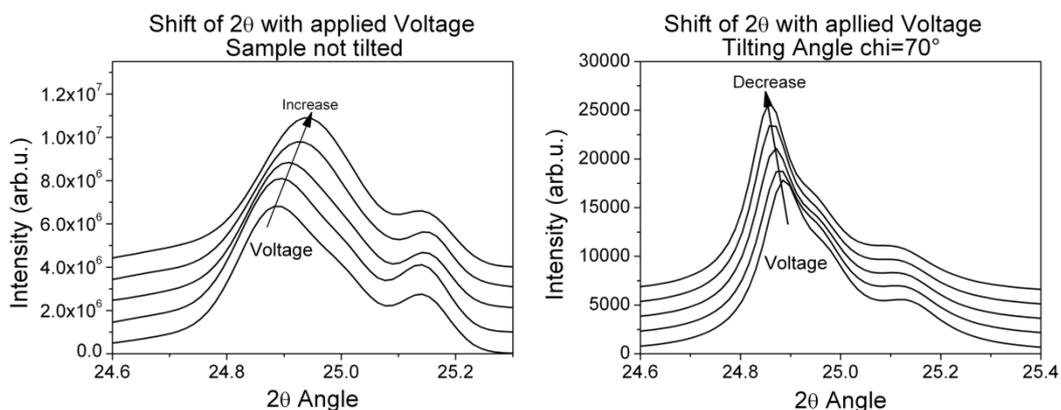
Figure 6.6: Shift of 2θ angle when applying voltages between 0 and 200 V to the sample. (a) First, the lattice plane distance decreases with increasing voltage. (b) When the sample is tilted, the angle decreases and the expected expansion is visible.

From static X-ray experiments, we can get some information on the crystal structure of the actuator material. As mentioned above, we would possibly expect the PZT to be monoclinic. Looking at a θ-2θ-scan, we can see that the peaks split in a way, which we would expect from a tetragonal ceramic, even though some small fractions of a different second phase, rhombohedral or monoclinic, might still be present (see figure 6.2). The dopants present in the material seem to shift the phase composition to the tetragonal phase.

By performing rocking scans and translating the sample perpendicular to the beam directions, we could select some grains or groups of grains with the highest possible intensity and then centre on the peak. The dependence of the peak position on the applied voltage is plotted in figure 6.7. Several different interesting effects can be seen.
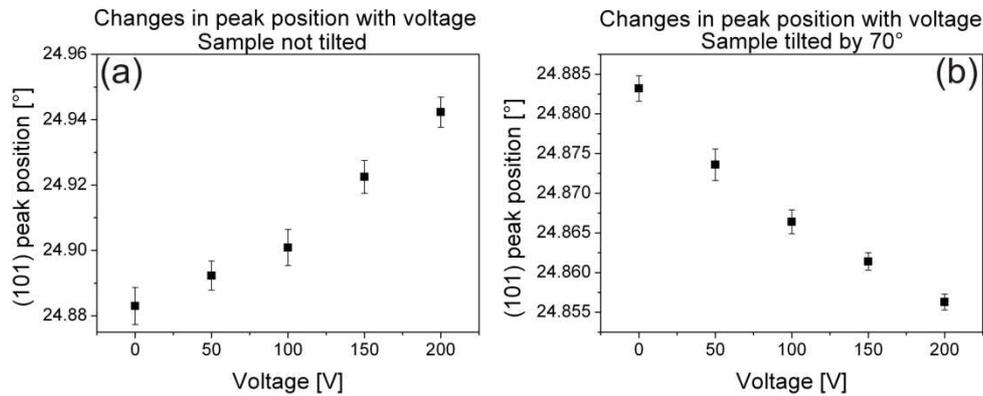
Figure 6.7: (101) peak position as a function of voltage. (a) Lattice plane direction perpendicular to expansion direction. (b) Lattice plane direction tilted by 70° into the direction of expansion. Error bars are as given by the fitting routine in origin.

In general, we would expect an expansion of the (101) planes when applying a voltage. We can do a simple calculation to verify that: If Poisson's ratio is 0.3 (ref [135]), the elongation of the c-axis would be more than three times as high as the contraction of the a-axis. In our case, the expected shift of the lattice plane distance would be 0.14%. With this data, the peak position at 200V should shift from 24.884° to 24.849°.

Of course, this would only be the case if the c-axis is oriented fully in the direction of the electrical field. Also, the calculation mentioned above is strictly only valid for a single grain with the c-axis oriented parallel to the direction of the field. In a polycrystalline material, there might also be collective effects of the whole sample that influence the response of the single grains. Surrounding grains can also affect the behavior of the grains we are investigating in the experiment. As a whole, the actuator will expand in the field direction and contract in both other directions. If we consider the untilted sample, the planes we are investigating are oriented in a direction of lateral contraction, so it is not surprising that we effectively measure a contraction.

Also, we do not know the full orientations of the grains we are investigating. In our setup, we do not know the precise orientation perpendicular to the diffraction vector. We only know that in the unit cells we are investigating, the (101) planes are oriented parallel to the surface, there is still an unlimited number of possible orientations of the a- and c- axis. In addition to that, we are dealing with a polycrystalline material. After tilting, lattice planes mainly located in the direction of expansion should be in Bragg condition (figure 6.8). This is indeed confirmed by the results seen in figure 6.7 (b).
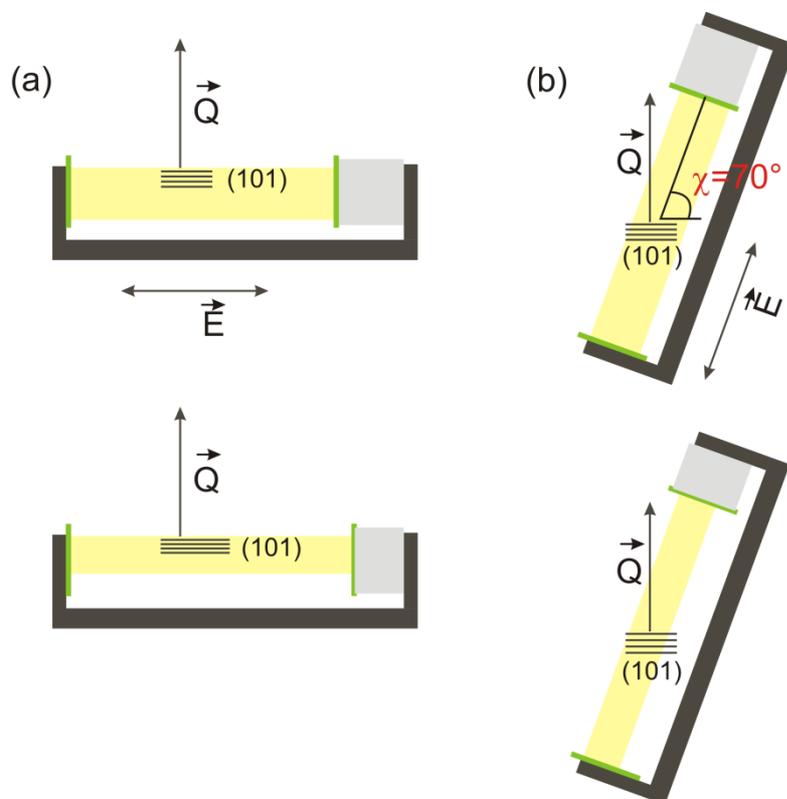
Figure 6.8: Schematic view of the sample first not tilted and then tilted. The beam direction is from the eye of the viewer into the paper plane. In (a), the actuator contracts in the direction perpendicular to the electrical field and thus forces the (101) lattice planes of the grain also to contract. When tilting the sample, the direction of expansion of the actuator is close to the direction of the (101) lattice planes and thus the X-ray experiments show an expansion (b).

Another interesting effect that can be seen in the graphs is that the relation between voltage and peak shift is linear up to 100 V, but after that a deviation from this linear relation can be seen. We do not expect domain wall movement to start so late as the ceramic is a very soft piezoelectric[136]. The strange thing is that in both cases the deviation is in positive direction, so for the tilted sample the total shift is smaller than expected (figure 6.7 (a)) and in case of the sample surface perpendicular to the lattice plane orientation it is larger. The effect can thus be only explained by a movement of the sample as a whole perpendicular to its long axis, so this appears as positive shift.

7 Results: Time-resolved Diffraction Experiments on Piezoelectric Actuators

7.1 First results

Different kinds of time-resolved experiments were done both at ANKA and ESRF. At first pre-experiments at ANKA, the full actuator was studied. The sample position and all angles were kept constant and only the change of the peak intensity with time was recorded. After that, rocking scans in both θ and φ direction (figure 3.6) were performed. At each point of the scan, the time-resolved intensity changes were recorded. From this, potential peak shifts with time could be extracted. The results of the small and split actuator are of better quality, so most of the results for the full actuator will not be shown here.

As an example for the experiments with the full actuator, the time-dependent intensity of one single Q point of the (101) peak is shown in figure 7.1. In this case, the voltage was switched on after 2 ms and switched off after 7 ms. 500000 cycles were accumulated resulting in a high signal to noise ratio of the intensity curve. The visible vibrations could be addressed to eigenmodes of the sample frame by doing a frequency analysis with finite element methods (work was done by Dr. Frank Felten, Robert Bosch GmbH). Different excitation frequencies were scanned and the sample response was investigated, and at the frequencies found in the time-dependent intensities curve, strong vibrations of the sample frame were found.

The intensity at the Q point measured in figure 7.1 changes when applying an external field. Possible reasons for this could be a peak shift in any possible direc-

tion, domain switching processes which change the intensity relations between peaks or changes in strain. A detailed discussion on this will follow later.
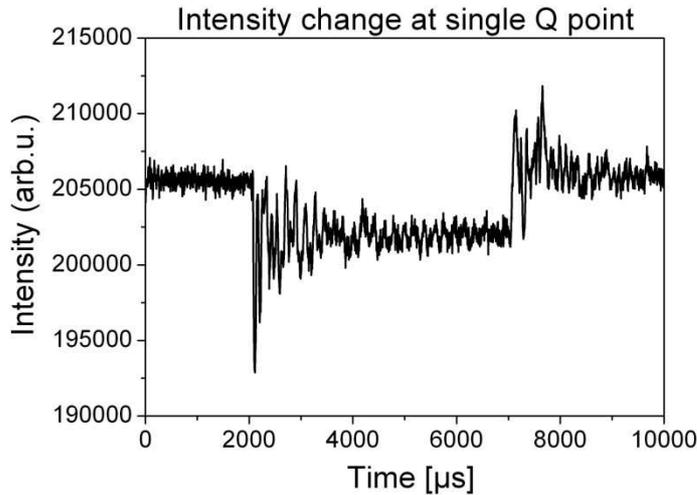
Figure 7.1: Change of the intensity of one single Q point for the full actuator after applying an external electrical field. The intensity changes when switching on the field, but strong vibrations of the sample environment mask possible relaxation effects.

It is not sufficient to consider only the change of a single point in reciprocal lattice. An intensity change can be caused by a peak shift in any direction or also only a change in peak shape, so we will consider the full changes of a Bragg peak when applying an electrical field. For this, we mostly recorded meshes in θ and θ-2θ direction. Other directions exist in which the peak could shift, such as the translational directions x and y (which should not play a big role at ANKA when working with a large beam spot compared to the grain size) and the second tilting angle χ. In χ, the peaks were relatively broad and we were thus not sensitive to small shifts in this direction. The same holds for the in-plane rotation angle φ.

Although no relaxations of the intensity after switching were found in these first experiments, we could already measure peak shifts both in θ and θ-2θ direction. The results were later reproduced with the small actuator when measuring a full

mesh of the peak (see chapter 7.2 and later). Figure 7.2 shows the peak shifts with an applied electrical field. Only the average values with and without electrical field were considered, potential vibrations or relaxations were not taken into account at this point.

In both directions, the peak shows a shift when applying an electrical field, which at first is not surprising. The elongation of the c-axis combined with a contraction of the a- and b-axis trivially leads to a tilting of (101) planes in the unit cell (see figure 3.10). Again, we see a decrease of the lattice plane distance, which has been discussed in chapter 6.3.
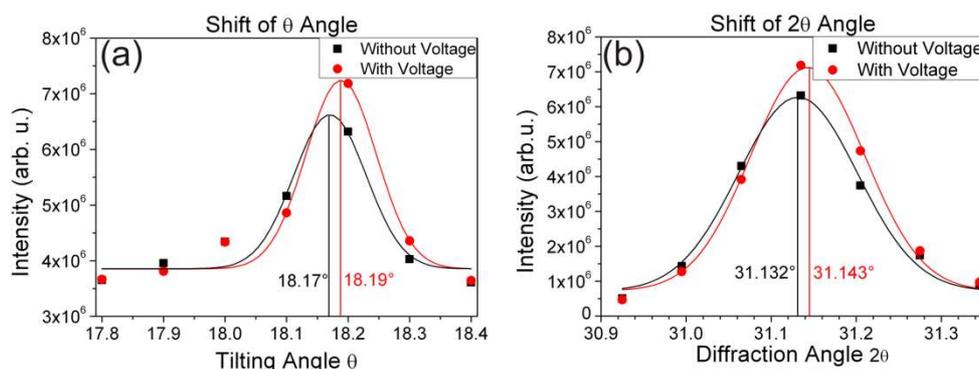
Figure 7.2: "Static" shift of the (a) θ and (b) 2θ angle when applying an electrical field to the actuator, measured in early ANKA experiments.

In the next step, the new sample chamber with the small actuator was used and the sample was operating against a spiral spring. A full mesh was recorded; the vibrations especially in the θ direction were much stronger than before (figure 7.3). The reason for this is that the spiral spring shows periodic vibrational rotations. Relaxations could still not be seen. After this experiment, only the split actuator was used for further investigations and the spiral spring was replaced by a bulk steel block.
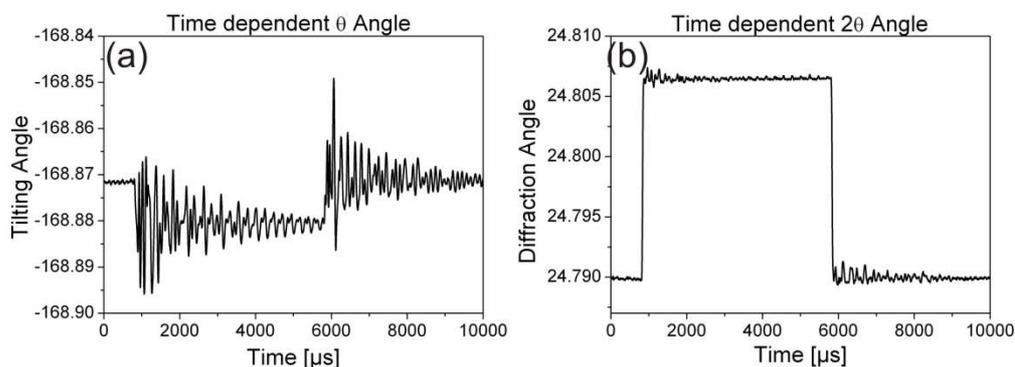
Figure 7.3: Time-dependent change of (a) θ and (b) 2θ angle of the (101) peak position when using the small actuator with a spiral spring. Very strong vibrations can be seen, especially in θ direction.

7.2 Results at ANKA with the split actuator

The first mesh with the new split actuator setup (see figure 3.11) showed much less vibrations, and now a small relaxation after switching the electrical field was visible (figure 7.4 and figure 7.5). This region could be fitted by an exponential decay function with time constants in the regime of 100-250 μs (figure 7.5). This relaxation can later be found at almost every time-resolved experiment with the split actuator, a detailed discussion will follow in chapter 7.6.
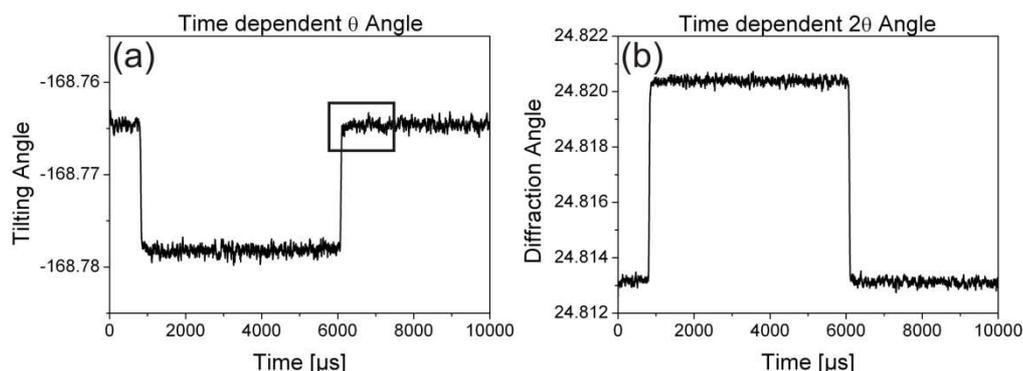
Figure 7.4: Fit of the angle positions of (a) θ and (b) 2θ measured with the split actuator setup on the (101) peak. Vibrations are reduced by approximately an order of magnitude. After applying the electrical field, a small relaxation of the angular position can be seen. One of these relaxations is marked in (a).
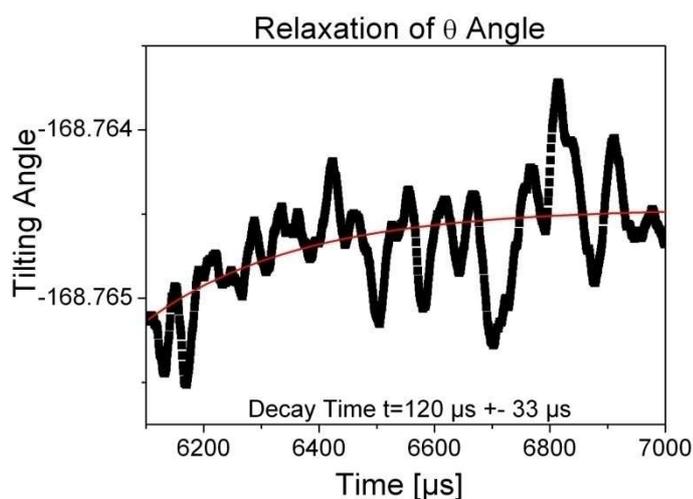
Figure 7.5: Fit of the relaxation of θ marked in figure 7.4 (a) with an exponential decay function. The decay time is in the same range as the other relaxation times obtained from figure 7.4.

In the next experiment performed at ANKA we investigated the influence of different parameters on the changes in peak positions. We started with a first mesh at room temperature and with the standard parameters (U=160 V, ΔU/Δt=5 V/μs, T=RT, (101) peak). The previously observed behavior was confirmed. The next experiment was performed at the (111) peak to study the response of a different

105

type of lattice planes. The time-dependent peak positions can be seen in Figure 7.6, relaxations after switching the voltage on and off could be fitted with times around 100-200 µs.
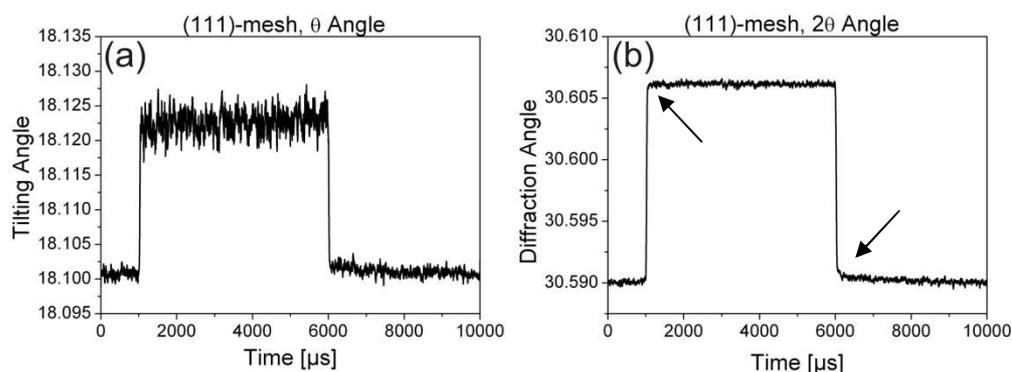
Figure 7.6: Time-dependent (a) θ and (b) 2θ peak angles for the mesh recorded at the (111) peak. Small relaxations are visible after switching the voltage on or off (1000 and 6000 µs, marked with arrows).

After the (111) peak, a mesh with a lower voltage of only 80 V was recorded at the (101) peak. The results are shown in figure 7.7. Fitting of potential relaxations was not possible due to the low signal to noise ratio. The total shift of the angles is also lower, which complicates fitting.
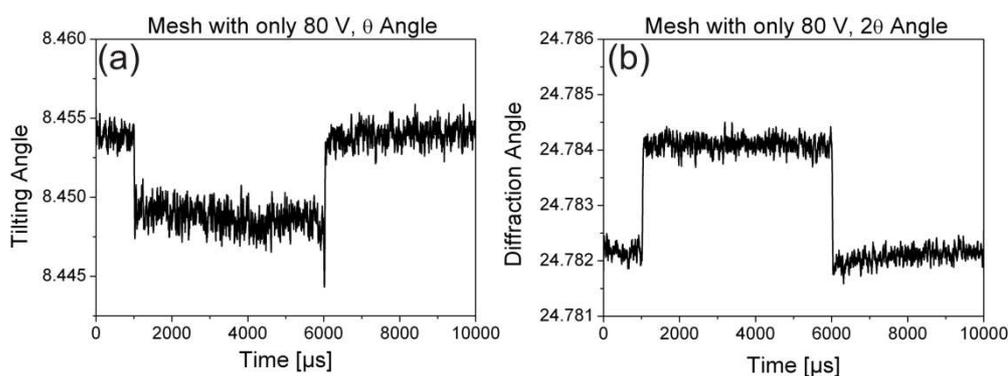
Figure 7.7: Changes in the (a) θ and (b) 2θ angles for the mesh with lower voltage (80 V). As the total shift is much smaller, the signal to noise ratio is also lower.

Now, the sample was heated up to a temperature of around 80 °C. The corresponding plots of changes of the (101) peak with time can be seen in figure 7.8.
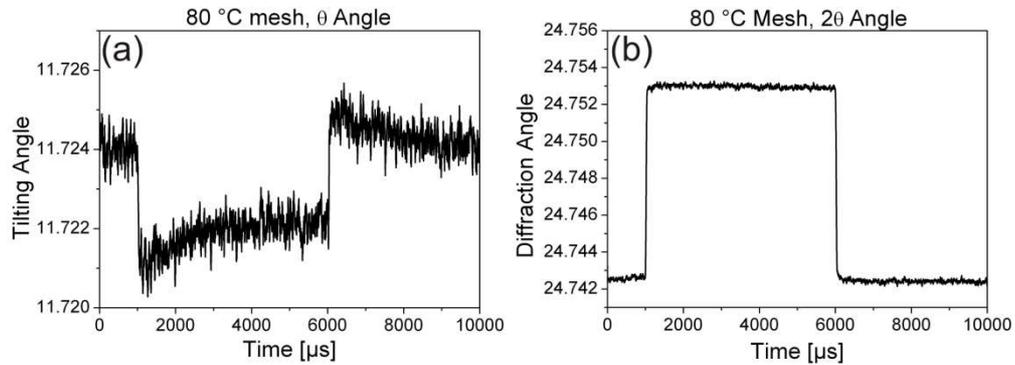
Figure 7.8: Periodic peak shifts of (a) θ and (b) 2θ for the mesh recorded at 80 °C at the (101) peak.

The next mesh was recorded at the same peak, but at 120 °C. Figure 7.9 shows the respective changes in the angles. Especially the θ angle (a) shows a totally unexpected shape, the short-time relaxation around 100-250 µs can nevertheless still be seen in both plots.
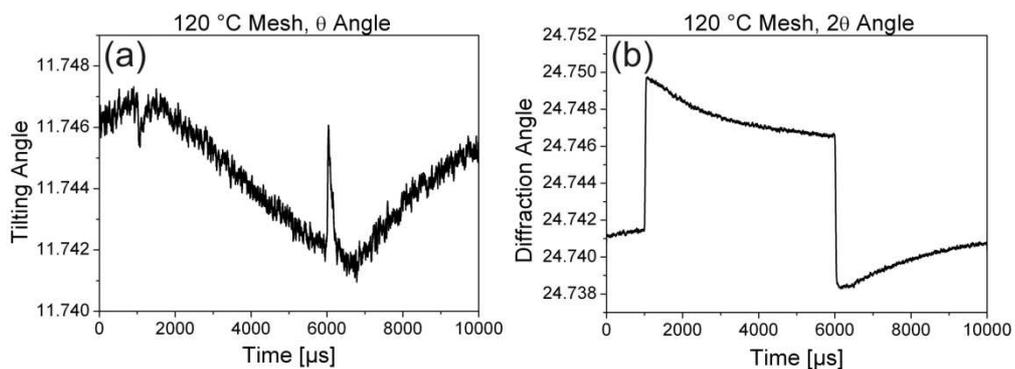
Figure 7.9: Time-dependent changes of the (a) θ and (b) 2θ angle of the (101) peak at 120 °C.

The setup was now cooled down to room temperature again. The next mesh was recorded with a shallower ramp of 3V/µs, but still 160V peak voltage. The graphs can be seen in figure 7.10. Again, the time-dependent peak shift in both directions, especially in θ, looks unexpected.
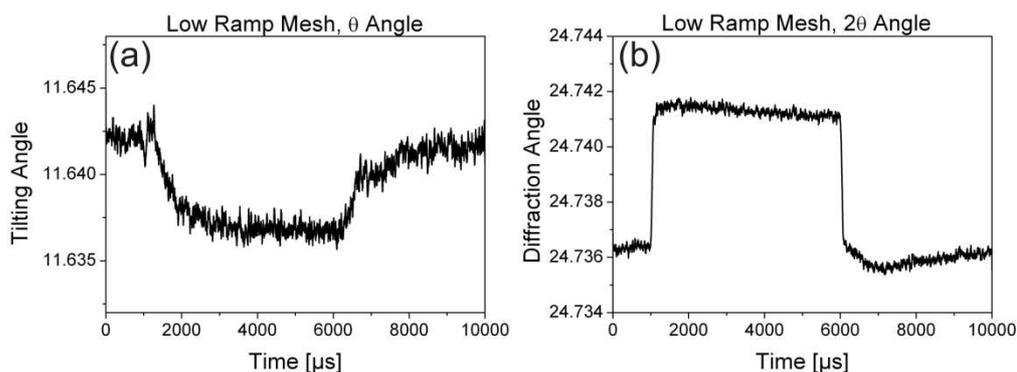
Figure 7.10: Plots of the (a) θ and (b) 2θ of the (101) peak in both directions when applying the voltage with a shallower ramp of 3V/µs at room temperature.

The last mesh at this beamtime was recorded at the (101) peak using a ramp of 1 V/µs; the graphs are shown in figure 7.11. The curves look similar to figure 7.10, but different to the other room temperature curves obtained earlier.
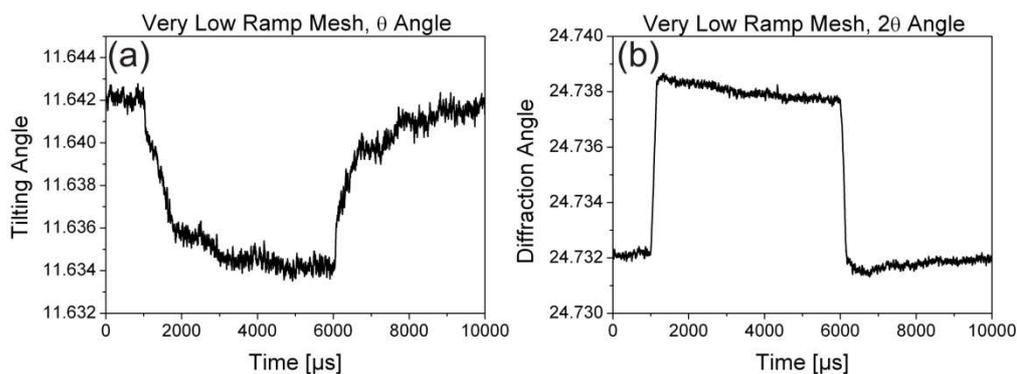
Figure 7.11: Time-dependent changes of the (a) θ and (b) 2θ angle when applying a voltage of 160V with a ramp of 1V/µs. Measurement was done at the (101) peak at room temperature.

7.3 Results at ANKA with the baby actuator

The baby actuator was used to minimize vibrations and in particular the movement of the sample. This was especially relevant for the experiments at ESRF, but some meshes with different parameters were nevertheless recorded at ANKA to test the setup and the stability. In contrast to the later ESRF experiments, the collective behavior of many grains of the actuator was studied. At first, we did an experiment with the "normal" parameters of 160 V at room temperature with a ramp of 5 V/µs. The plots for both angles are shown in figure 7.12. The scatter for θ (a) is much higher than for 2θ (b).
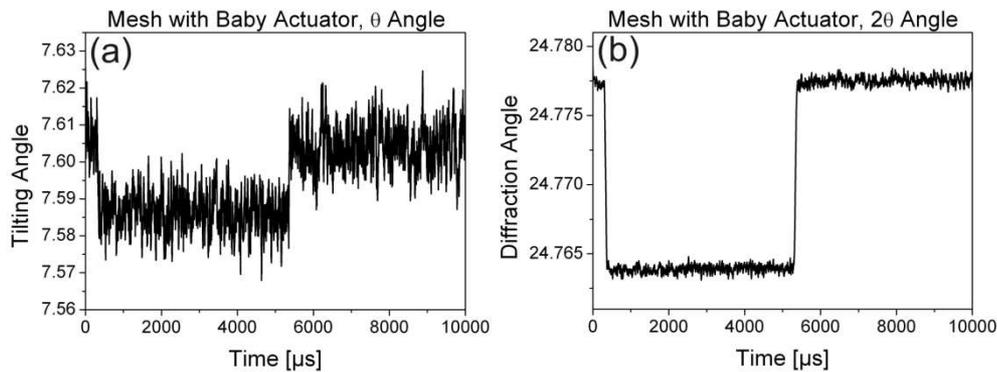
Figure 7.12: Peak positions of (a) θ and (b) 2θ for a mesh recorded at the (101) peak with the baby actuator under "normal" parameters (room temperature, 5 V/µs ramp, 160 V). θ shows a much larger scatter than 2θ.

Now, a mesh with a lower voltage (in this case with 90 V) was measured at the (101) peak. The corresponding plots of the fitted angles can be found in figure 7.13. Unfortunately, the scatter is very high, so no clear trends can be seen in these graphs. The smaller voltage leads to smaller shifts and so the signal-to-noise ratio gets lower.
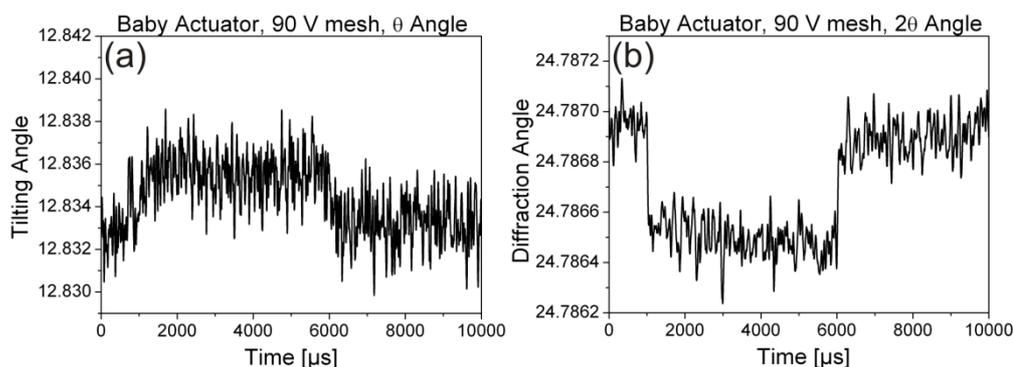
Figure 7.13: Plot of the fitted angles for a mesh with the baby actuator recorded at the (101) peak with a lower voltage of 90 V at room temperature. (a) θ angle, (b) 2θ angle. The signal to noise ratio is relatively low.

The experiments with a shallower ramp on the split actuator showed unexpected results (figure 7.10 and figure 7.11), so a mesh with a ramp of 3V/µs was now measured with the baby actuator at room temperature. The fitted (101) peak positions are shown in figure 7.14. No pronounced relaxations can be seen.
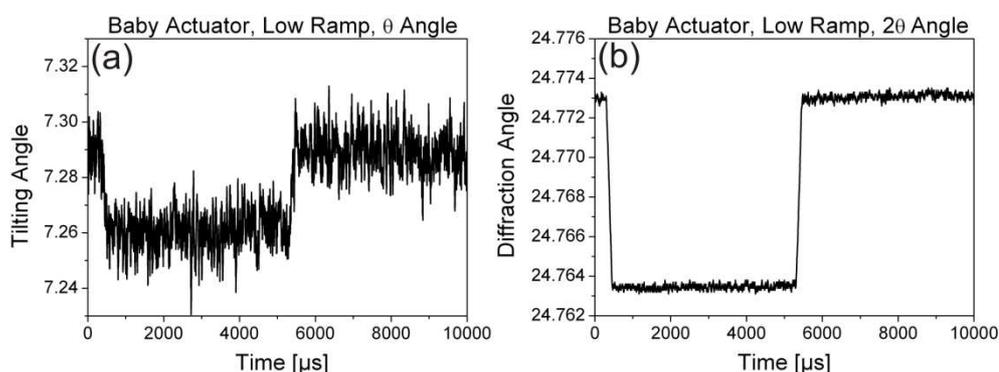
Figure 7.14: Fitted angles for the (101) peak mesh with a shallower ramp of 3 V/µs. (a) θ angle, (b) 2θ angle. The data for θ scatters more than the data for 2θ. No relaxations can be seen.

Now, three meshes were recorded at the (101) peak at elevated temperatures to check whether the data collected with the split actuator (see chapter 7.2, figure 7.8 and figure 7.9) were true effects or only artifacts. None of the curves showed

strong relaxations, the small relaxations as found in other curves before (figure 7.5) could however still be seen (see e.g. figure 7.15(b)). A first measurement was performed at 80 °C (figure 7.15). The data does not show similar effects as the split actuator data. All curves at elevated temperatures were measured at the same peak.
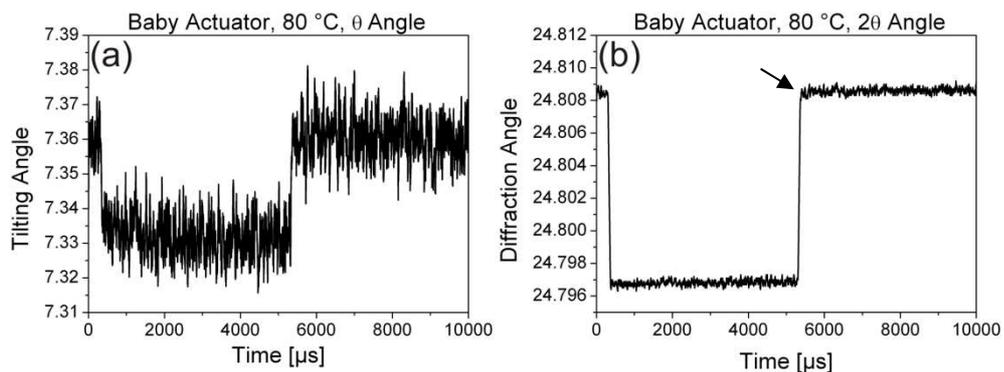
Figure 7.15: Data for the mesh recorded with the baby actuator at 80 °C, (101) peak. No strong relaxations can be seen for both angles, only the small relaxations seen in most experiments (marked with arrow in (b)). (a) θ, (b) 2θ angle.

The next measurement was done at 120 °C. The plots for both angles look very similar than for 80 °C, showing no relaxations or other unexpected effects (figure 7.16).
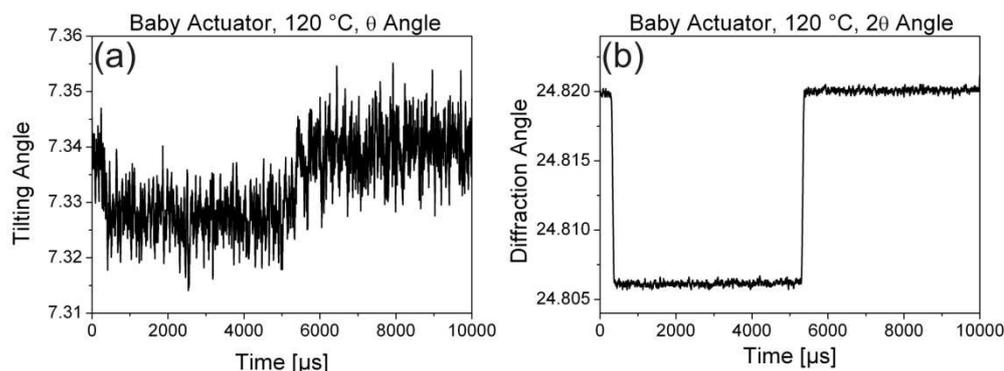
Figure 7.16: Plots of time-dependent angles for the (101) peak mesh recorded at 120 °C. (a) θ, (b) 2θ. No relaxations can be seen.

Now, a last mesh was recorded at 170 °C. The fitted angle positions over time are plotted in figure 7.17. The curves almost do not change compared to the curves for lower temperatures.
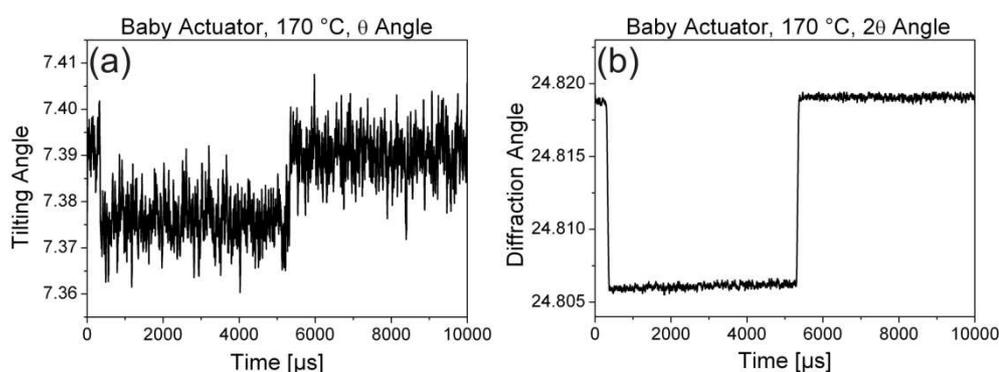
Figure 7.17: Plots for the (a) θ and (b) 2θ (101) peak positions fitted for the mesh at 170°. The curves look similar than for lower temperatures.

7.4   Results at ESRF with the split actuator

At ESRF, the whole meshes of (101) peaks were measured at different sample positions (see figure 3.16 (a)). First, the changes in the peak positions at the centre of the sample were studied. In contrast to the ANKA experiments, a focused X-ray

beam with a spot size of approximately 4x6 μm² was used to measure changes of single grains. The resulting changes in the angles are shown in figure 7.18.
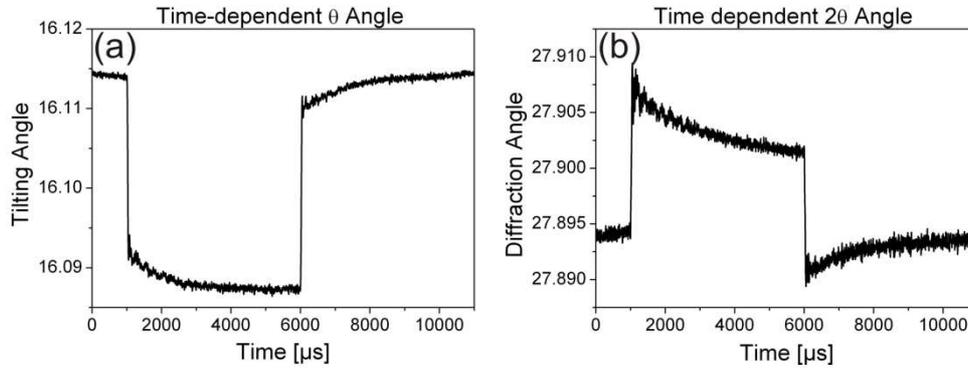
Figure 7.18: Time-dependent fitted (101) peak positions of (a) the tilting angle θ and (b) the diffraction angle 2θ of a single grain in the homogeneous field area of the actuator. Strong relaxations can be seen.

The angle positions show strong relaxations, but also slight vibrations that are still present, even though they are much smaller now that the split actuator setup is used. A second grain located in the inactive area close to the electrode edges was investigated. The fitted angles against time are plotted in figure 7.19.
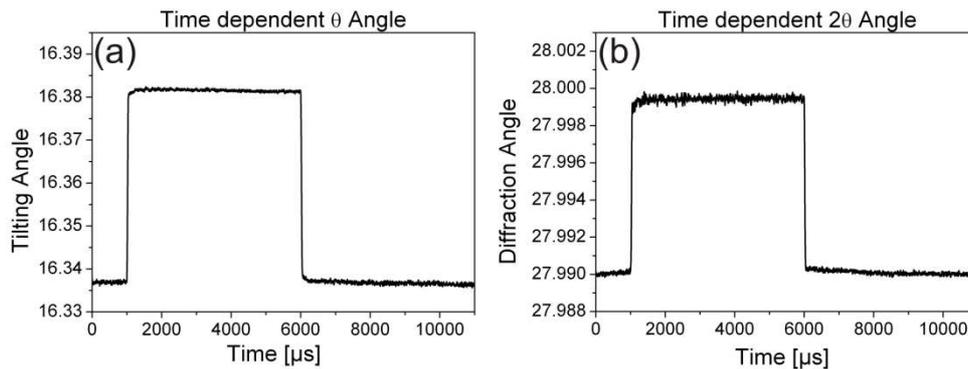
Figure 7.19: Time-dependent (101) peak positions of (a) θ and (b) 2θ in the inactive area of the actuator. Relaxations are much less pronounced.

The corresponding relaxations can in both cases be fitted using a simple exponential decay function or also a stretched exponential function with exponents close to 1. Both possible fits for one of the relaxations in the active area are shown in figure 7.20. No significant difference between the two curves can be found. The fits for the other relaxations are in good agreement with the values shown here.
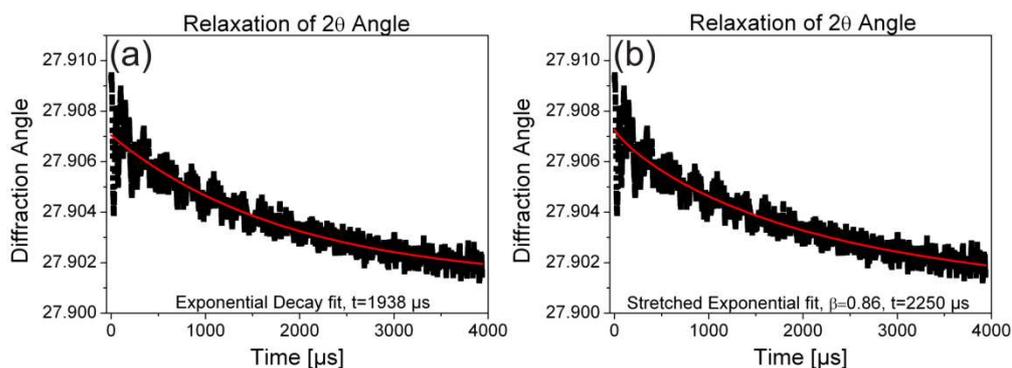
Figure 7.20: Two possible fits for one of the relaxations shown in figure 7.18. (a) Fit with exponential decay function, (b) Fit with stretched exponential. Almost no difference can be seen. The time axis has been rescaled to zero for fitting reasons.

The same holds for the curves in figure 7.19, for these relaxations also both fit functions give reasonable results which are shown in figure 7.21.
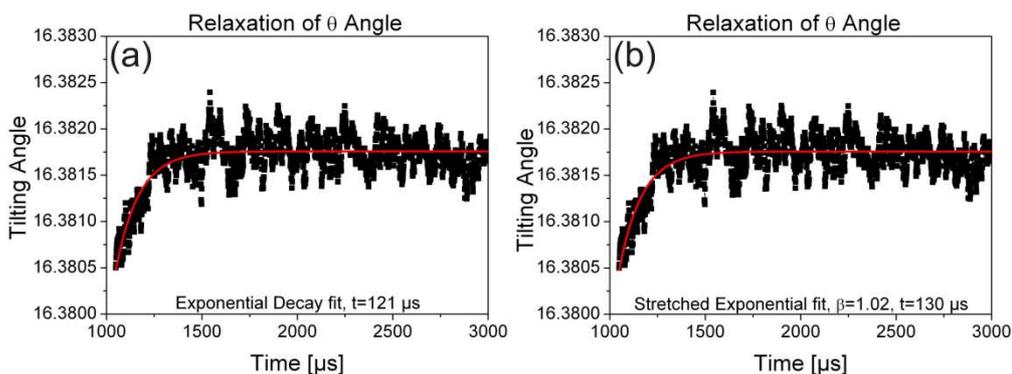
Figure 7.21: Fits with (a) exponential decay function and (b) stretched exponential functions for the grain investigated in the inactive area of the actuator.

Another possibility to evaluate the processes which occur during switching is the integrated intensity (the sum of all intensities of the whole mesh at a certain time) of the peak. We plotted the total peak intensity over time and also found a change after applying the electrical field. Figure 7.22 shows the plots for both cases. Both curves show a decrease of intensity when the field is applied, but in the centre area the relaxations are much more pronounced. The intensity loss may be due to domains moving out of the diffraction condition, e.g. 90° steps (as discussed later) or due to a movement of the sample when the field is applied. The full width at half maximum (FWHM) also showed a small trend, but was very difficult to fit reliably enough, so the values will not be shown here.
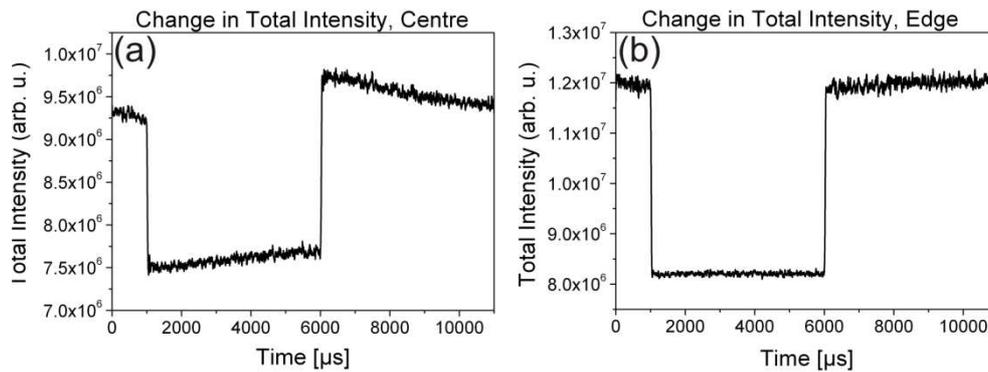
Figure 7.22: Time-dependent total sum of intensity in the mesh for the ESRF experiments. (a) Active Area, (b) inactive area of the actuator. In both case the total intensity decreases strongly when applying an electrical field. A strong relaxation can only be seen in the centre area of the actuator.

7.5 Results at ESRF with the Baby Actuator

The experiment performed at ESRF with the baby actuator are the largest part of this thesis, so the results will be shown more in detail than the results collected on other beamtimes. Altogether, 8 different meshes were recorded that are summarized in table 7.1. All meshes were measured at the (101) peak, as the intensities

of the other peaks were not high enough to perform time-resolved measurement with sufficient intensities in a reasonable time.

Table 7.1: List of all meshes recorded with the baby actuator on ID01 at ESRF.

Mesh No.	Grain position	Voltage	Ramp time
1	centre	160 V	30 µs
2	centre	80 V	30 µs
3	centre	160 V	90 µs
4	centre (2nd grain)	160 V	30 µs
5	centre (2nd grain)	80 V	30 µs
6	electrode edge	160 V	30 µs
7	electrode edge	80 V	30 µs
8	inactive area	160 V	30 µs

Several changes in the setup were made during and between the experiments to maximize the stability of the sample, but overall, peak positions did not remain stable. Especially the translational position parallel to the incident beam was unstable, which could be addressed to instabilities of the beamline setup (see chapter 3.3.2). Due to the monochromator we used, the beam was structured in a way that the signal of a grain showed up to five sub-peaks when scanning in y-direction (parallel to the direction of the incident beam). This effect is shown in figure 7.23.

Due to this instability, we had to include an automatic adjustment step in our mesh routine after each point at which the intensity was measured in time-resolution. As the sub-peaks were also not stable in intensity and number, this was reflected in the mesh surface plots, which did not show a "regular" structure as meshes recorded at ANKA, but showed intensity jumps on the shoulders of the peak (figure 7.24). This made it difficult to fit the peak positions of this mesh and has to be kept in mind when considering further results.
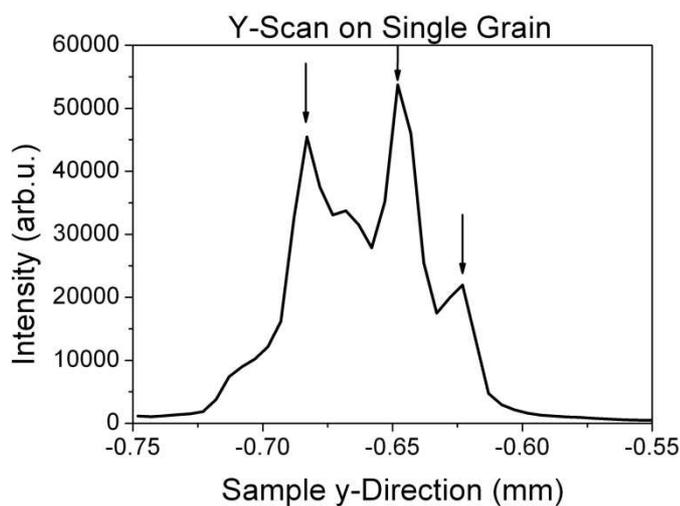
Figure 7.23: y-scan of the baby actuator on the signal of one grain. Several sub-peaks can be found due to the monochromator structure. These sub-peaks were not stable in relative intensities.
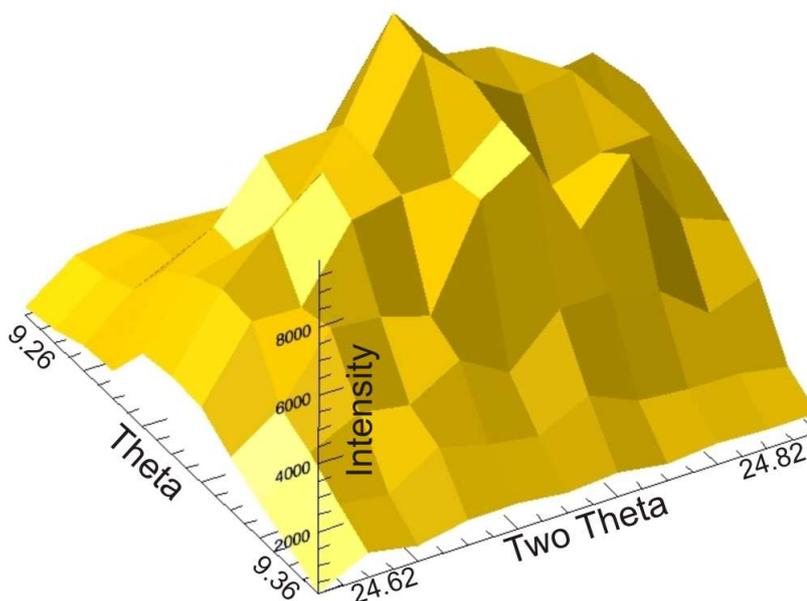
Figure 7.24: Surface mesh taken with the baby actuator at ESRF in θ and 2θ direction. The facets on the surface are due to the automatic readjustment of the sample during the measurement of a mesh in time-resolution. This was necessary because of the instability of the beam.

Keeping these problems in mind, we will not only look at the fitted angles for the experiments of this beamtime. We also will consider the time-resolved curves of all single Q points on the mesh, as these results should be more reliable than the fits. Another advantage of doing this is the larger data space available for analysis.

First, we will take a look at the meshes measured in the homogeneous active area in the centre of the sample with the typical parameters (No. 1 and No. 4, see table 7.1). The changes in the time-dependent angular positions for the first mesh are shown in figure 7.25. The basic curve shape looks comparable for both angles, after a sharp initial change of the angle two relaxations can be seen. More discussion about the nature of these relaxations will follow later.
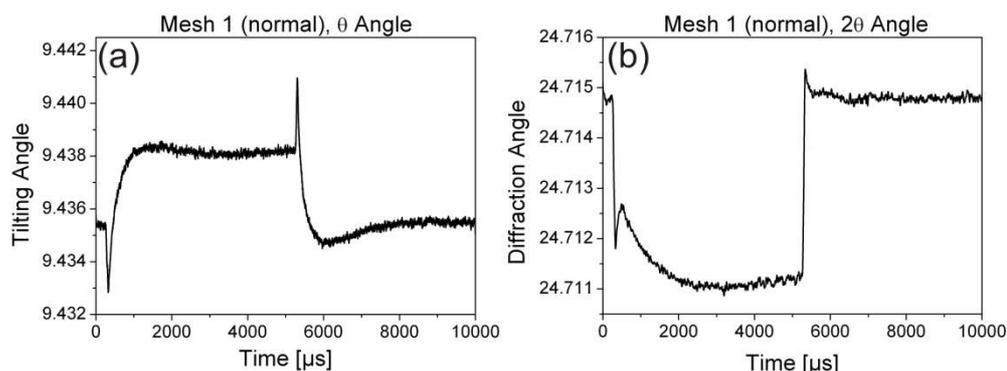
Figure 7.25: Fitted angles for mesh 1 (normal parameters, (101) peak, 160 V, 30 μs risetime, grain in centre of the sample). (a) θ angle, (b) 2θ angle. Two relaxations can be distinguished after an instantaneous change of the angles due to the electrical field.

For the same parameters, a second mesh at a different grain was measured. The fitted angles for this mesh can be found in figure 7.26. The similarities between both angles are now more remarkable than before. The shape is slightly different than for mesh 1, but some basic features remain. In all cases, switching the electrical field on or off will lead to a "two-step" response showing one faster relaxation and a slower relaxation in the opposite direction.
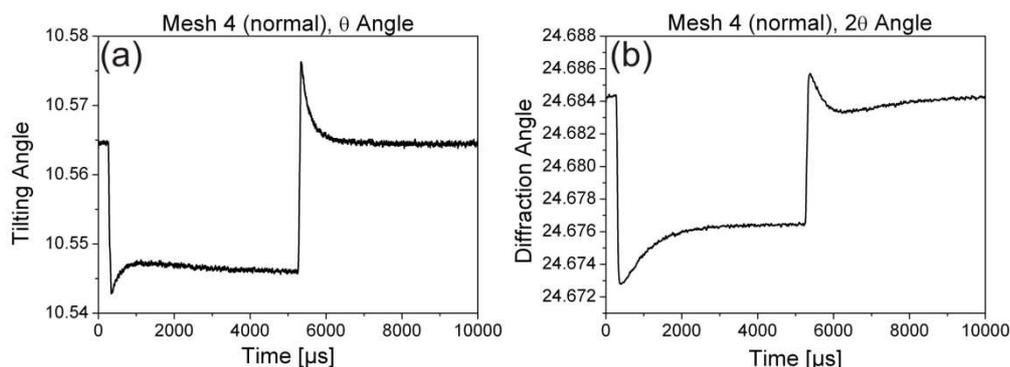
Figure 7.26: Fitted angles for mesh 4, measured under the same conditions than mesh 1. (a) θ, (b) 2θ angle. The shape is not similar, but the general trend is comparable.

To get an idea whether the response of the fitted angles to the electrical excitation is reasonable we can also look at the intensity curves at single Q points. As an example, 4 of these curves for mesh 1 are plotted in figure 7.27. The shape of the curves is not very different as they again show a "two-step" response. The basic changes in the mesh thus also seem to be reflected in the single point intensity changes.

For mesh 1 as well as mesh 4, some curves at single Q points exist where the curve shape looks different. Only one relaxation seems to occur after switching. Two of these curves, in this case taken from mesh 4, are shown in figure 7.28. It turned out that these curves also need two relaxation functions to be described well; the only difference is that both relaxations change the intensity in the same direction. A detailed discussion of the relaxations will follow later.
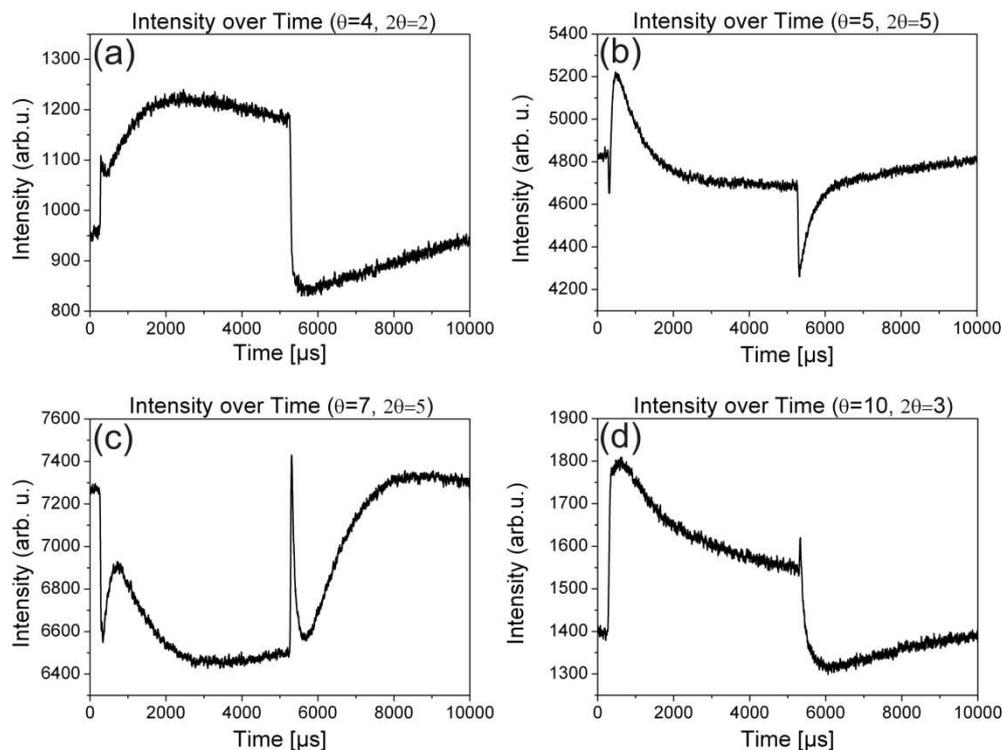
Figure 7.27: Examples for 4 curves of intensity against time at single Q points on mesh 4. The numbers behind θ and 2θ mark the Q-position on the (11x11) mesh. The principle shape, especially the nature of the relaxations, is comparable for all curves. At almost every point, a "two-step" relaxation can be found after switching the electrical field on or off.
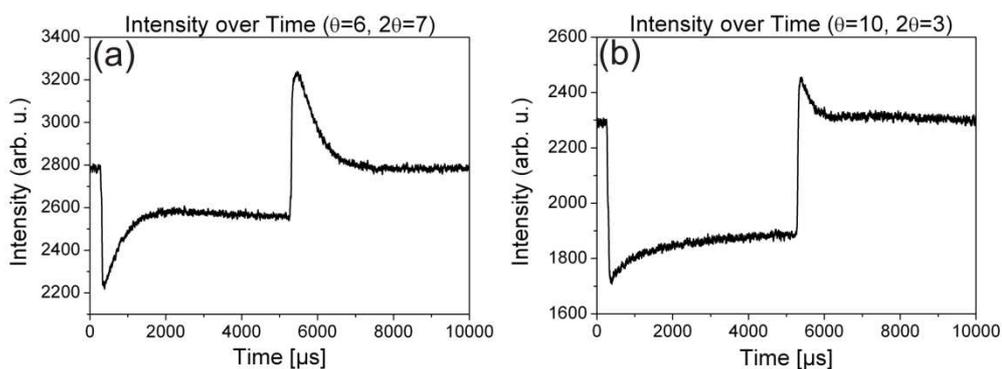
Figure 7.28: Example for 2 curves taken from mesh 4, intensity plotted against time. The curves look as if only one relaxation occurs after switching.

The curves shown here are only examples and some deviations exist, but the general trend is reproducible. Almost all curves show the shape as given in figure 7.27, so we can consider this as "normal" curve shape for the two meshes, which is also reflected in the fitted curve of the angles (figure 7.25).

Now, the two meshes measured in the centre area of the sample with a lower voltage of only 80 V will be discussed. In figure 7.29, the fitted angle curves for mesh 2 (recorded at the same grain as mesh 1) are shown. The basic trend of the measurement at higher voltage is still visible, even though the first relaxation appears to be weaker.
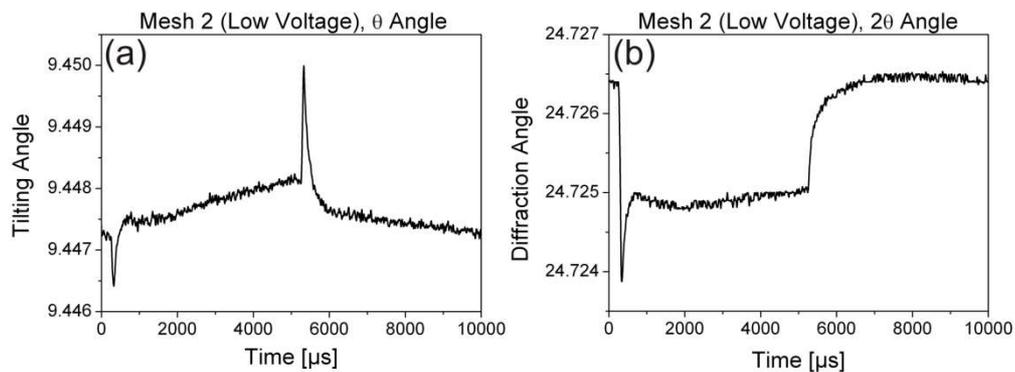
Figure 7.29: Fitted (a) θ and (b) 2θ angles for mesh 2, recorded at lower voltage. The general trend of curves is comparable to mesh 1, but the first relaxation is weaker.

The same parameters were chosen for mesh 5, where the same grain than in mesh 2 was investigated. The curves of the fitted angles are plotted in figure 7.30.
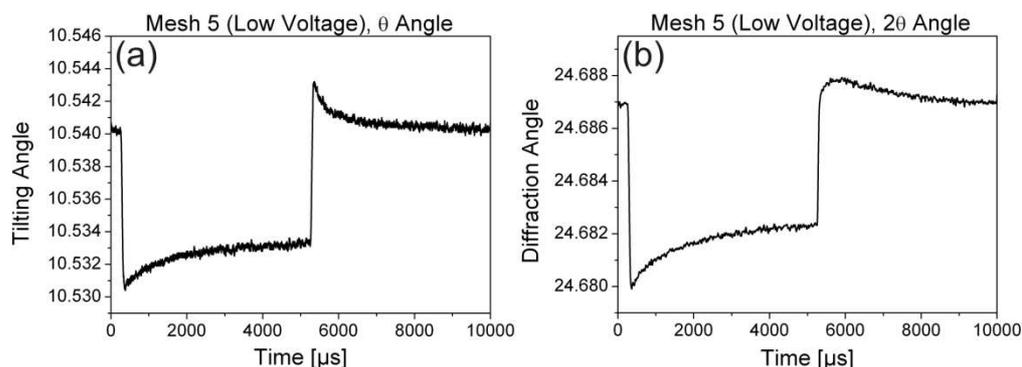
Figure 7.30: Fitted angle positions for mesh 5 taken at the same grain than mesh 4 with a voltage of 80 V. (a) θ, (b) 2θ angle. A difference to mesh 2 can be seen, but more detailed view on the data is necessary to verify this.

Compared to mesh 2, the curves look different because the first impression is that only one relaxation exists. A more detailed view can be given by looking at the curves at single Q points (figure 7.31). The curve shape is sometimes different to mesh 4, but also many curves look similar. Fitting reveals that still two functions are necessary to describe the relaxations properly, so altogether the curves can be treated similar.

To check the effect of a different, shallower ramp on the relaxation behavior of a grain, one mesh was recorded on the same grain as mesh 1, but now with a lower voltage ramp of 90 μs. The time-dependent angles for this measurement can be seen in figure 7.32. There is no significant difference compared to the other measurements, so the results of this mesh will not be discussed widely. The shallow ramp obviously does not have a big influence on the response.
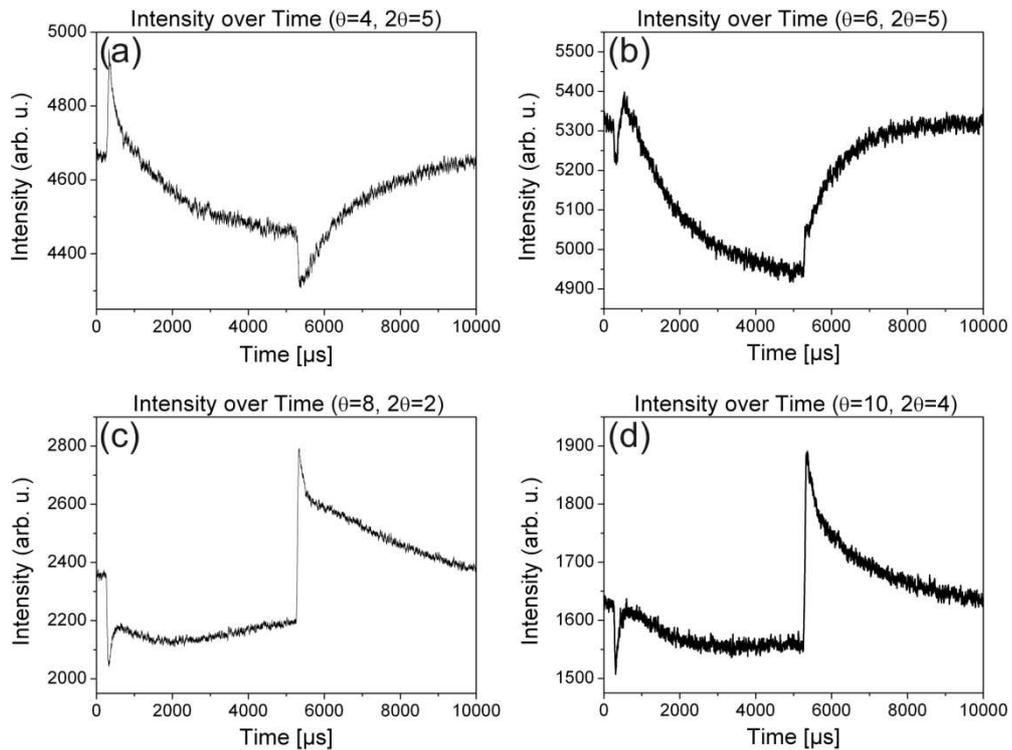
Figure 7.31: Curves of intensity against time for single Q points at mesh 5. The curves look a bit different to the curves of mesh 1 and 4, but still many curves have the shape with two strong relaxations.
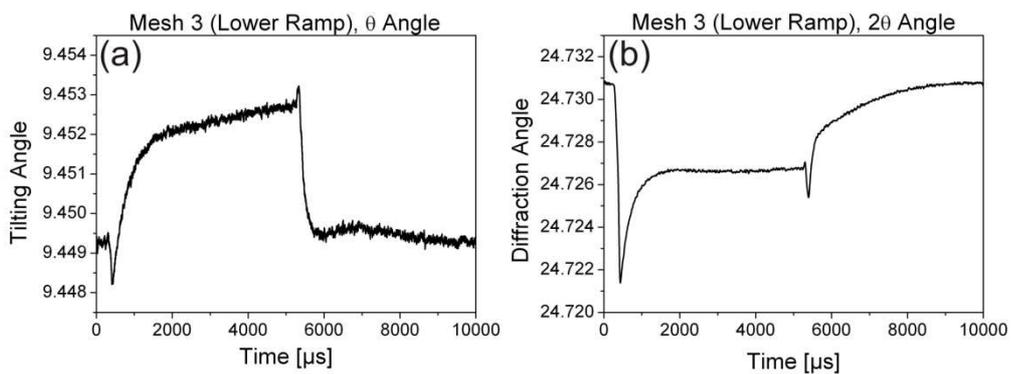
Figure 7.32: Plots of time-dependent angles (a) θ and (b) 2θ for mesh 3, recorded with a shallower ramp. There is no significant difference when comparing the results to the results obtained with a faster ramp.

123

Now, a grain directly at the edge of the electrode was selected. This is of special interest because this region is considered to be the origin of cracks and mechanical fatigue processes in the actuator (see chapter 2.3.3). The electrical field is inhomogeneous at the electrode edge giving rise to high mechanical stresses. With the experiment, we wanted to study whether the response of a single grain somehow reflects these high stresses and this might influence the fatigue behavior. The time-dependent angles are shown in Figure 7.33.
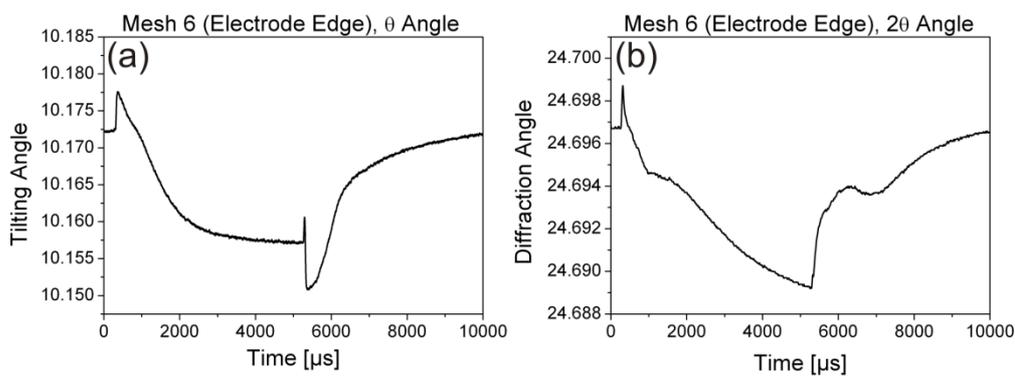
Figure 7.33: Time-dependent angles (a) θ and (b) 2θ for the mesh measured close to the electrode edge (mesh 6). The response of the angles looks very much different than for the other meshes.

In contrast to all the other curves shown up to this point, the response of the grain seems to be totally different this time. There is a stronger shift of the peak and very pronounced relaxations or oscillations can be seen. The same thing holds for the time-dependent intensity curves at single Q points that also show strong oscillation or relaxation behavior. Only as examples, 4 of these curves are shown in figure 7.34.
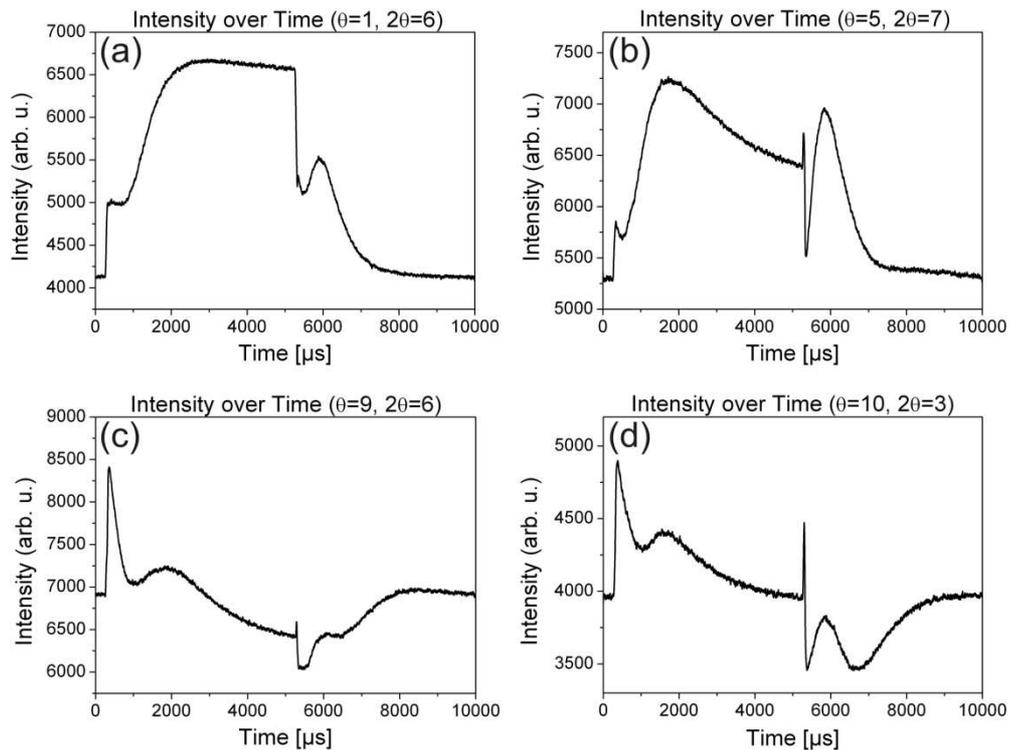
Figure 7.34: Intensity changes for mesh 6 close to the electrode edge, shown for 4 different Q points. In contrast to the other measurements, more than two relaxations or oscillations can be seen.

The total set of curves shows many different curve shapes, but they almost never look similar to the curves for the grains in the centre of the actuator. More and stronger relaxations are found, often looking more like periodic oscillations.

The next mesh was still recorded at the same position on the sample, but now again with a lower voltage of 80 V. The curves for the fitted angles can be seen in figure 7.35.
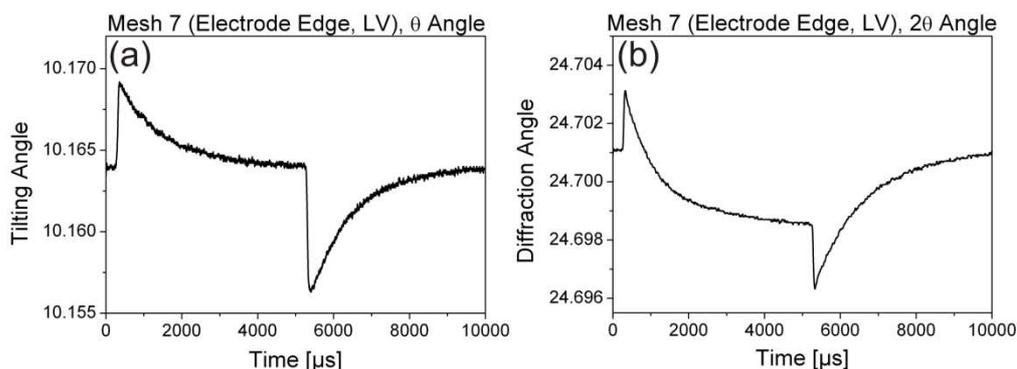
Figure 7.35: Fitted (a) θ and (b) 2θ angles for the mesh measured at the electrode edge with a lower voltage. There is not much agreement with the data of mesh 6, but still 2θ shifts in the same direction (in contrast to the grain position in the centre of the actuator).

For this mesh, the curves show a weaker response than for mesh 6, the strong oscillations seen there do not appear. On the other hand, there is still a shift of 2θ in positive direction after the field is applied. This is unexpected, because we normally investigate lattice planes expanding parallel to the external electrical field with the baby actuator setup, which is also confirmed by the results obtained before where only negative shifts can be found. In spite of this, the shape of the relaxations looks more like for the other meshes recorded with a low voltage. The curves for the individual Q points support this trend, but do not show special unexpected effects, so they will not be discussed here.

For the last mesh of this beamtime, a grain in the inactive area of the actuator was selected. Here, only a small electrical field should be present and no strong response on the external excitation should be measured. The graphs for the time-dependent angles are shown in figure 7.36. Curves for single Q points also look similar.
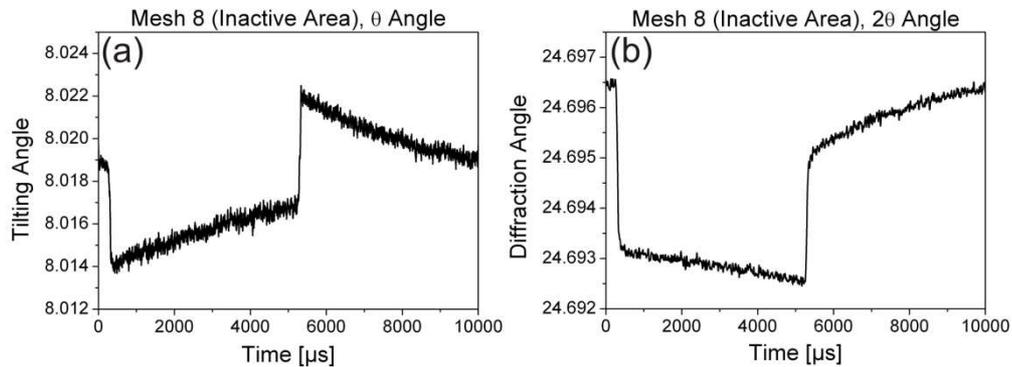
Figure 7.36: Fitted (a) θ and (b) 2θ angles for the mesh data collected in the inactive area. No strong relaxations can be seen; the curves look more like a constant slope.

For this experiment, the plots of the angles against time look completely different than for all the other measurements. No strong relaxation can be seen; the changes after applying a field look more like a change of angle with an almost constant slope or a much longer relaxation time. The intensities for the single Q points show a similar behavior.

7.5.1 Summary

Many differences can be seen in the curves of all the different meshes. As a general trend, we can say that the voltage ramp does not seem to have a strong influence on the curves, the voltage only seems to have a small influence (the first relaxation is weaker), while the position on the sample changes the curve shape dramatically. In the centre area of the actuator, the homogeneous electrical field seems to trigger two relaxations in the material. Close to the electrode edges, a stronger response of the material can be see, while the material relaxation in the inactive area is comparably weak.

7.6 Discussion

7.6.1 ANKA results

7.6.1.1 General effects

The first part of this discussion will focus on the ANKA data, where we worked with a larger beam spot illuminating many grains of the actuator. We thus do not measure the response of a single grain although some peaks could be separated well when doing a rocking scan (figure 6.3). The amount of background from other grains is still relatively high, so the results will not show the response of single grains, but of groups of grains with similar orientations. With our beam size of 200x500 μm² and a typical θ angle of 12°, the footprint of the beam on the sample is 1x0.5 mm². With an average grain size of around 1 μm, the beam illuminates about 500.000 grains only at the surface, not even considering the grains deeper in the material that still contribute to the diffraction signal (the penetration depth is around 5 μm). In addition, several domain orientations exist in each grain. It is obvious that this large amount of grains cannot be separated in the X-ray signal.

First time-resolved experiments performed at ANKA showed strong oscillations in the time-dependent intensity signal. Different reasons for these vibrations can be discussed. At first, they might remind of the work of van Reeuwijk et al.[84], where periodic oscillations in the signal could be attributed to the excitation of strain waves in a single crystal. These waves are reflected at the crystal edges and spread through the crystal at the speed of sound.

If we do a simple calculation, in which our actuator is treated as a single crystal without internal boundaries, and assume a speed of sound v of 3000 m/s (ref.[137]) in PZT, we can calculate an expected period P of:

$$f = \frac{v}{2*l} = \frac{3000\frac{m}{s}}{2*0,03m} = 50kHz \Rightarrow P = \frac{1}{f} = 20\mu s$$

l is the length of the actuator and f the frequency of the oscillation. A frequency analysis of the data shown in figure 7.1 reveals that no frequency peak can be found close to the expected 50 kHz (figure 7.37), the dominant frequencies are around 4.3 and 8.6 kHz, so the vibrations are not due to elastic waves in the crystal. Such a process would be difficult to measure because many interfaces are present in the multilayer actuator, and all of these interfaces can reflect waves. If the waves spread in only one layer and are reflected from the electrodes, the resulting frequency would be 30 MHz and too high to be resolved with our method.
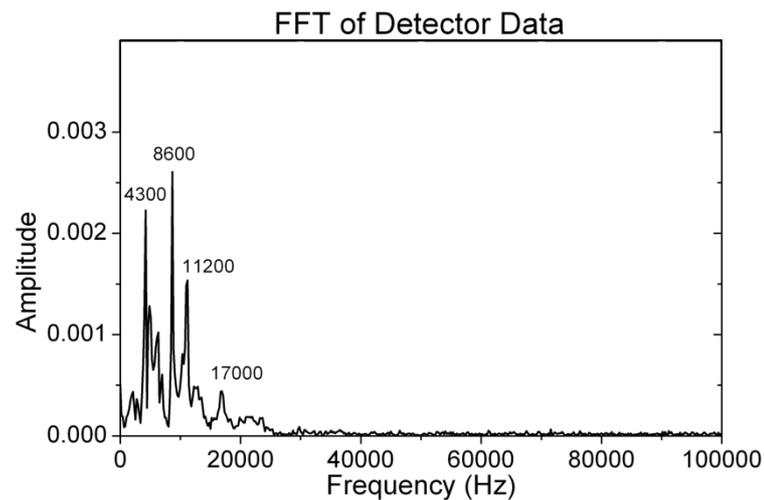
Figure 7.37: FFT analysis of the time-resolved data received in an experiment at ANKA. The dominant frequencies are in the low frequency-range.

Frank Felten from the Robert Bosch GmbH did a frequency analysis in a finite element method (FEM) program with the full system of the actuator, spring and frame and found that the dominant eigenmodes of the system do indeed lie at around 9 kHz, so the periodic oscillation of the actuator induces the eigenvibrations of the system sample plus sample holder. The vibrations are a relatively

strong effect and mask possible relaxations we want to study. To solve this problem, the split actuator setup was built as described in chapter 3.3.2. The signal of a piezo bimorph sensor, which was glued on a disc close to the sample (Figure 7.38), was used to minimize the vibrations in the system. A disadvantage of this setup is the fact that the pre-stress cannot be adjusted exactly, so the screw was tightened manually as reproducibly as possible. Part of the pre-stress is nevertheless applied by switching on the outer parts of the actuator, which leads to an expansion. Different pre-stresses should partially change the amplitude of length change and the fraction of domain wall movement; the basic mechanisms should nevertheless be unaffected.
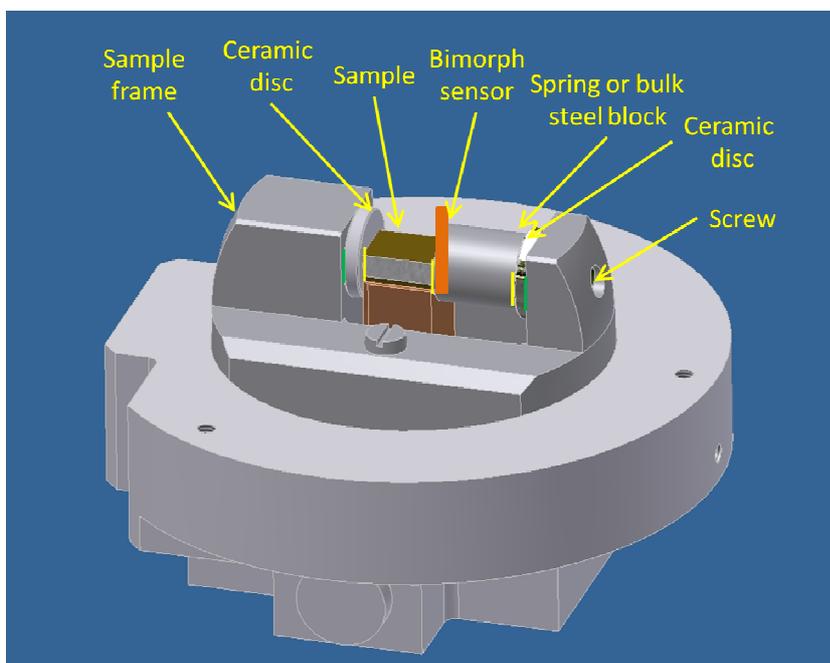
Figure 7.38: Drawing showing the positions where the sample is glued (yellow) and not fixed (green). In orange, the position of the piezo bimorph sensor is marked.

7.6.1.2 Quasistatic changes

First, the equilibrium (quasistatic) changes after application of the electrical field will be discussed (see fitted angles in figure 7.4). Applying a field leads to a shift of the lattice plane distance, which was discussed widely in the last chapter. The

direction of this shift depends on the orientation of the lattice planes with respect to the direction of overall expansion of the actuator, since the collective length change is a stronger effect than the local change in the few grains we are investigating. Movements of the sample as a whole might also influence the changes in 2θ (see chapter 6.3).

A second effect is a change in the tilting angle of the lattice planes. This is primarily a trivial effect, because the expansion of the c-axis and the compression of the a-axis lead to a change in the tilting angle of the (101) planes (figure 3.10). The material is polycrystalline, so the shape change of neighboring grains affects changes in the grains we are measuring. The total measured shifts are also smaller than the shifts we would expect if the grains could change their shape without influences of neighboring grains. If we calculate the value with our lattice parameters, the expected shift is 0.26°; we usually obtain values close to 0.05°. This can be explained when we assume that the grains are under stress and cannot change their shape freely.

It is known in the literature that static changes in a piezoelectric crystal can also be used to determine the piezoelectric constants. Following the method of Bhalla et al.[138] and Barsch[139], the piezoelectric d_{33} value can be determined from our results using:

$$d_{33} = -\cot\theta \frac{\Delta\theta}{2\Delta E}$$

(7.1)

where θ is the diffraction angle, $\Delta\theta$ the change of θ when an electrical field is applied and ΔE is the change in the electrical field. This is valid if the electrical field is applied in the z direction (parallel to the c axis of the crystal). This does not include the tilting of the unit cell. As an example, we can take the values of figure 7.2, when 2θ shifts by 0.011° (and thus θ by 0.0055°) with an applied electrical

field of 180 V/100 μm. From equation (7.1.) and assuming a stress-free state we obtain a d_{33} value of:

$$d_{33} = 5000*10^{-12} m/V .$$

This does not match the PZT literature data of around $600*10^{-12}$ m/V (ref.[140]). Our method is not suitable to determine piezoelectric coefficients. To calculate piezoelectric constants, experiments have to be done on stress-free single crystals. In our case, the material is polycrystalline, so neighboring grains influence the expansion of the grains we study. Furthermore, we do not know the exact orientation of the grain with respect to the electrical field. The shifts are larger than expected when considering the stress-free single crystal, but other experiments on polycrystals show similar results[38]. The collective response reflected in the peak shapes is thus stronger than the pure piezoelectric coefficients would suggest.

7.6.1.3   Relaxation response

From the experiments performed at ANKA with the split actuator, we can conclude that a small relaxation after switching can be seen. Relaxations can be described using different mathematical models, such as exponential or stretched exponential functions. In our case, an exponential relaxation function

$$I = I_0 \cdot e^{\left(-\frac{t}{\tau}\right)}$$

(7.2)

with a relaxation time τ of 100-250 μs (see figure 7.5) describes the data well. A comparison with the other experiments and an interpretation on this will follow later. With our method, even very small shifts can be resolved precisely. The oscillations in the fitted angle positions are larger in θ than in 2θ.

First, the sample is better fixed against vibrations in the direction of expansion due to the pre-stress. Transverse vibration oscillations are still possible, because the actuator assembly is at both ends free (see figure 7.38). A second explanation is the automatic fitting routine that is used to determine the angle positions at each of the 10.000 time sequences of 1 µs. The peak shape is much better defined in θ-2θ direction than in θ direction (figure 3.9), which makes fitting much easier. We can thus conclude that the fitting errors in θ direction are usually higher, so the fit values will scatter more. This is also indicated by the lower R^2 values when fitting θ (0.95, taken from the data of mesh 1) compared to 2θ (0.98). Another indication that this might be the reason for the scatter in the fitted data is the fact that for some meshes, the θ data can be fitted just as well as for 2θ (see e.g. figure 7.4 (a)), while for other meshes, where θ obviously was not as well defined, the data scatters more strongly (figure 7.6 (a)).

7.6.1.4 Influence of temperature and ramps

In a series of experiments, we studied the influence of different parameters on the relaxation behavior of the split actuator at ANKA. The voltage ramp was changed as well as the total voltage, the temperature and a mesh of a different lattice plane type was measured. The first experiments measured with the split actuator at ANKA suggest that changing the temperature has a strong influence on the response of the lattice planes (figure 7.8 and figure 7.9). Surprisingly, the strong relaxations are still visible after returning to room temperature, especially in the time-dependent θ angle (figure 7.10 and figure 7.11). Intuitively, this is difficult to explain, normally only changing the voltage ramp should not change much of the response of the actuator. In contrast, one would expect that a shallower ramp would lead to a smoother response as the voltage is not applied as "rough" as it was before. The fact that this effects occurred after heating up the sample leads to two possible explanations.

First, the heating process might influence the microstructure which leads to changes in the response of the material; on the other hand we might also have to deal with a measurement artifact. In general, heating might lead to diffusion, phase transformations, grain growth or other possible modifications in the material. Some of them, like phase transformations, are mainly reversible, even though a hysteresis effect exists due to the activation energy of the process. As the sample was cooled down back to room temperature before the experiments with lower ramps were done, one would not expect that any phase change occurs in this experiment. Also, we are far off the Curie point at this composition, so the only possibility would be a change between tetragonal, rhombohedral or a potential monoclinic phase in the material. Even though one could think that this influences the relaxation behavior, it seems rather unlikely that this change is so strong and still fails to explain why the response remains different after cooling down again.

At elevated temperatures, diffusion can change the microstructure much faster than at room temperature. Diffusion of Ag from the electrode into the PZT layers has been reported to occur[141], but only at higher temperatures (500 °C-750 °C) and slowly. A saturation concentration of 0.2 % was not exceeded. Altogether, no strong diffusion effects could be found between PZT and AgPd electrodes[142]. Diffusion always needs thermal activation[143] and we do not expect that it happens fast enough at room temperature to influence the microstructure during the experiment. Finally, one-directional diffusion due to stress gradients would lead to a steady state, which means that an effect that occurs during the measurements should vanish or at least decelerate during the experiment, which is not the case. The only remaining possibility is a diffusion process that is fully reversed when switching off the actuator, which is very unlikely as stresses should be different in on-switching and off-switching process.

A final possibility of what might change the microstructure at elevated temperatures is a crystallographic process like grain growth or recrystallization. As stated

in literature[144], recrystallization occurs only at temperatures above 0.4 to 0.5 times the melting temperature (in K), and for PZT which melts at above 1300 °C[145], the temperatures of the experiment are by far too low.

To conclude, the strong response of the split actuator found at some experiments is an artifact. The sample has several glue spots and if one of them is in too close contact with the heating block the glue might melt or dissolve, even though the epoxy glue should in principle be stable enough for temperatures up to 200 °C. In this case, a periodical movement or tilting of the sample might be reflected in the results. Also, the different thermal expansion coefficients of sample and frame might lead to a loosening of the sample. Later results with the baby actuator at elevated temperatures (see chapter 7.3) did not show any changes in the response of the actuator. Therefore we do not expect that our measured relaxations and vibrations with the split actuator are effects due to the piezoelectric response of the sample. The experiments at ANKA with the split actuator did thus not show any influence of temperature, voltage and ramp, at least as long as the measurement setup was stable.

7.6.1.5 On the actuator relaxation

The next experiments were done with the baby actuator. Now, the lattice planes parallel to the surface expand in field direction, which is an advantage when studying effects due to the applied field, as we now have a more direct effect than the lateral contraction measured before. Due to the electrode on the surface (which was partially removed) we also investigate lattice planes close to the electrode, so effects which are related to the direct contact of electrode and ceramic would appear in the measurement more strongly than before. The special geometry of only four active layers on top of a 4.6 mm long inactive ceramic foot leads to a constraint in the lateral contraction, which might influence the results and should be kept in mind. Nevertheless, the setup has advantages which simplified especially

the position-resolved measurements at ESRF, because the low overall expansion leads to a high mechanical stability of the setup.

Pre-experiments with the baby actuator were done at ANKA. For these experiments, the angle positions in θ scatter much stronger than they do for θ-2θ. This can be explained by less fitting accuracy due to the less pronounced peak shape or possible torsional vibrations that partially also occurred with the baby actuator. The influence of several parameters on the time-dependent response of the actuator was studied. For the standard conditions, almost no relaxation of the actuator was seen, at least in 2θ where the scatter was low (figure 7.12(b)). This does neither change when lowering the voltage, nor when raising the temperature up to even 170 °C. The only change is a slightly higher shift of 2θ when the temperature gets higher, which means that the piezoelectric response of the crystal gets larger at higher temperatures. Similar results are found in literature[146]. To summarize the data from ANKA, in some cases see a small relaxation of the angles with relaxation times close to 100 or 200 μs can be seen. Potential reasons for this will be discussed later.

7.6.2 ESRF results

At ESRF, we only studied the response of single grains, which can be seen when comparing the rocking scan data in figure 6.3 (ANKA) and figure 6.5 (ESRF). We can completely separate the signal of a single grain from other grains. It is also possible to select grains in designated positions we are interested in by scanning the sample in translational directions.

7.6.2.1 Split actuator

On the first beamtime with the split actuator, the stability and reproducibility of the results was not satisfactory. After cycling the sample, the sample position often had to be readjusted. There are several possible explanations for this. First, the

sample chamber for the split actuator was not fabricated in a way that stability in the sub-μm regime was guaranteed. With the small beam spot of 4x6 μm², high mechanical stability of the whole setup is necessary to get reliable results. The base of the chamber is fabricated of a macor ceramic[147] which can be machined quite simply and has the advantage of a good thermal conductivity. Nevertheless the screw holes and other mechanically fixed parts of this setup were not fabricated with high precision. The sample frame and its glue spots might also not be stable enough, especially when exposed to cyclic loading. There are two positions which are not glued (see figure 7.38), so the sample could periodically move. On the other hand, there were indications that the beamline setup was moving and ESRF suffers from beam path position problems. To exclude problems with our setup, we later started to perform experiments with the baby actuator, which ensures maximum mechanical stability.

Keeping these difficulties in mind, we finally measured two grains at different sample positions, which for unknown reasons turned out to be more stable than other grains which were measured earlier. In this case, the reproducibility was sufficient to measure the whole mesh without having to readjust the position during the measurement.

Comparing the results from the central area and the inactive area, we can see a strong relaxation behavior, but only for the grain located in the active area of the actuator. The inactive area shows a smaller relaxation at shorter times which looks similar to the measurements at ANKA, where this small relaxation could also be seen in many of the experiments with the split actuator (see figure 7.5). This would suggest that we see a collective effect which is also reflected in the single grain behavior. If we look at the amplitude of both relaxations, it is possible that the grain in the centre area of the actuator might show this small relaxation in addition and it is only overlaid by the stronger signal of the second relaxation. We can assume that the relaxation is either a collective stress relaxation effect or re-

flects an effect in the amplifier signal. If the amplifier does not immediately reach the exact final voltage, but has a small delay at the end of the pulse, this would also lead to a relaxation in the grain signal. The reproducibility with which this effect occurs at any temperature or measurement conditions suggests that it is an amplifier effect.

We can now try to fit the data we obtained in the centre area of the actuator with an appropriate fitting function. A stretched exponential function (equation 2.10, see figure 7.20 (b)) was used, which will later play an important role when discussing the data for the baby actuator to describe potential domain processes. Fitting of the curves at single Q points was unfortunately not successful due to the low signal-to-noise ratio.

From figure 7.18 and figure 7.22 (a), we can fit six relaxations. The relaxation times range between 840 and 2700 µs and the stretching exponents between 0.77 and 1.09. A more detailed discussion will follow later in the context of the other ESRF experiments.

7.6.2.2 Baby actuator

At the second ESRF beamtime, we performed experiments with the baby actuator. We studied different positions and parameters to measure the response of single grains to the external excitation by the electrical field. There are several differences compared to the split actuator setup, as we can now study lattice planes expanding parallel to the electrical field. Also, sample movement was excluded due to the stable setup with only four active layers.

Altogether, 8 meshes of the (101) peak were measured under different conditions (table 7.1). Two meshes were recorded in the centre of the actuator under normal conditions, a voltage of 160 V and a high voltage ramp of 5 V/µs, but at different grains. Two more meshes were measured at the same sample positions, but with a

lower voltage or a shallower ramp of around 2 V/µs. Two other sample positions were also studied, one in the inactive area away from the electrode edge, one close to the electrode edge, where high mechanical stresses are expected. Close to the electrode edge, a last mesh with a lower voltage was measured. The results show that we mainly have to distinguish between five cases: three different sample positions measured at high voltage and the meshes with a lower voltage and ramp. We will first discuss six meshes which show comparable results: the meshes measured in the centre of the sample at higher and lower voltage as well as with a higher and shallower ramp (meshes 1-5) and the mesh recorded at the electrode edge with a lower voltage (mesh 7). The two remaining meshes, mesh 6 at the electrode edge with a higher voltage and mesh 8 in the inactive area, will be discussed later.

We still had instability problems even after excluding all possible sources of movement in our setup. The stability of the sample holder was tested later using a dial gauge and no movement was detected. The monochromator of the beamline was moving. An indication of the beamline instability were stripes in the beam (reflected in the peak shape, see figure 7.23) which changed their intensities during the experiment. The stripes arise from stripes in the monochromator and if they change their position this means that the incoming or diffracted beam from the monochromator also changes its position. This affects the quality of our results, especially as they are collected in relatively long times. Therefore, it is of high interest to consider also changes in the signal at single Q points where data was collected in shorter time (2 minutes per point, 5 hours for the whole mesh). Altogether, all the results obtained for the single Q were analyzed and we studied the switching-on process as well as the switching-off process.

To verify the reproducibility of our measurement, we repeated a measurement at single Q for five times. The corresponding intensity curves are shown in figure 7.39. The curves are shifted for better illustration, intensities and curve shapes are very well reproducible.
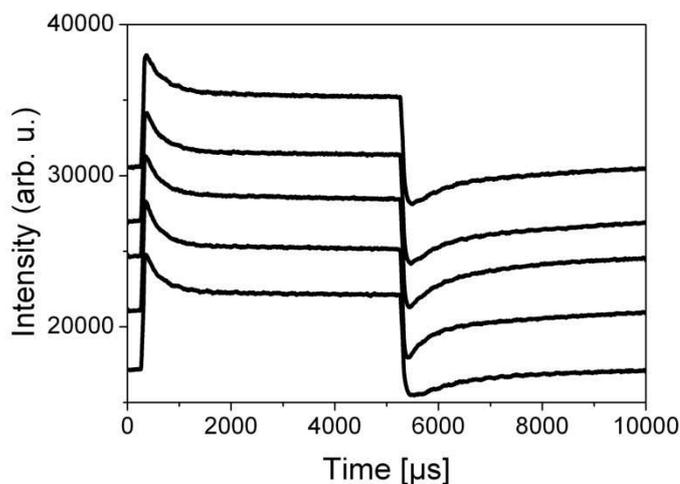
Figure 7.39: Five time-dependent intensity curves measured at the same Q point. The experiment was done with the baby actuator at 160 V and room temperature. The curves are shifted for better illustration. The reproducibility is good.

Most curves at single Q are shaped similarly (figure 7.27). Two effects can be seen after an electrical field is applied at around 250 µs total measurement time. First, the intensity (or angle) changes instantaneously due to the electrical distortion of the unit cell, which reflects the direct intrinsic piezoelectric response. After that, a slower process which often can be described with two relaxations (Figure 7.40) can be seen. This will be the focus in later discussions. In most cases, these two relaxation processes change the intensity in opposite direction, sometimes they "point" in the same direction. This relaxation behavior can be seen more or less in every mesh which we measured in the active area of the actuator, with only minor changes.
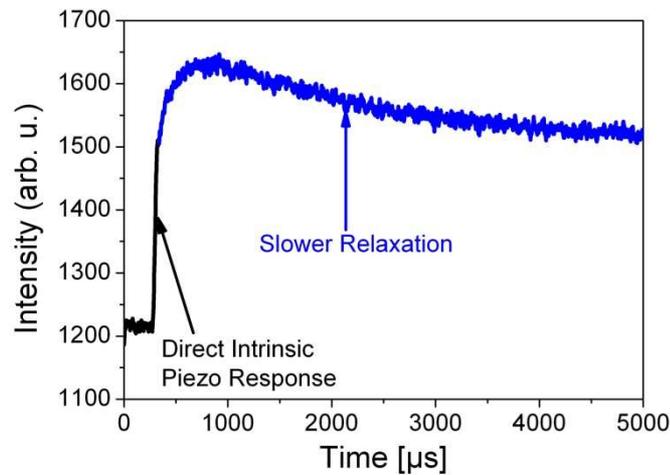
Figure 7.40: Example for the processes occurring when an electrical field is applied, detail from figure 7.39. The intensity changes instantaneously due to the piezoelectric effect, but other slower processes can also be seen. In this particular case, a faster relaxation raises the intensity, and afterwards, the intensity decreases with a slower relaxation.

Some of the possible mechanisms which can appear as relaxations in X-ray experiments were mentioned earlier in the discussion of ANKA results (see chapter 7.2). An additional possibility would be a global stress and strain relaxation of the actuator, but in this case, the relaxation behavior should be at least qualitatively similar at all sample positions. Global stress relaxations in piezoelectric ceramics usually happen on the timescale of seconds[148-150]. A local stress relaxation which is different at different sample positions is nevertheless still possible, but this triggers domain processes[151]. Mechanical stress and domain wall movement are closely related in piezoelectric materials.

Our material is a soft piezoelectric, so domain wall movement will occur even at low voltages and in unipolar loading[136]. Comparing our relaxation timescales to other domain studies found in literature[77,93,106-108], we can see that often domain processes occur in similar timescales. They are referred to as fast domain relaxation processes in contrast to the slow relaxations that are of interest when studying

for example the retention behavior of ferroelectric random access memories (Fe-RAMs).

7.6.2.3 Fitting of the data

We will now try to explain the measured relaxations by the domain switching models summarized in chapter 2.5. For simplicity, we will assume that our PZT ceramic only consists of one tetragonal phase, even though a rhombohedral fraction can be seen in the phase analysis (see figure 2.14).

Different possible models can explain the two relaxations which can be seen in the measurements in the active area of the actuator. Typical domain processes in a tetragonal piezoelectric material can be either 180° or 90° switching. A simple sketch of a unit cell visualizing the two possible processes is given in figure 7.41.

In principle, 90° domain steps and 180° domains steps can be measured using X-ray diffraction. 180° domain steps yield a change in intensity due to the imaginary part of the atomic formfactor[152] changing the structure factor. This is only valid when studying single domains or domains with a preferred orientation. In contrast, 90° domain steps can be seen well, as the change of the unit cell dimensions shown in figure 7.41 (b) leads to a tilting of (101) planes by approximately 1 degree (calculated with the lattice parameters of our ceramic). This is much larger than the usual rocking width of our peaks. Studying the (100)/(001) peak would give us more detailed results as we would also see a change in the 2θ value, but the intensities were too low to obtain good statistics.

Only single grains can be studied with a focused X-ray beam. Nevertheless the number of domains is much higher. Measurement effects will reflect changes in the average orientation, lattice constant etc. of all domains or in a fraction of the domains.
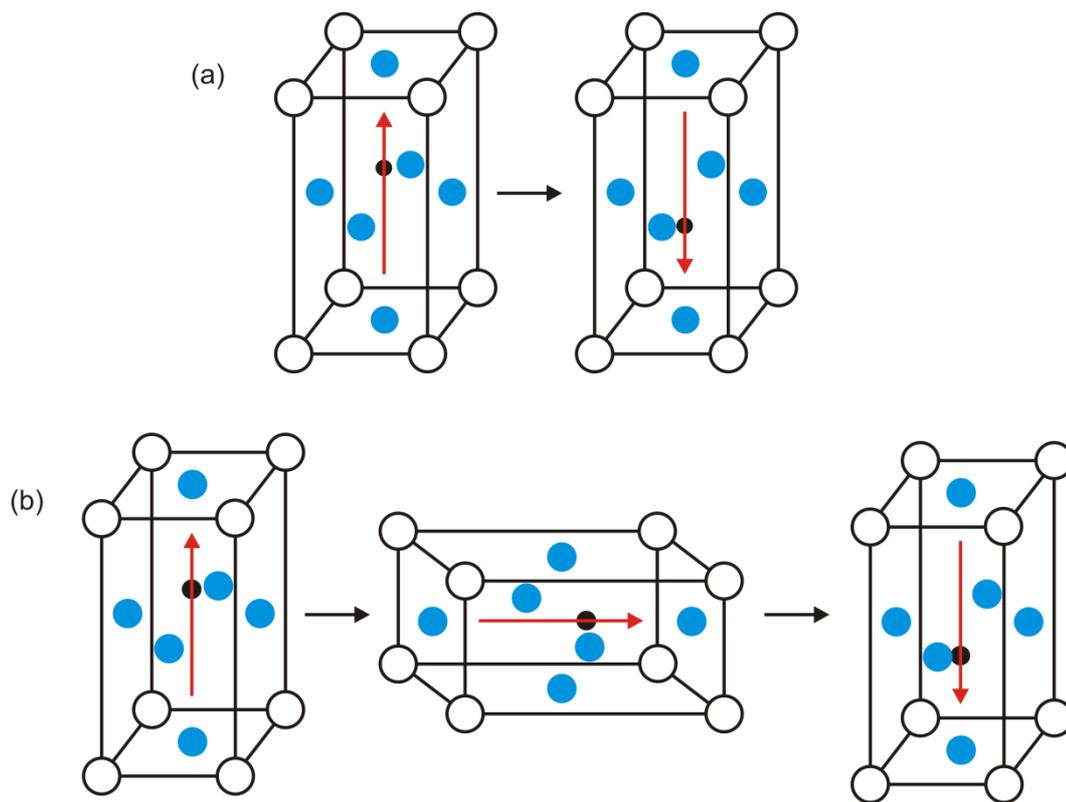
Figure 7.41: Visualization of possible domain processes. (a) 180° switching, in this case the total unit cell dimensions do not change, the length remains the same und lattice planes also do not change their orientations. (b) Two 90° switchings, here, the unit cell dimensions and the lattice plane angles change during the experiment. 90° domain steps are the reason for the typical strain-electrical field butterfly loops (figure 2.5).

As summarized in chapter 2.5.1, domain wall movement is often described with a stretched exponential function of the Kohlrausch-Watts-Williams Type[91]. Often, literature experiments on domain switching kinetics are in the millisecond to microsecond regime,[77,106-108,153,154] which we also study in our work.

We can now try to model our results on the basis of the Kohlrausch-Watts-Williams[91] equation (equation 2.10) or also on the basis of the two alternative models, the Curie-von Schweidler[101,102] relationship (equation 2.11) or a logarithmic decay function[155] (equation 2.12). The intrinsic deformation of the unit cell,

which happens instantaneously (figure 7.40), will not be considered here. Fitting will only be done on the relaxations after switching on or off the actuator.

At first, we took a representative dataset and tried to fit the data with each of the three mentioned models. In our following considerations all possible types of curves will be studied, either the time-dependent fits of the angle positions, intensities and the full width at half maximum (FWHM) or also the time-dependent intensities at single Q points. All these curves show similar features and can be treated as a whole. In figure 7.42, two representative curves with the corresponding fits of a sum of two functions of every type can be seen.

Although the curves are of course only examples for a large dataset it is quite obvious that the stretched exponential function provides by far the best fit for the results, fitting errors are within a reasonable range. The theoretical description of domain processes reproduces our data well. At ANKA, where we studied many grains collectively, they show different changes in intensity (also with a different sign and different relaxation times) and will average out.
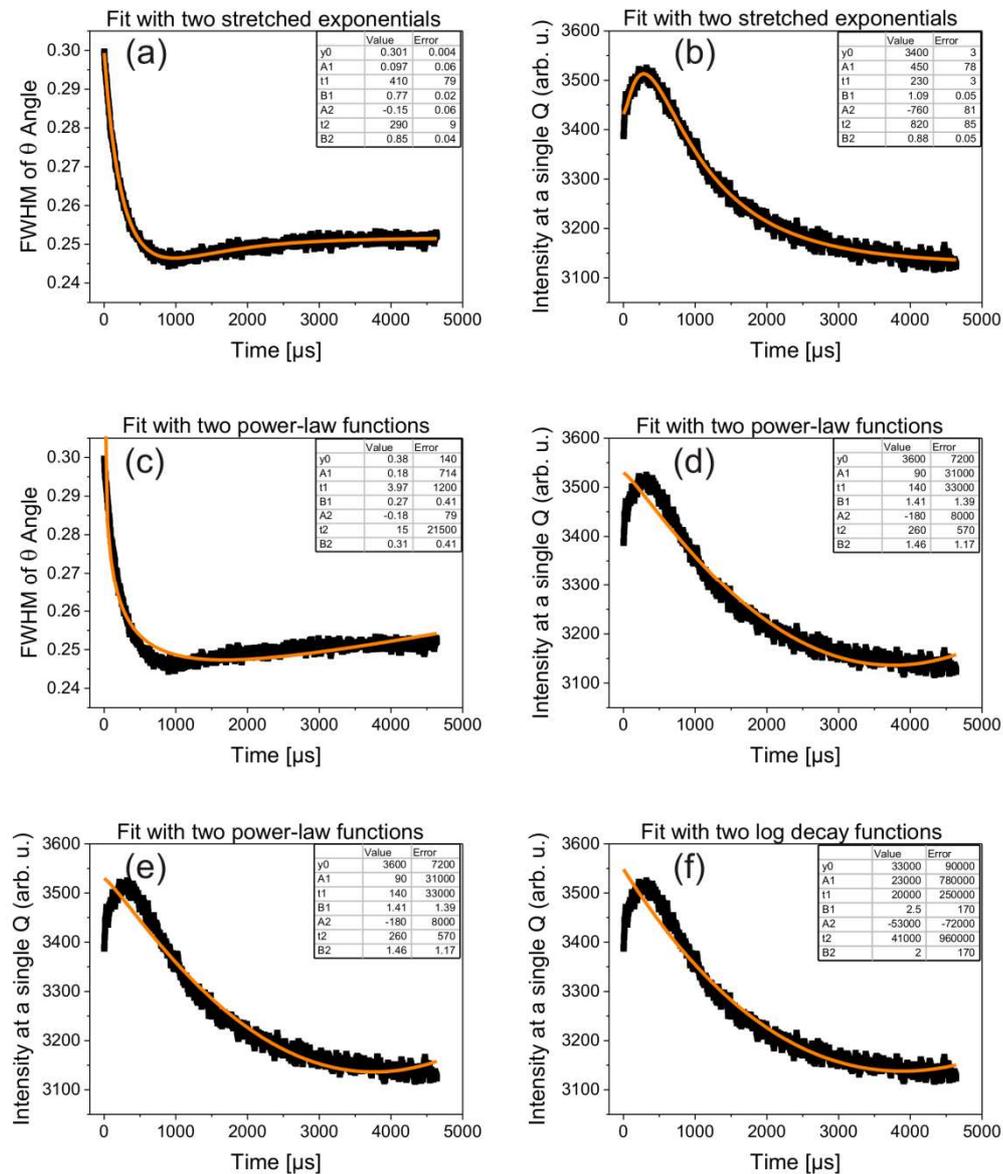
Figure 7.42: Different fits of example datasets from mesh 4 with the models available in literature. 7 fit parameters were used: $t_{1,2}$ as relaxation times, $B_{1,2}$ as exponents and $A_{1,2}$ as amplitudes for both processes. y_0 describes the y value at infinite time. (a,b) Fit with a sum of two stretched exponentials, (c,d) Fit with a sum of two power law functions, (e,f) Fit with two logarithmic decay functions. As can be clearly seen, the stretched exponential provides the best fit in both cases. Also, the fitting errors are lower.

We can now move on to a more detailed examination of our data starting with the meshes taken in the centre area of the actuator. A reasonable approach would be to describe the data at single Q points and fitted angles as a sum of two stretched exponential functions with a constant background. If the two processes both start at the same time t=0 (the time when the electrical field is fully applied) and have independent relaxation times and amplitudes, we can use an equation of the form:

$$I(t) = A_1 \cdot \left(1 - e^{\left(-\frac{t}{\tau_1} \right)^{\beta_1}} \right) + A_2 \cdot \left(1 - e^{\left(-\frac{t}{\tau_2} \right)^{\beta_2}} \right) + I_0 \qquad \textbf{(7.3)}$$

At this point, we have to recall the physical origin of our fitting parameters. The sum of both functions is the intensity I of the signal against time. At t=0, the diffracted intensity of the X-ray signal is I_0, which represents the intensities (structure factors) of all domains we are studying (including background). The physical meaning of the two stretching exponents β_1 and β_2, the dimensionality of the growth process, was discussed in chapter 2.5.1. τ_1 and τ_2 are the relaxation times for the two processes. A_1 and A_2 are the amplitudes to describe the relative magnitude of the two relaxation steps. These amplitudes describe the fraction of the whole number of domains I_0 which switch. To explain this, figure 7.43 shows a schematic of our model with the two steps and the quantities used in equation 7.3.

At the beginning, in the unpoled state, a certain number of domains in diffraction condition are present in the material. In a first step, an unknown number of these domains will switch by 90°; the resulting change in intensity is described by a stretched exponential function with the intensity change I(1). The second 90° step is also described by a stretched exponential function with different parameters and the intensity change I(2). In this case, the two amplitudes to describe the steps must have different signs, as the orientation change in the first step will switch the domains out of the diffraction conditions, while in the second step they will

switch back into the diffraction condition again. This is only valid if the peak is described by a simple form like the Gaussian function.
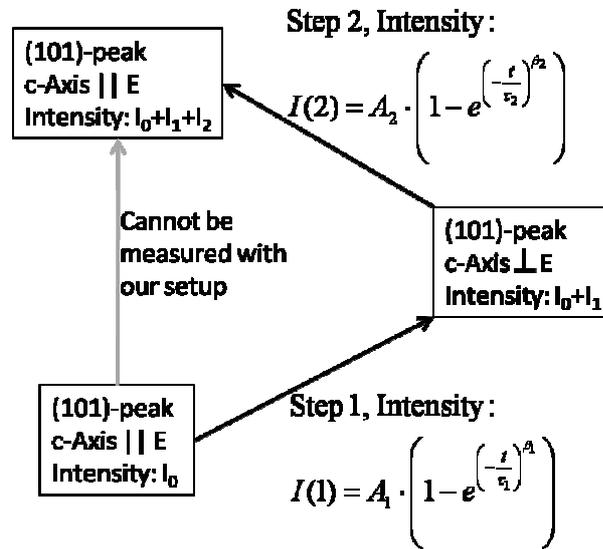
Figure 7.43: Schematic showing the two steps we assume and the quantities involved in our model. At first, a number of domains with a total intensity I_0 are present, for example with their c-axis parallel to c. In a first step, the c-axis will change its orientation by 90° and is now oriented perpendicular to E. This step can be described with the three variables A_1, τ_1 and β_1. The second 90° step switches the c-axis back to the orientation parallel to E and will occur with different time constants.

To model the expected results, we took a 3-dimensional Gaussian peak (shown in figure 7.44) and shifted it into the θ direction using function (7.4). In our case, the peak position moved from position (1) to position (2) and the intensities on the points (a) and (b) were studied as a function of time. The relaxation times were chosen as $\tau_1=400$ and $\tau_2=800$ μs and the amplitudes as $A_1=200$ and $A_2=-150$ (values similar to the values we often obtained for our data). For simplicity reasons, the stretching exponents were chosen as 1.
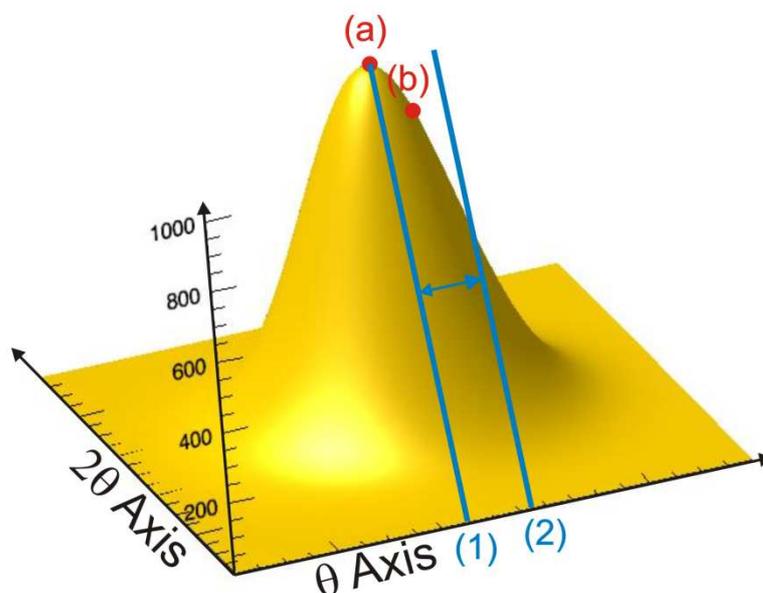
Figure 7.44: Simple model of a 3D Gaussian peak to explain the different curve shapes we obtained for the different positions on the peak. As an example, the peak has been shifted from position (1) to position (2) using a sum of two stretched exponential functions and the intensities at the points (a) and (b) were studied.

If the time-dependent intensities which we obtain for the two points are compared, interesting differences can be seen. The reason is simple: while the intensity at the peak position only shows the two relaxations from the input function, points close to the peak can show some additional oscillations. This is the case if the shift of the peak maximum is larger than the distance of the point from the peak. In this case the position of our Q point with respect to the maximum changes from the right shoulder of the peak to the left shoulder and back to the right shoulder. This appears as additional relaxation in the intensity. For θ, we expect a shift of around $1°$ due to the $90°$ domain step. As the whole range we study in Q is much smaller than $1°$ (usually only around $0.1°$), we would expect to see additional relaxations in θ directions compared to 2θ (of course only in the one direction where the peak shift happens).
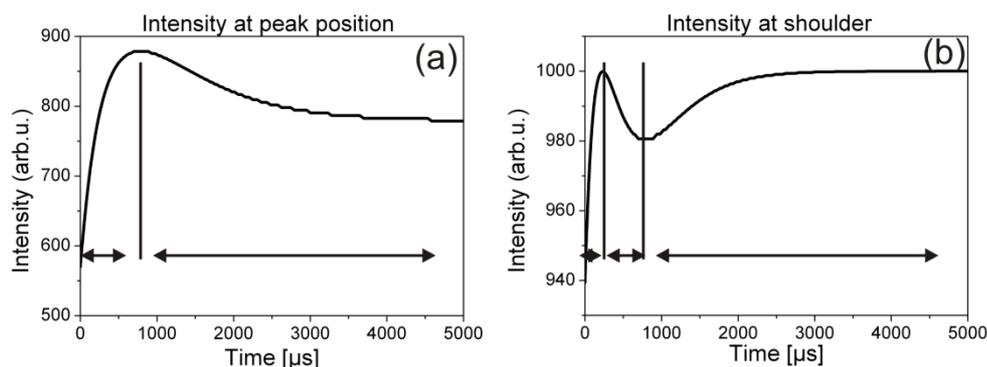
Figure 7.45: Example for the different curve shapes we can get when shifting the peak from figure 7.44. For (a), the intensity at the peak maximum, we only see the two relaxations. In (b), the fact that the peak shifts by a larger amount than the distance of the point to the peak leads to an additional intensity relaxation.

As shown in figure 7.24, we obtain a peak with different facets in our experiments. The monochromator leads to stripes of the beam on the sample, which results in a complicated peak shape. In θ and 2θ, the shift of the peak maximum due to the piezoelectric effect is smaller than the distance between two Q points, but the additional ferroelectric shift will happen in θ. The complicated peak shape which also changes when the peak is shifted can nevertheless explain the different curve shapes for different Q points on the mesh (see e.g. figure 7.31 (a) and (b)). Unfortunately, the setup problems will not allow us an exact consideration of the whole data at this point; no systematic has been found studying the single Q results. When talking about our results in the rest of this work, we always regard effects of most of the data, but for some points the whole shape cannot be explained.

When treating the data, we studied both the on- and off-switching of the electrical field. Ideally, on- and off-switching should occur with the same relaxation times and intensities. For our data, the parameters had to be chosen as independent, as the quality of our data was not good enough to find really similar response for both switchings at one Q point.

As already shown in figure 7.42, this mathematical description fits many curves very well. A large number of curves have been fitted and altogether, almost always the data is reproduced very well. Some more examples for successful data fitting with two stretched exponential functions are shown in figure 7.46.
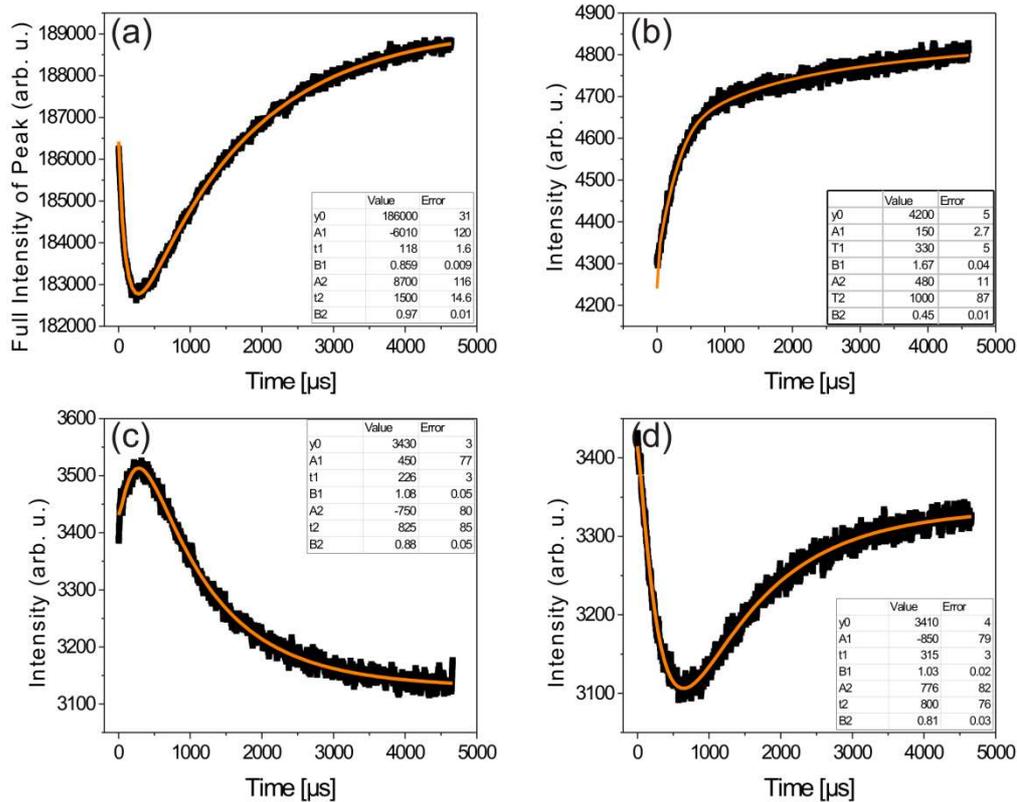
Figure 7.46: Examples for fitting of relaxation curves with a sum of two stretched exponential functions (equation 7.1). Almost all curves can be reproduced well with this assumption.

Nevertheless many free parameters are available in the equation, which often leads to fitting results that are implausible, namely very high exponents (higher than 2 meaning two-dimensional growth) or amplitudes higher than the original intensity. We thus have to find a system to simplify the data treatment in a way that the fitting procedure is somehow forced to give reasonable results without too

many constraints. If we take a look at the full set of fitting parameters, we see an accumulation of the results for certain values (figure 7.47).
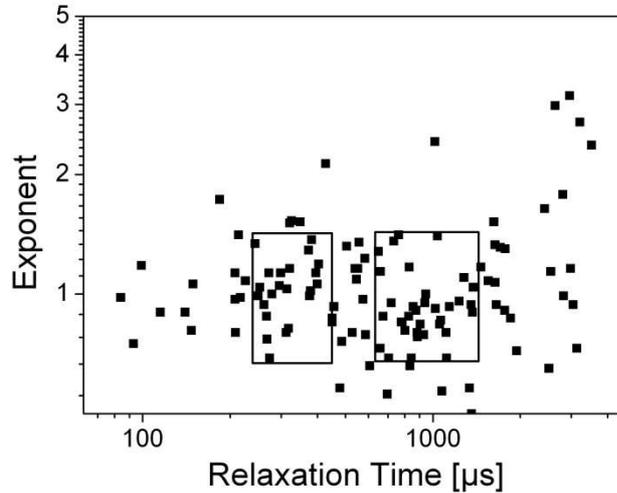
Figure 7.47: Graph showing the distribution of relaxation times and exponents for both relaxations and a set of fits performed at several meshes. A accumulation of data can be seen at stretching exponents close to 1 and at relaxation times around 300-400 and 700-1000 µs.

The dataset shows that for many fitted curves, the stretching exponents lie close to 1 and the relaxation times are around to 300-400 and 700-1000 µs. The stretching exponent has an interesting physical meaning because it describes the nature of the process we are investigating, in our case the dimensionality of the domain structure. The physical background of the relaxation time is not so significant. We thus will now fix the time constants, because we expect to get more information keeping the stretching exponents as free fit parameters. This is a simplification to try to find a systematic in the data. For our next fitting run, the relaxation times were fixed to τ_1=400 µs and τ_2=800 µs:

$$I(t) = A_1 \cdot \left(1 - e^{\left(- \frac{t}{400\,\mu s} \right)^{\beta_1}} \right) + A_2 \cdot \left(1 - e^{\left(- \frac{t}{800\,\mu s} \right)^{\beta_2}} \right) + I_0 \qquad (7.4)$$

151

Other relaxation times were also tried and no significant improvement of the fits was found, but some of them also give reasonable results. If we now fit the full data of mesh 1 (121 points, on- and off-switching processes) with these new constraints, we still get very reliable and plausible results for almost all of the curves. As an example, four of them can be seen in figure 7.48.
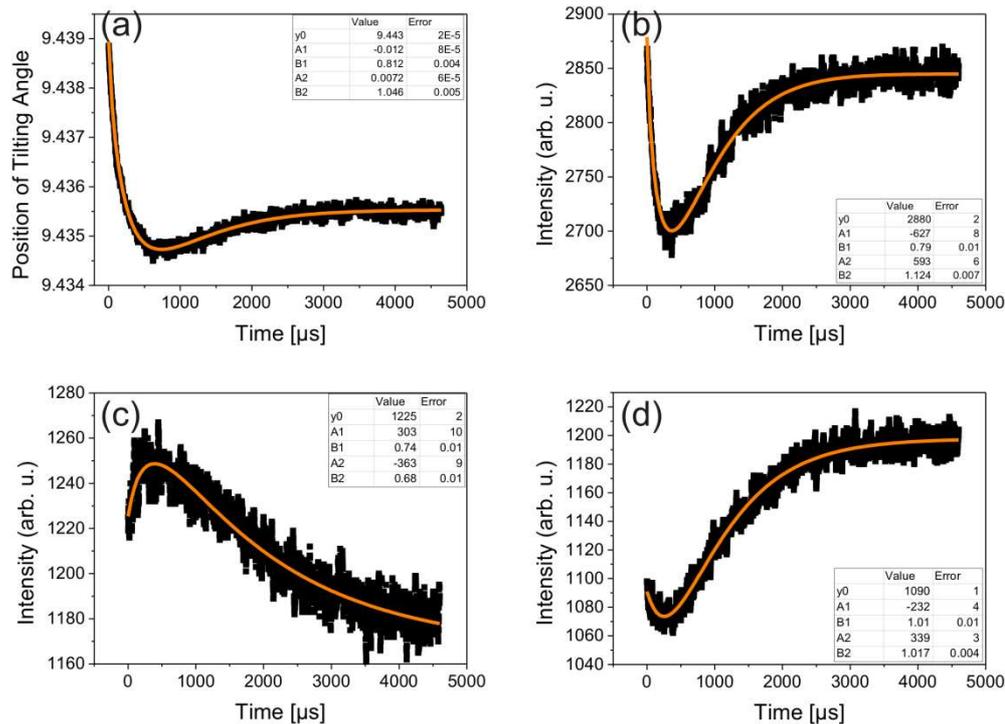
Figure 7.48: Four example curves for fitting the relaxations with two stretched exponential functions and fixed time constants of 400 μs and 800 μs. Curve shapes can be reproduced very well.

With this function, we can now fit a larger amount of data and try to find a systematic behind our results. To do so, we took most of the curves of the 6 meshes in the centre of the sample (except the curves with very low intensity at the peak edges) and fitted both relaxations with equation 7.4 and fixed times for τ_1 and τ_2. When looking at the amplitudes, it does not make much sense to consider the absolute values, as they only represent total changes in intensity, which are different

for each point on the mesh. More meaningful could be a fixed ratio of the amplitudes which could help in the interpretation of the data.

The first insight in the processes and the reliability of our model can be given by a total statistics of all the fitting parameters we measured in our experiments. For the six meshes we are considering at the moment, we can plot a total histogram-like statistics of the amplitude ratio A_2/A_1 (figure 7.49) and the stretching exponents $\beta_{1/2}$ (figure 7.50). We only used the absolute values. Normally, the curves should show two relaxations in opposite direction, so the amplitudes should have different signs. This is the case for more than 80% of the points, but some show differences due to the stability problems discussed before.
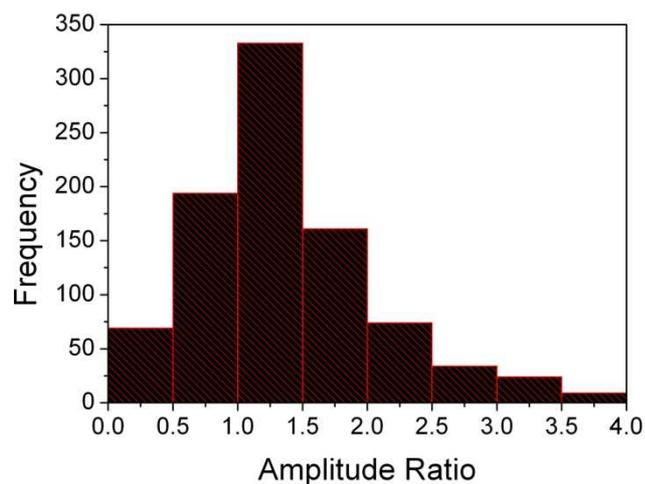
Figure 7.49: Distribution of the amplitude ratio for all the fits with two stretched exponential functions and fixed relaxation times. Often, the amplitudes for both processes are relatively similar.
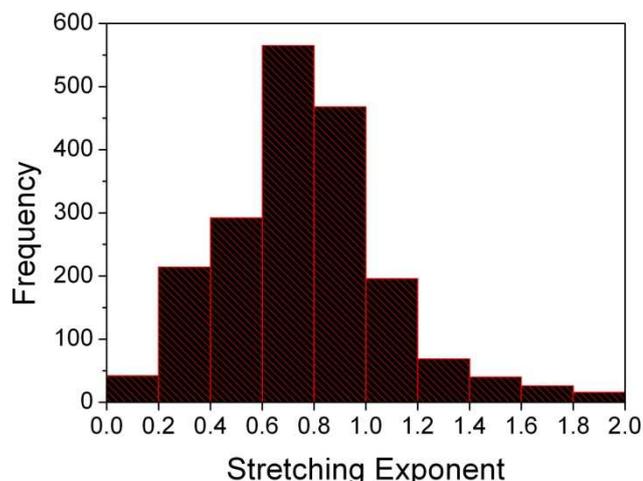
Figure 7.50: Values of all stretching exponents for all the fits performed at the selected meshes with a sum of two stretched exponential functions and fixed times. The stretching exponents are usually between 0.6 and 1.

We can summarize a few trends from the fitting results. First, the amplitudes of both processes are often similar or the second switching is a little stronger, and the stretching exponent is often slightly below one. A stretching exponent lower than one would describe almost one-dimensional growth of domain walls with few fluctuations in the opposite direction of the growth[99]. Taking the explanation of Lupascu et al.[100], a stretching exponent close to one would also mean that the domain structure in the material is highly ordered.

In the model we used so far we assume that both switching processes are independent. During this work, we also tried different models with the two processes depending on each other. As an example, equation 7.5 describes a model where the amplitude of the second process adds up as a sum of two intensities: one fraction of domains already present at t=0 and a second fraction that has completed the first switching step (see figure 7.43). After fitting the data with this model it turned out that equation 7.4. describes our data better, probably due to the partially bad data quality.

$$I(t) = A_1 \cdot \left(1 - e^{\left(-\frac{t}{400\,\mu s}\right)^{\beta_1}}\right) + \left[A_2 - A_1 \cdot \left(1 - e^{\left(-\frac{t}{400\,\mu s}\right)^{\beta_1}}\right)\right]$$
$$\cdot \left(1 - e^{\left(-\frac{t}{800\,\mu s}\right)^{\beta_2}}\right) + I_0 \tag{7.5}$$

Several other models were tried during this work. As a summary, they do not describe the data as well as equation 7.4 does, which may also be due to the fact that the fewest assumptions are made in this model. To conclude, our time-dependent data shows two domain relaxation processes, which have comparable amplitudes and start at t=0. This domain relaxations lead to a shift of the Bragg peak and give rise to changes we can see in the angle positions as well as the intensities on a single Q point and the integral intensity.

If we recall the results from the first ESRF beamtime with the split actuator, we only saw one slow relaxation process. The split actuator is in a pre-stressed state, which is a big difference to the baby actuator experiments. This pre-stress could trigger different processes in the material.

Before polarization, domains are randomly aligned in the material. The reason for the many domains that are formed is the minimization of the depolarizing field in the material. There is a comparable number of domains polarized in each of the six possible directions. If a mechanical pre-stress is applied to a piezoelectric material, domains are forced to align perpendicular to the direction of the stress[24,156,157] (figure 7.51). This usually happens by a 90° domain step[158]. If an electrical field is now applied in the same direction than the mechanical pre-stress, there is only one 90° domain step remaining. This describes the initial state for the split actuator. It can be found in the literature that a pre-stress increases both the dielectric permittivity[159] and the total macroscopic strain of the actuator. The total

strain is larger because many domains are oriented perpendicular to the electrical field and so the relative expansion when the field is applied is higher. There exists a maximum strain that can be reached at certain pre-stress levels[25-29,160,161] (figure 7.52), which is also one of the reasons why pre-stresses are applied in the application. This is only valid if the actuator is driven in unipolar mode.
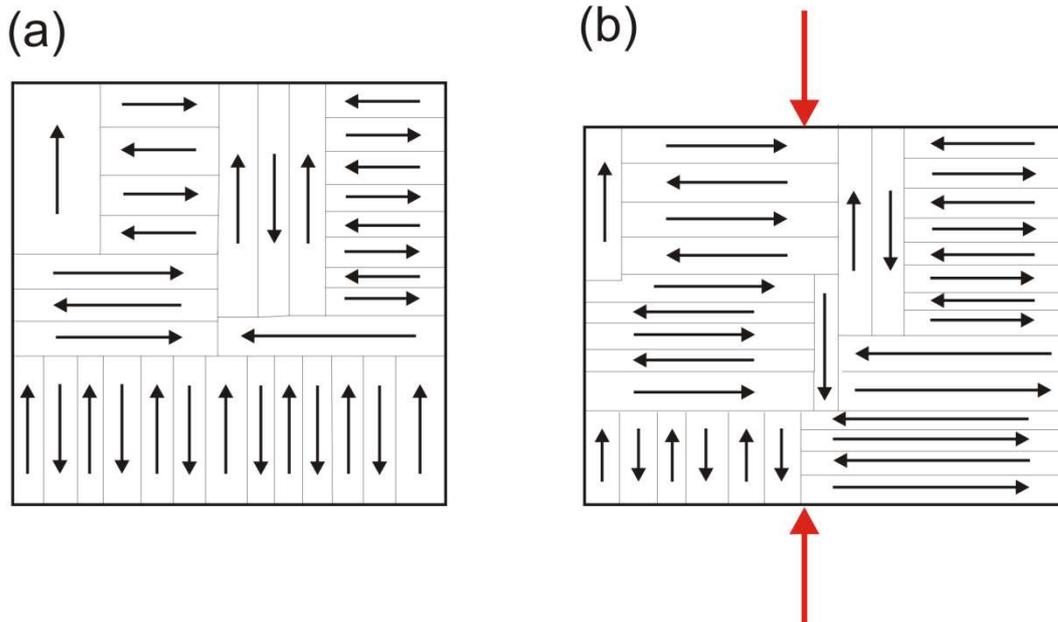
Figure 7.51: Effect of mechanical pre-stress on the domain configuration in a piezoelectric material. Domains will avoid the external stress by orienting perpendicular to it. This can explain why we only saw one relaxation when working with the pre-stressed split actuator (b), while we measured two relaxation processes when measuring the response of the baby actuator (a).
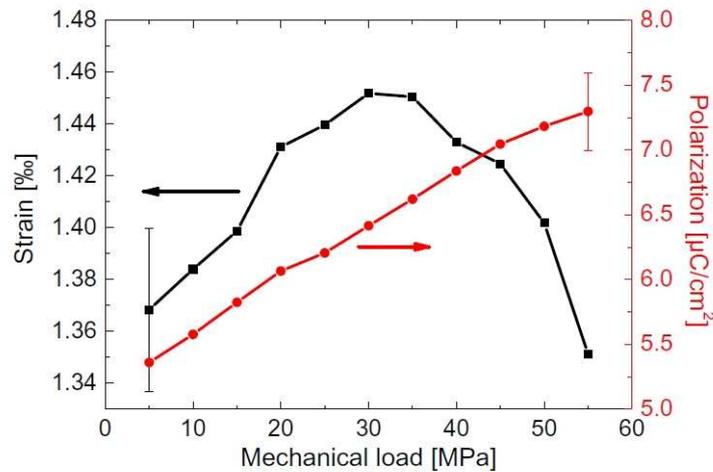
Figure 7.52: Influence of mechanical pre-stress on the strain of a piezoelectric multi-layer actuator[29]. At a certain stress, a maximum strain level exists due to the orientation of 90° domains induced by the mechanical stress.

We could thus conclude that we see only one 90° domain step in the split actuator, maybe the second process exists, but has a much lower amplitude so that the relaxation effect is hidden behind the vibrations we see (figure 7.18). If we consider two 90° domains steps, the second step should depend on the first one. It is known from the literature that the two 90° steps do not have the same switching times[30], as the activation energy for these processes is different[11] due to dielectric energy generated by the polarization opposed to the switched domain. This would explain why the processes happen on different timescales. In the same studies it was pointed out that 180° domain wall motion is much slower (it would anyhow be very difficult to measure when studying multiple domains with our setup), so 180° domain steps can be excluded. There is also literature data where each 180° domain step is assumed to occur via two 90° domain steps[162].

As stated in the domain theory chapter (2.5.1), the stretching exponent describes the mechanism of domain growth. This mechanism might depend on the parameters of the experiment, so we can try to compare the data summarized in figure 7.49 and figure 7.50 for different parameters. Altogether, there are the results of

six meshes plotted in these diagrams. For the meshes 1,2, 4 and 5 we measured twice the same grain, only with different voltages applied. If there is a difference in the mechanisms, we should see it by comparing the distribution of stretching exponents for the measurements taken at a high voltage of 160 V (figure 7.53) and a low voltage of 80 V (figure 7.54). The graphs show a tendency that the lower voltage will also lead to lower stretching exponents (0.78 median value for high voltages compared to 0.71 for low voltages). This can be easily understood, as a lower voltage will lead to a lower driving force on the domain walls and growth fluctuations lowering the stretching exponent are more reasonable.
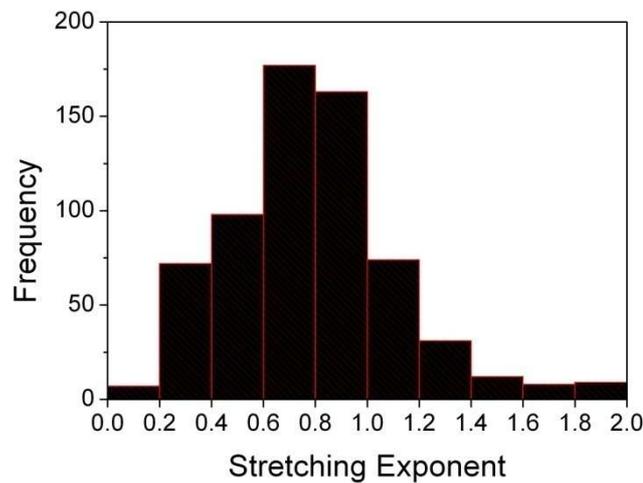
Figure 7.53: Distribution of stretching exponents for the experiments done at 160 V. Most of the stretching exponents are between 0.6 and 1.
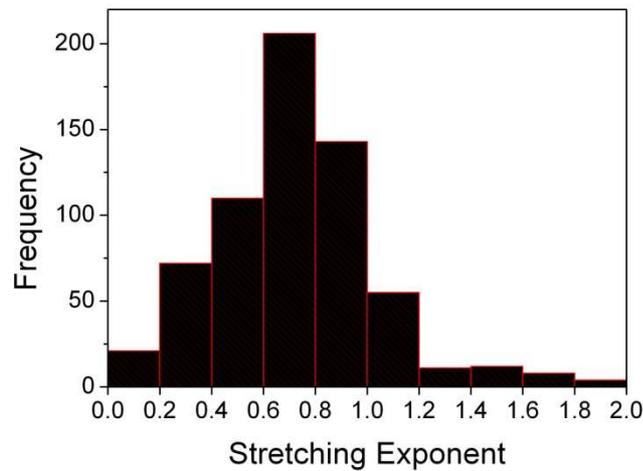
Figure 7.54: Distribution of stretching exponents for the experiments done with lower voltage (80 V). The exponent value lies mostly between 0.6 and 0.8, the probabilities are shifted to lower values.

We can also study whether there are differences in the exponent values for both the faster and slower relaxation or for the on- and off-switching process. For the switching-on and -off, only small differences can be found (on: 0.75, off: 0.73), the effect is not significant. Regarding the first (faster) and the second (slower) relaxation we do indeed also see a difference, the stretching exponent is higher for the fast process (0.77 compared to 0.72). The faster process occurs with less growth fluctuations which also fits to our model.

Two meshes are still remaining and can now be considered. Mesh 3 was measured at the same grain than mesh 1 and 2, but with a shallower voltage ramp. As figure 7.55 shows, the stretching exponent is shifted to lower values compared to the distribution with a fast voltage ramp. This is reasonable, as lower ramps might also lead to lower driving forces for domain growth and thus to more growth fluctuations. The amplitude ratio distribution is in between the high voltage and the low-voltage experiments and will not be shown here, but also supports the trend.
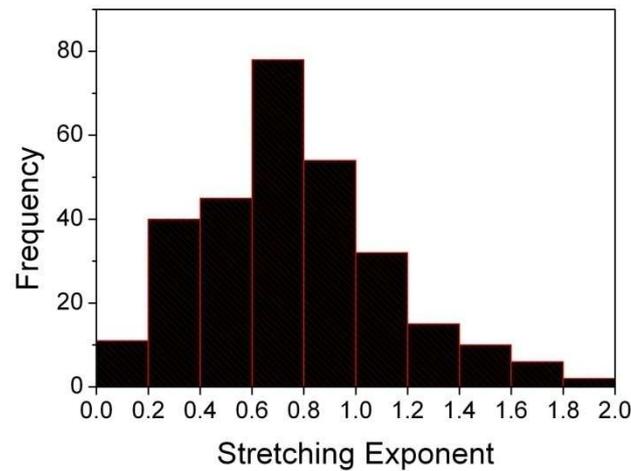
Figure 7.55: Distribution of stretching exponents for the mesh measured with shallower voltage ramp and 160 V. Compared to the fast ramp meshes, the exponent is shifted to lower values, which means more growth fluctuations.

Mesh 7 was measured close to the electrode edge with a voltage of 80 V. The special geometry at the electrode edge leads to high electrical fields and mechanical stresses which triggers fatigue in the actuator. At low voltages, we do not see differences compared to the centre of the actuator. The stretching exponents (median 0.81) are higher than in the centre of the actuator, which may be due to the effectively higher electrical field.

There are two remaining meshes which have to be discussed. First, one mesh was measured in the inactive area, where no strong electrical field can be found. In contrast to the results in the area of homogeneous electrical field, only one relaxation process can be seen here. If we try to describe it with a simple stretched exponential function assuming also domain processes, we get mostly relaxation times in the range of 1000-5000 μs and stretching exponents slightly above one. The curves (figure 7.36) show that the total shifts are relatively weak and especially no very strong relaxation can be seen.

As we are considering the inactive area of the actuator, we expect no strong electrical field. More reasonable would be a macroscopic relaxation of the whole ac-

tuator leading to small shifts in the inactive area. This effect is probably too weak to be measured in the active area, where stronger changes are triggered by the electrical field.

The curves for high voltages and the grain position close to the electrode edge show a different shape (figure 7.33 and figure 7.34). We can see a very strong response for both of the angles and the intensities at single Q points. If we try to describe the results with the model for domain wall movement, we need three exponential functions to describe most the data. If we would assume that domain processes are the origin of the relaxations, we can again try to get a distribution of stretching exponents to describe the mechanism of switching (figure 7.56). We can see that most of the stretching exponents are higher than one, which is not expected for domain wall movement as domains usually grow only one-dimensional. If we take the simple model that is behind that description, we can still think that the structural effect triggering this relaxation should have a dimensionality of 1-2.
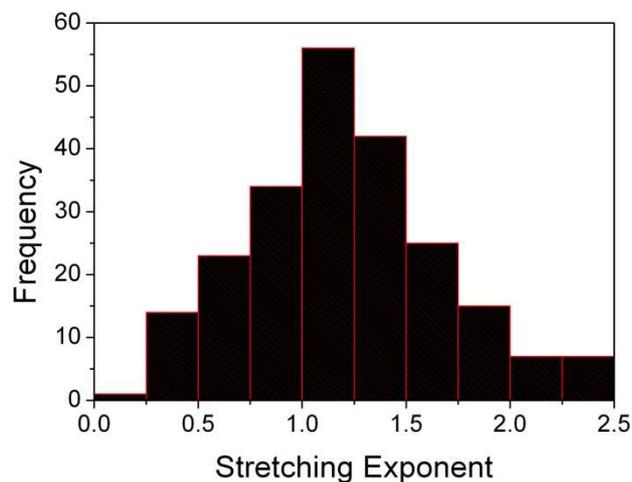
Figure 7.56: Distribution of stretching exponents for fits of mesh 6 with three stretched exponential functions. Most of the exponents are higher than one, which suggests that no domain process is the origin of the relaxations.

If domain relaxations are not the origin of the strong relaxations (which for many curves look more like vibrations) we have to consider what else might be the reason for this response. In contrast to the other meshes, we see a contraction of the unit cell as first response to the excitation, which later relaxes and turns to an expansion of the unit cell reflecting the behaviour of the full device.

The mechanical stresses close to the electrode edge when an electrical field is applied are much higher than in the centre area[32,163]. The strong response to the voltage was not seen in any other mesh and also disappears at lower voltages (figure 7.33 and figure 7.35), so we can assume that the mechanical stress is the origin. Stress can trigger several kinds of relaxation, first relaxation of the stress itself, but also of defects in the material such as dislocations[164] or point defects[165], which are usually studied with mechanical spectroscopy. As the theory for these mechanisms is of high complexity and our results only give a "macroscopic" view on the response of whole domains or grains, we can only try to explain the response qualitatively. For a quantitative description, different methods would be necessary, which are on the other hand usually not position-sensitive enough to study only the response at single positions of the actuator.

For a qualitative description we can try to interpret the curve of θ-2θ plotted against time (figure 7.33). The first instantaneous response of the material in this region is a contraction of the unit cell, although the effect is very small. This is different than at all other sample positions, where we can see an expansion. A compression of the unit cell can generally be triggered by compressive stresses. If we recall the literature, experiments[166] and simulations[167,168] show strong compressive stresses close to the electrode edge. These compressive stresses can trigger dislocation relaxations which also lead to a relaxation of this stress. If this happens faster than the actuator can follow, the dislocations can itself now lead to tensile stresses which are relaxed again and can explain the vibration-like response we see in the curves. After a while, the stresses are relaxed and the unit

cells close to the electrode edge follow the response of the whole actuator and show an expansion. Defect relaxations can also play a role when considering fatigue in piezoelectric materials, but a more detailed study would be necessary to verify this hypothesis.

To conclude, most our results can be described well using a model of two 90° domains steps. Under special boundary conditions, different responses can be found. The method works reproducibly and different samples can be studied in time-resolution and with different beam sizes. In the future, the goal could be to repeat and expand the measurements with a more stable setup, as we for example could not study the temperature-dependence and the influence of fatigue, which would both be of large interest for science and application. Domain processes should indeed depend on the temperature and also change with the fatigue state[100,169].

Nevertheless, our results can already give an interesting insight on the dynamic response of the actuator and help to improve the fundamental understanding and can also be used for simulations. New and more sophisticated X-ray methods will open up further possibilities to study piezo- and ferroelectric materials. With our setup, devices very close to the application condition can be studied under different boundary conditions.

8   Conclusions and Outlook

In this work, we have studied the time-dependent response of piezoelectric actuators when exposed to an electrical field. As major part of the work, we developed a new setup where we could perform experiments on the original device, which was not done before in literature. With the respective electronics and software, we achieved a time-resolution of 1 µs. The conditions were chosen as close as possible to the application, only minor changes in the geometry were necessary. A split actuator was developed to eliminate vibrations in the system. For later experiments, a smaller baby actuator was used to ensure maximum mechanical stability of the sample position.

At ANKA, the response of large areas on the actuator was studied. The external electrical field gave rise to shifts of the Bragg peaks, as the unit cell changes its shape when the actuator is exposed to the field. This happens instantaneously after the field is applied. No further strong time-dependent relaxation response was found. This could probably be addressed to the large number of domains which were studied, where small signal effects average out.

At ESRF, experiments with a pre-stressed split actuator and a free standing baby actuator were done. The response of single grains was studied, in both cases strong time-dependent relaxations can be seen. When a pre-stress was applied, only one domain step could be found, while two domain steps could be seen in the non-pre-stressed baby actuator. A possible explanation for this was the alignment of domains due to the external mechanical stress. Domain growth was almost one-dimensional. At lower voltages and shallower voltage ramps, more growth fluctuations occur. In the inactive area, no strong relaxation behavior was found. Close to the electrode edges, high mechanical stresses could probably trigger defect relaxations which appear as strong oscillations in the diffraction signal. At lower

voltages, the threshold stress for these relaxations was not exceeded and the effect vanishes.

In addition to the time-resolved experiments, the mechanical properties of AgPd thin films used as electrode material were studied using synchrotron-based micro-tensile tests. We found a decrease of flow stresses with increasing temperature. Nevertheless, application conditions should only yield elastic deformation in the films. No size effect was found when studying two different film thicknesses of 2 and 4 μm.

With our new time-resolved diffraction setup, there are many more experiments one could think of. In the future, the goal of the experiments should be an exact study of only one grain with maximum stability of the setup and beamline, so that the pure effect of single grains or, with smaller beam sizes, even domains can be studied. Domain processes should depend on temperature[87,170] and fatigue state[100], as 90° domain wall movement is more affected by fatigue than 180° switching[171]. In further experiments, one could study this and also see whether changes apply to all sample positions or do only occur in the active area of the sample. Knowing the exact processes which are responsible for fatigue in piezoelectric devices can improve the future construction of these devices and fatigue resistance. Different materials can be studied and the optimal composition with least fatigue can be selected. If the whole cycling of the sample is done in a synchrotron, also change of the relaxation response with increasing cycle number can be studied. Also, simulations which are at the moment done quasi-static can be changed in a way that the dynamic response of the domains can be taken into account. Another possibility would for example be the time-dependent change of residual stresses at different sample positions, which can also be measured with our setup.

A wide field of interesting experiments with a similar setup could arise from new methods which are currently developed in the field of X-ray diffraction. With new

free electron laser X-ray sources[172,173] like the X-FEL[174], very high intensities and brilliances can be reached in very short times. By pump-probe experiments[175], the response of special samples can already be studied in a single shot. Experiments using free electron lasers on piezoelectric materials could give insight in the very fast processes in the material[176]; with coherent X-ray beams one could get much information in short times[177]. Due to the special requirements of these experiments they could however only be done on model systems. Short-time experiments could extent the knowledge on fast relaxation processes in piezoelectric material.

Gated detector systems could be used and can be synchronized to the synchrotron bunches, also with one- or two-dimensional detectors like the Pilatus[178]. The readout times are nevertheless relatively slow and restrict the measurement speed. With our samples, extremely short counting times cannot be used, because the total diffracted intensity from the sample is too low. The methods are mainly restricted to model systems like thin films, where it was already successfully used to study the intrinsic piezoelectric effect[82].

Other possibilities arise from high energy beamlines, where larger samples can be studied in transmission geometry. When working with thicker samples, studies on single grains get more difficult as now a larger amount of material is illuminated. On the other hand, the geometry gets simpler when working in transmission as the sample can be prepared to study lattice planes in any desired field direction.

The method developed in this work was an approach to study a real device during operation and in operation conditions. Research on the field of piezoelectric materials will continue, increasing the understanding on dynamic processes in these materials and how they contribute to fatigue. With this knowledge from experiments and accompanying simulations, fatigue also under application conditions will be more predictable in the future.

9   Bibliography

1   J. B. Wachtman, *Ceramic Innovations in the 20th century* (The American Ceramic Society, Westerville, OH, 1999).

2   A. J. Moulson and J. M. Herbert, *Electroceramics* (Chapman and Hall, New York, 1990).

3   J. Curie and P. Curie, C. R. l'Academie. Sci. Paris **91,** 294 (1880).

4   G. H. Haertling, J. Am. Ceram. Soc. **82,** 797 (1999).

5   F. E. Neumann, "Vorlesungen über die theorie Elastizität fester Körper," (1885).

6   B. Jaffe, W. R. Cook, and H. Jaffe, *Piezoelectric ceramics*, Vol. 3 (Academic Press, London, New York, 1971).

7   A. Von Hippel, R. G. Breckenridge, F. G. Chesley, and L. Tisza, Industrial and Engineering Chemistry **38,** 1097 (1946).

8   E. C. Subbarao, M. C. McQuarrie, and W. R. Buessem, J. Appl. Phys. **28,** 1194 (1957).

9   R. M. McMeeking and C. M. Landis, Int. J. Eng. Sci. **40,** 1553 (2002).

10   H. Sahota, Continuum Mech. Thermodyn. **16,** 163 (2004).

11   S. C. Hwang, J. E. Huber, R. M. McMeeking, and N. A. Fleck, J. Appl. Phys. **84,** 1530 (1998).

12   M. Al Janaideh, C. Y. Su, and S. Rakheja, Smart Mater. Struct. **17,** 11 (2008).

13   B. Jaffe; *Vol. 2708244* (Jaffe, B., United States, 1955).

14   R. C. Rogan, N. Tamura, G. A. Swift, and E. Ustundag, Nat. Mater. **2,** 379 (2003).

15   S. E. Park and T. R. Shrout, J. Appl. Phys. **82,** 1804 (1997).

16   A. J. Bell, Appl. Phys. Lett. **76,** 109 (2000).

17   G. A. Rossetti, W. Zhang, and A. G. Khachaturyan, Appl. Phys. Lett. **88** (2006).

18   D. E. Cox, B. Noheda, G. Shirane, Y. Uesu, K. Fujishiro, and Y. Yamada, Appl. Phys. Lett. **79,** 400 (2001).

19   R. Guo, L. E. Cross, S. E. Park, B. Noheda, D. E. Cox, and G. Shirane, Phys. Rev. Lett. **84,** 5423 (2000).

20   B. Noheda, D. E. Cox, G. Shirane, J. A. Gonzalo, L. E. Cross, and S. E. Park, Appl. Phys. Lett. **74,** 2059 (1999).

21   B. Noheda, D. E. Cox, G. Shirane, R. Guo, B. Jones, and L. E. Cross, Phys. Rev. B **63** (2001).

22   B. Noheda, J. A. Gonzalo, L. E. Cross, R. Guo, S. E. Park, D. E. Cox, and G. Shirane, Phys. Rev. B **61,** 8687 (2000).

23   L. Bellaiche, A. Garcia, and D. Vanderbilt, Phys. Rev. Lett. **84,** 5427 (2000).

24   P. M. Chaplya and G. P. Carman, J. Appl. Phys. **90,** 5278 (2001).

25   C. S. Lynch, Acta Mat. **44,** 4137 (1996).

26   D. Zhou, M. Kamlah, and D. Munz, J. Eur. Ceram. Soc. **25,** 425 (2005).

27   D. N. Fang and C. Q. Li, J. Mater. Sci. **34,** 4001 (1999).

28   P. M. Chaplya, M. Mitrovic, G. P. Carman, and F. K. Straub, J. Appl. Phys. **100,** 13 (2006).

29   I. Kerkamm, P. Hiller, T. Granzow, and J. Rödel, Acta Mat. **57,** 77 (2009).

30   S. Pruvost, G. Sebald, L. Lebrun, D. Guyomar, and L. Seveyrat, Acta Mat. **56,** 215 (2008).

31   D. C. Lupascu and J. Rodel, Adv. Eng. Mat. **7,** 882 (2005).

32   C. A. Randall, A. Kelnberger, G. Y. Yang, R. E. Eitel, and T. R. Shrout, J. Electroceram. **14,** 177 (2005).

33   D. A. van den Ende, B. Bos, W. A. Groen, and L. M. J. G. Dortmans, J. Electroceram. **22,** 163 (2009).

34   S. Lucato, D. C. Lupascu, and J. Rodel, J. Eur. Ceram. Soc. **21,** 1425 (2001).
35   C. Schuh, T. Steinkopff, A. Wolff, and K. Lubitz, in *Smart Structures And Materials 2000 - Active Materials: Behavior And Mechanics*; *Vol. 3992* (2000), p. 165.
36   I.-H. Im, H.-S. Chung, D.-S. Paik, C.-Y. Park, J.-J. Park, and S.-G. Bae, J. Eur. Ceram. Soc. **20,** 1011 (2000).
37   W. Wersing, H. Wahl, and M. Schnoeller, Ferroelectrics **87,** 271 (1988).
38   A. Endriss, M. Hammer, M. J. Hoffmann, A. Kolleck, and G. A. Schneider, J. Eur. Ceram. Soc. **19,** 1229 (1999).
39   H. Kungl, R. Theissmann, M. Knapp, C. Baehtz, H. Fuess, S. Wagner, T. Fett, and M. J. Hoffmann, Acta Mat. **55,** 1849 (2007).
40   C. Verdier, D. C. Lupascu, and J. Rodel, J. Eur. Ceram. Soc. **23,** 1409 (2003).
41   Q. Y. Jiang, W. W. Cao, and L. E. Cross, J. Am. Ceram. Soc. **77,** 211 (1994).
42   A. L. Kholkin, E. L. Colla, A. K. Tagantsev, D. V. Taylor, and N. Setter, Appl. Phys. Lett. **68,** 2577 (1996).
43   H. Weitzing, G. A. Schneider, J. Steffens, M. Hammer, and M. J. Hoffmann, J. Eur. Ceram. Soc. **19,** 1333 (1999).
44   C. R. J. Salz, M. Hoffman, I. Westram, and J. Rodel, J. Am. Ceram. Soc. **88,** 1331 (2005).
45   J. L. Jones, C. R. J. Salz, and M. Hoffman, J. Am. Ceram. Soc. **88,** 2788 (2005).
46   D. C. Lupascu and U. Rabe, Phys. Rev. Lett. **89** (2002).
47   M. D. Hill, G. S. White, C. S. Hwang, and I. K. Lloyd, J. Am. Ceram. Soc. **79,** 1915 (1996).
48   D. C. Lupascu, E. Aulbach, and J. Rodel, J. Appl. Phys. **93,** 5551 (2003).
49   S. B. Desu, Phys. Stat. Sol. A **151,** 467 (1995).
50   G. Le Rhun, G. Poullain, R. Bouregba, and G. Leclerc, J. Eur. Ceram. Soc. **25,** 2281 (2005).
51   D. C. Lupascu and C. Verdier, J. Eur. Ceram. Soc. **24,** 1663 (2004).
52   A. K. Tagantsev, I. Stolichnov, E. L. Colla, and N. Setter, J. Appl. Phys. **90,** 1387 (2001).
53   D. J. Johnson, D. T. Amm, E. Grisvold, K. Sreenivas, G. Yi, and M. Sayer, in *Materials' Research Society Symposium Proceedings*, 1990, p. 289.
54   P. K. Larsen, G. J. M. Dormans, D. J. Taylor, and P. J. Vanveldhoven, J. Appl. Phys. **76,** 2405 (1994).
55   D. C. Lupascu, Y. A. Genenko, and N. Balke, J. Am. Ceram. Soc. **89,** 224 (2006).
56   Y. Zhang, I. S. Baturin, E. Aulbach, D. C. Lupascu, A. L. Kholkin, V. Y. Shur, and J. Rodel, Appl. Phys. Lett. **86** (2005).
57   M. Brazier, S. Mansour, and M. McElfresh, Appl. Phys. Lett. **74,** 4032 (1999).
58   Q. Y. Jiang, E. C. Subbarao, and L. E. Cross, J. Appl. Phys. **75,** 7433 (1994).
59   E. M. Alkoy, K. Uchiyama, T. Shiosaki, and S. Alkoy, J. Appl. Phys. **99** (2006).
60   G. Teowee, C. D. Baertlein, E. A. Kneer, J. M. Boulton, and D. R. Uhlmann, Integr. Ferroelectr. **7,** 149 (1995).
61   F. Yan, P. Bao, H. L. W. Chan, C. L. Choy, and Y. N. Wang, Thin Solid Films **406,** 282 (2002).
62   J. L. Jones, J. Electroceram. **19,** 67 (2007).
63   N. Menou, C. Muller, I. S. Baturin, D. K. Kuznetsov, V. Y. Shur, J. L. Hodeau, and T. Schneller, J. Phys.: Condens. Matter **17,** 7681 (2005).
64   D. H. Do, P. G. Evans, E. D. Isaacs, D. M. Kim, C. B. Eom, and E. M. Dufresne, Nat. Mater. **3,** 365 (2004).
65   D. A. Hall, A. Steuwer, B. Cherdhirunkorn, T. Mori, and P. J. Withers, J. Appl. Phys. **96,** 4245 (2004).
66   F. Yang, W. D. Fei, Z. M. Gao, and J. Q. Jiang, Surf. Coat. Tech. **202,** 121 (2007).
67   K. S. Lee, Y. K. Kim, S. Baik, J. Kim, and I. S. Jung, Appl. Phys. Lett. **79,** 2444 (2001).
68   R. Guillot, P. Fertey, N. K. Hansen, P. Alle, E. Elkaim, and C. Lecomte, Euro. Phys. J. B **42,** 373 (2004).
69   A. E. Glazounov, H. Kungl, J. T. Reszat, M. J. Hoffmann, A. Kolleck, G. A. Schneider, and T. Wroblewski, J. Am. Ceram. Soc. **84,** 2921 (2001).

70   S. Hackemann and W. Pfeiffer, J. Eur. Ceram. Soc. **23,** 141 (2003).

71   B. C. Larson and J. Z. Tischler, in *Time-Resolved Electron And X-Ray Diffraction*; *Vol. 2521* (1995), p. 208.

72   H. Jung and D. G. Gweon, Rev. Sci. Instrum. **71,** 1896 (2000).

73   M. H. Lente, A. Picinin, J. P. Rino, and J. A. Eiras, J. Appl. Phys. **95,** 2646 (2004).

74   B. S. Li, G. R. Li, Z. J. Xu, Q. R. Yin, and A. L. Ding, Integr. Ferroelectr. **75,** 91 (2005).

75   D. S. Fu, K. Suzuki, K. Kato, and H. Suzuki, Appl. Phys. Lett. **82,** 2130 (2003).

76   C. S. Ganpule, A. L. Roytburd, V. Nagarajan, B. K. Hill, S. B. Ogale, E. D. Williams, R. Ramesh, and J. F. Scott, Phys. Rev. B **65** (2002).

77   A. Gruverman, B. J. Rodriguez, C. Dehoff, J. D. Waldrep, A. I. Kingon, R. J. Nemanich, and J. S. Cross, Appl. Phys. Lett. **87,** 082902 (2005).

78   H. Fujisawa, M. Shimizu, and H. Niu, Jap. J. Appl. Phys. Part 1 **43,** 6571 (2004).

79   K. W. Lee and W. J. Lee, Jap. J. Appl. Phys. Part 1 **41,** 6718 (2002).

80   D. B. McWhan, G. Aeppli, J. P. Remeika, and S. Nelson, J. Phys. C: Solid State Phys. **18,** L307 (1985).

81   G. Zorn, Ferroelectrics **55,** 759 (1984).

82   A. Grigoriev, D. H. Do, D. M. Kim, C. B. Eom, B. Adams, E. M. Dufresne, and P. G. Evans, Phys. Rev. Lett. **96** (2006).

83   E. Zolotoyabko, J. P. Quintana, D. J. Towner, B. H. Hoerman, and B. W. Wessels, Ferroelectrics **290,** 115 (2003).

84   S. J. van Reeuwijk, A. Puig-Molina, O. Mathon, R. Tucoulou, and H. Graafsma, J. Appl. Phys. **94,** 6708 (2003).

85   J. E. Daniels, T. R. Finlayson, M. Davis, D. Damjanovic, A. J. Studer, M. Hoffman, and J. L. Jones, J. Appl. Phys. **101** (2007).

86   J. E. Daniels, T. R. Finlayson, A. J. Studer, M. Hoffman, and J. L. Jones, J. Appl. Phys. **101** (2007).

87   M. Avrami, J. Chem. Phys. **7,** 1103 (1939).

88   M. Avrami, J. Chem. Phys. **9,** 177 (1941).

89   M. Avrami, Journal of Chemical Physics|Journal of Chemical Physics**,** 212 (1940).

90   W. A. Johnson and R. F. Mehl, Trans. Am. Inst. Min. Metall. Eng. **135,** 416 (1939).

91   Y. Ishibashi and Y. Takagi, J. Phys. Soc. Jpn. **31,** 506 (1971).

92   Y. Ishibashi, Jap. J. Appl. Phys. **24S2,** 126 (1985).

93   B. H. Hoerman, B. M. Nichols, and B. W. Wessels, Phys. Rev. B **65,** 224110 (2002).

94   G. Williams and D. C. Watts, Trans. Faraday Soc. **66,** 80 (1970).

95   R. V. Chamberlin, Phase Transitions **65,** 169 (1998).

96   W. Kauzmann, Reviews of Modern Physics **14,** 12 (1942).

97   V. Shur, E. Rumyantsev, and S. Makarov, J. Appl. Phys. **84,** 445 (1998).

98   V. Y. Shur, E. L. Rumyantsev, E. V. Nikolaeva, E. I. Shishkin, I. S. Baturin, M. Ozgul, and C. A. Randall, Integr. Ferroelectr. **33,** 117 (2001).

99   A. Kholkin, I. Bdikin, D. Kiselev, V. Shvartsman, and S. H. Kim, J. Electroceram. **19,** 83 (2007).

100   D. C. Lupascu, S. Fedosov, C. Verdier, J. Rodel, and H. von Seggern, J. Appl. Phys. **95,** 1386 (2004).

101   J. Curie, Ann. Chim. Phys. **7,** 244 (1889).

102   E. von Schweidler, Pogg. Ann. Phys. **24,** 711 (1907).

103   V. Koval, M. J. Reece, and A. J. Bushby, Ferroelectrics **318,** 55 (2005).

104   J. Kakalios, R. A. Street, and W. B. Jackson, Phys. Rev. Lett. **59,** 1037 (1987).

105   R. G. Palmer, D. L. Stein, E. Abrahams, and P. W. Anderson, Phys. Rev. Lett. **53,** 958 (1984).

106   J. M. Benedetto, R. A. Moore, and F. B. McLean, Integr. Ferroelectr. **1,** 195 (1992).

107   B. S. Kang, J. G. Yoon, T. K. Song, S. Seo, Y. W. So, and T. W. Noh, Jpn. J. Appl. Phys. 1, Regul. Pap. Short Notes Rev. Pap. **41,** 6836 (2002).

108   I. G. Jenkins, T. K. Song, S. Madhukar, A. S. Prakash, S. Aggarwal, and R. Ramesh, Appl. Phys. Lett. **72,** 3300 (1998).

109   C. Dehoff, B. J. Rodriguez, A. I. Kingon, R. J. Nemanich, A. Gruverman, and J. S. Cross, Rev. Sci. Instrum. **76,** 023708 (2005).

110   V. Nagarajan, S. Aggarwal, A. Gruverman, R. Ramesh, and R. Waser, Appl. Phys. Lett. **86,** 3 (2005).

111   T. K. Song, J. G. Yoon, and S. I. Kwun, in *Microscopic polarization retention properties of ferroelectric Pb(Zr,Ti)O-3 thin films*, Iguassu Falls, Brazil, 2005 (Taylor & Francis Ltd), p. 61.

112   F. R. Elder, A. M. Gurewitsch, R. V. Langmuir, and H. C. Pollock, Phys. Rev. **71,** 829 (1947).

113   H. O. Moser, M. Ballauff, V. Bechtold, H. Bertagnolli, J. Bialy, P. vonBlanckenhagen, C. Bocchetta, W. Bothe, C. Coluzza, A. N. Danilewsky, K. D. Eichhorn, B. Eigenmann, D. Einfeld, L. Friedrich, M. Haller, N. Holtkamp, V. Honecker, K. Hummer, E. Huttel, J. Jacob, V. Kashikin, J. Kircher, H. KleweNebenius, A. Knochel, A. Krussel, G. Kumpe, K. D. Moller, J. Mohr, M. Nagaenko, F. J. Pantenburg, M. Plesko, J. Schaper, K. Schlosser, G. Schulz, S. Schuppler, H. Schweickert, I. Seidel, Y. Severgin, I. Shukeilo, L. Steinbock, R. Steininger, M. Svandrlik, G. Williams, K. Wilson, and J. Zegenhagen, in *Proceedings Of The 1995 Particle Accelerator Conference, Vols 1-5* (1996), p. 272.

114   A. Stierle, A. Steinhauser, A. Ruhm, F. U. Renner, R. Weigel, N. Kasper, and H. Dosch, Rev. Sci. Instrum. **75,** 5302 (2004).

115   A. C. Dürr, N. Koch, M. Kelsch, A. Rühm, J. Ghijsen, R. L. Johnson, J. J. Pireaux, J. Schwartz, F. Schreiber, H. Dosch, and A. Kahn, Phys. Rev. B **68,** 115428 (2003).

116   S. Lequien, L. Goirand, and F. Lesimple, in *Design of the Anomalous Scattering beamline at the European Synchrotron Radiation Facility*, Stony Brook, Ny, 1994 (Amer Inst Physics), p. 1725.

117   B. Buras and G. Materlik, Nucl. Instrum. Methods Phys. Res., Sect. A **246,** 21 (1986).

118   http://www.esrf.eu/UsersAndScience/Experiments/SurfaceScience/ID01/equipment.html/ optics.html

119   W. L. Bragg, Proc. R. Soc. London, A **89,** 248 (1913).

120   B. C. Larson and J. Z. Tischler, in *Time resolved techniques: An overview*, 1990 (SPIE), p. 90.

121   G. P. Williams, in *Infrared Synchrotron Radiation Instrumentation And Applications*, Chester, England, 1991 (Amer Inst Physics), p. 1535.

122   J. Bohm, P. Gruber, R. Spolenak, A. Stierle, A. Wanner, and E. Arzt, Rev. Sci. Instrum. **75,** 1110 (2004).

123   I. C. Noyan and J. B. Cohen, *Residual stress measurements by diffraction and interpretation* (Springer, New York, 1987).

124   C. J. Smithells and E. A. Brades, *Metals reference book*, 5 ed. (Butterworths, London, 1976).

125   D. J. Dingley and V. Randle, J. Mater. Sci. **27,** 4545 (1992).

126   F. J. Humphreys, J. Mater. Sci. **36,** 3833 (2001).

127   K. Z. Baba-Kishi, J. Mater. Sci. **37,** 1715 (2002).

128   R. Ruer, Z. Anorg. Chem. **51,** 315 (1906).

129   J. Slakhorst, Acta Metall. **23,** 301 (1975).

130   G. Gottstein, *Physikalische Grundlagen der Materialkunde* (Springer, Heidelberg, 1998).

131   L. A. Schmitt, K. A. Schonau, R. Theissmann, H. Fuess, H. Kungl, and M. J. Hoffmann, J. Appl. Phys. **101,** 7 (2007).

132   J. Munoz-Saldana, M. J. Hoffmann, and G. A. Schneider, J. Mater. Res. **18,** 1777 (2003).

133   D. G. Choi and S. K. Choi, J. Mater. Sci. **32,** 421 (1997).

134   E. Arzt, Acta Mat. **46,** 5611 (1998).

135   S. Lu, C. Zuo, H. Zeng, W. Huang, and H. Ji, Mater. Lett. **60,** 255 (2006).

136   F. Felten, Personal Communication, 2008

137   A. Tawfik, J. Am. Ceram. Soc. **68,** C317 (1985).

138   A. S. Bhalla, D. N. Bose, E. W. White, and L. E. Cross, Phys. Stat. Solidi A **7,** 335 (1971).

139   G. R. Barsch, Acta Crystallogr. Sect. A **32,** 575 (1976).

172

140   L. Burianová, M. Sulc, and M. Prokopová, J. Eur. Ceram. Soc. **21,** 1387 (2001).
141   M. V. Slinkina, G. I. Dontsov, and V. M. Zhukovsky, J. Mater. Sci. **28,** 5189 (1993).
142   A. C. Caballero, E. Nieto, P. Duran, C. Moure, M. Kosec, Z. Samardzija, and G. Drazic, J. Mater. Sci. **32,** 3257 (1997).
143   P. G. Shewmon, *Diffusion in Solids*, 2 ed. (Minerals, Metals & Materials Society, Warrendale, PA, 1989).
144   F. J. Humphreys and M. Hatherly, *Recrystallization and related annealing phenomena* 2ed. (Elsevier, Amsterdam, Heidelberg, 2004).
145   A. P. Wilkinson, J. S. Speck, A. K. Cheetham, S. Natarajan, and J. M. Thomas, Chem. Mater. **6,** 750 (2002).
146   R. G. Sabat, B. K. Mukherjee, W. Ren, and G. M. Yang, J. Appl. Phys. **101** (2007).
147   A. N. Martin, Microtecnic**,** 50 (1979).
148   B. L. Cheng and M. J. Reece, Bull. Mater. Sci. **24,** 165 (2001).
149   E. Defay, C. Malhaire, C. Dubois, and D. Barbier, in *Stress and stress relaxation study of sputtered PZT thin films for microsystems applications*, Boston, Ma, 1999 (Materials Research Society), p. 237.
150   H. Huang, Z. Tianshu, J. T. Oh, and P. Hing, Mater. Chem. Phys. **75,** 186 (2002).
151   A. A. Bokov and Z. G. Ye, J. Appl. Phys. **91,** 6656 (2002).
152   E. F. Bertaut and F. Lissalde, Solid State Commun. **5,** 173 (1967).
153   B. H. Hoerman, B. M. Nichols, M. J. Nystrom, and B. W. Wessels, Appl. Phys. Lett. **75,** 2707 (1999).
154   B. S. Kang, J.-G. Yoon, T. W. Noh, T. K. Song, S. Seo, Y. K. Lee, and J. K. Lee, Appl. Phys. Lett. **82,** 248 (2003).
155   J. Kim, C. J. Kim, and I. Chung, in *Retention behavior of ferroelectric memory devices depending on the capacitor processes*, Aachen, Germany, 2000 (Gordon Breach Sci Publ Ltd), p. 133.
156   D. Berlincourt and H. H. A. Krueger, J. Appl. Phys. **30,** 1804 (1959).
157   P. M. Chaplya and G. P. Carman, J. Appl. Phys. **92,** 1504 (2002).
158   J. M. Calderon-Moreno, Mater. Sci. Eng., A **315,** 227 (2001).
159   A. V. Turik and E. N. Sidorenko, in *Changing dielectric properties of ferroelectric ceramics by mechanical stresses*, Montreux, Switzerland, 1998 (Ieee), p. 533.
160   I. Kerkamm, Elektromechanisches Verhalten von Blei-Zirkonat-Titanat Massivkeramiken und Vielschichtaktoren, PhD Thesis, Technische Universität Darmstadt, 2008.
161   M. S. Ha, S. J. Jeong, J. H. Koh, H. B. Choi, and J. S. Song, Mater. Chem. Phys. **98,** 9 (2006).
162   L. Fa-Xin, F. Dai-Ning, and S. Ai-Kah, Smart Mater. Struct.**,** 668 (2004).
163   S. Lucato, H. A. Bahr, V. B. Pham, D. C. Lupascu, H. Balke, J. Rodel, and U. Bahr, J. Mech. Phys. Solids **50,** 2333 (2002).
164   A. Seeger, Phil. Mag. **1,** 651 (1956).
165   A. S. Nowick and W. R. Heller, Adv. Phys. **14,** 101 (1965).
166   A. Furuta and K. Uchino, J. Am. Ceram. Soc. **76,** 1615 (1993).
167   T. H. Hao, X. Gong, and Z. Suo, J. Mech. Phys. Solids **44,** 23 (1996).
168   E. Klotins, K. Kundzins, B. Andersen, and A. James, Ferroelectrics **199,** 261 (1997).
169   J. M. Benedetto, R. A. Moore, and F. B. McLean, J. Appl. Phys. **75,** 460 (1994).
170   K. Dimmler, M. Parris, D. Butler, S. Eaton, B. Pouligny, J. F. Scott, and Y. Ishibashi, J. Appl. Phys. **61,** 5467 (1987).
171   Y. Zhang and D. C. Lupascu, J. Appl. Phys. **100,** 54109 (2006).
172   W. Barletta and C. Rizzuto, Riv. Nuovo Cimento **29,** 1 (2006).
173   H. P. Freund and G. R. Neil, Proc. IEEE **87,** 782 (1999).
174   B. Sonntag, in *VUV and X-ray free-electron lasers*, Berlin, Germany, 2000 (Elsevier Science Bv), p. 8.
175   C. V. Schmising, M. Bargheer, M. Kiel, N. Zhavoronkov, M. Woerner, T. Elsaesser, I. Vrejoiu, D. Hesse, and M. Alexe, Phys. Rev. B **73** (2006).

176   C. Blome, T. Tschentscher, J. Davaasambuu, P. Durand, and S. Techert, in *Synchrotron Radiation Instrumentation, Pts 1 And 2*; *Vol. 879* (2007), p. 1254.

177   P. Wochner, C. Gutt, T. Autenrieth, T. Demmer, V. Bugaev, A. D. Ortiz, A. Duri, F. Zontone, G. Grubel, and H. Dosch, Proc. Natl. Acad. Sci. U. S. A. **106,** 11511 (2009).

178   E. F. Eikenberry, C. Bronnimann, G. Hulsen, H. Toyokawa, R. Horisberger, B. Schmitt, C. Schulze-Briese, and T. Tomizaki, in *PILATUS: a two-dimensional X-ray detector for macromolecular crystallography*, Brunnen, Switzerland, 2001 (Elsevier Science Bv), p. 260.